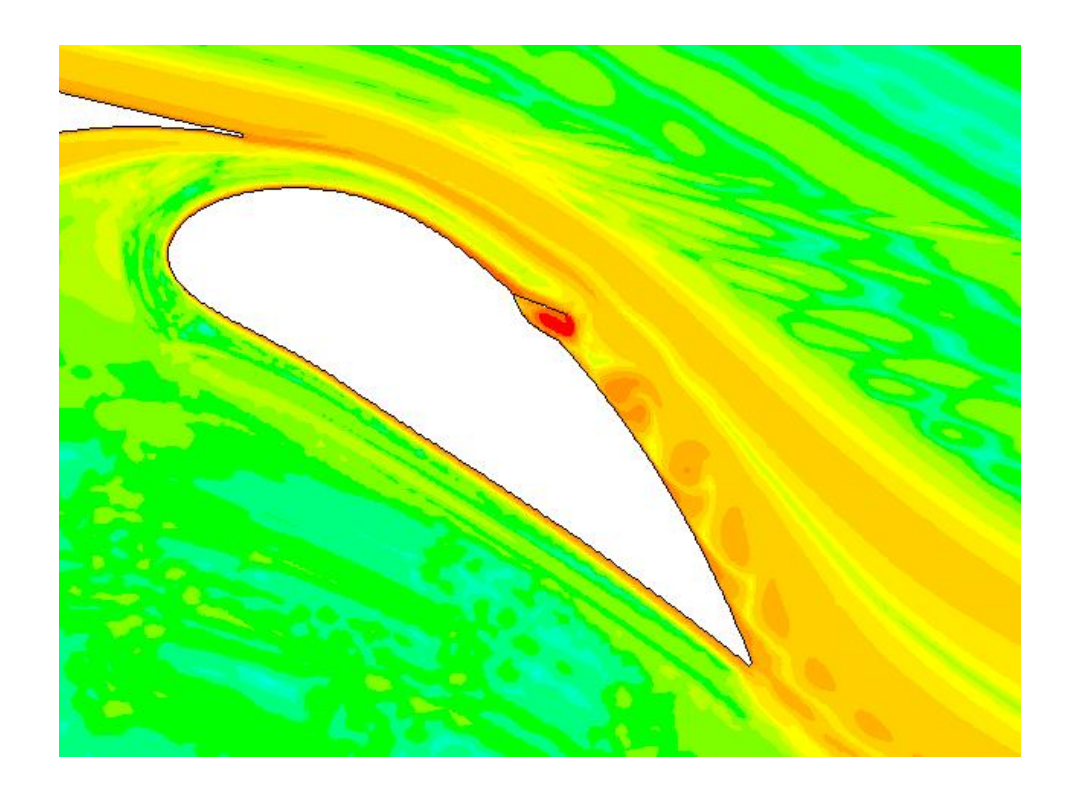
Flap Performance Improvement by Surface Excitation

A numerical research into active flow control



T.J.A. Dolle

June 17, 2009





Flap Performance Improvement by Surface Excitation

A numerical research into active flow control

Master of Science Thesis

For obtaining the degree of Master of Science in Aerospace Engineering at Delft University of Technology

T.J.A. Dolle

June 17, 2009



Delft University of Technology

Copyright © Aerospace Engineering, Delft University of Technology All rights reserved.

DELFT UNIVERSITY OF TECHNOLOGY DEPARTMENT OF AERODYNAMICS

The undersigned hereby certify that they have read and recommend to the Faculty of Aerospace Engineering for acceptance the thesis entitled "Flap Performance Improvement by Surface Excitation" by T.J.A. Dolle in fulfillment of the requirements for the degree of Master of Science.

	Dated: June 17, 2009
Supervisors:	
Supervisors.	Prof. dr. ir. drs. H. Bijl
	Dr. ir. L.L.M. Veldhuis
	Dr. ir. A.H. van Zuijlen
	Dr. T.J. Ahmed

Preface

This report is written as a Master Thesis at the Aerodynamics department of the Faculty of Aerospace Engineering of Delft University of Technology. It presents an overview of the graduation research that was performed between September 2008 and June 2009 at the High-Speed Aerodynamics Laboratory.

This report describes the numerical research about the application of flow control on an airfoil-flap configuration. The reader is only expected to have some basic knowledge about aerodynamics and computational fluid dynamics (CFD). Additional aerodynamic information is presented in chapter 2, while chapter 3 provides background information about the numerical setup. The chapters 4, 5 and 6 of the report present the results of numerical simulations in which the flow control is applied. This numerical study can be used as underlying support from which further experimental research can be set up.

It would not have been possible to realize this graduation research without the help of some specific people. First of all, I would like to thank my supervisor Dr. L.L.M. Veldhuis for his enthusiastic support during my graduation research. His view on flow physics and his interest in flow separation control have stimulated me enormously. And in the same way I would thank Dr. A.H. van Zuijlen for his supervision and for sharing his insights into numerical simulations. I would also like to thank E. de Keizer and S. Bernardy for their ICT support and I would thank all other involved staff members at the laboratory that helped me with practical advises. Finally, a special word of thanks goes to my friend and my parents for the confidence and the support they gave me during this graduation work.

Delft, June 2009

Tamara Dolle

<u>vi</u> Preface

Summary

The maximum lift coefficient that can be obtained with a certain airfoil is limited by the onset of flow separation. At a certain angle of attack the adverse pressure gradient becomes so strong that the flow can no longer follow the surface of the airfoil and separates, resulting in a decrease in lift and an increase in drag. This maximum lift coefficient can be increased by using high-lift devices like trailing edge flaps. However, flow separation still remains the limiting factor.

Flow separation control is a solution to this problem. By adding momentum to the boundary layer flow separation is postponed and higher lift coefficients can be reached. In this research active flow separation control by means of a vibrating surface element, a so-called fliperon, is investigated. Both the effectiveness and the efficiency of this flow control method are investigated for the NACA-0015 airfoil at 20° angle of attack and for the NLR7301 airfoil-flap configuration with flow separation from the 35° deflected flap. This research is performed completely numerically with the flow solver Fluent 6. For this research the RANS equations are closed with the $k-\epsilon$ turbulence model. Because the fliperon is oscillating during the simulation, the dynamic mesh model is used to rotate the fliperon and to keep the grid quality at a sufficient level.

The fliperon was located at a distance of about 20% (flap) chord length ahead of the flow separation point. The length is chosen such that the maximum amplitude of the fliperon tip equals the local boundary layer thickness. Further the shape of the fliperon is equal to the curvature of the airfoil at that location.

If the fliperon oscillates above a cavity, the shape of the cavity will also influence the generated vortices. The best results were obtained with a round cavity shape that increases the blowing effect in tangential direction and reduces the amount of additional vorticity that is generated. The performances of a fliperon oscillating above a cavity with a sharp trailing edge and a springboard type fliperon were less promising.

The most important parameter of the fliperon motion is the frequency. The frequency influences the size and the strength of the generated vortices. It is important that the generated vortices are sufficiently strong, because they have to travel towards the trailing edge and interact with the vortices that existed there due to the flow separation. Only then the total circulation is improved and the lift coefficient increased. In case of the NACA-0015 a dimensionless frequency F^+ of 1.2 turned out to be very effective, while

viii Summary

the most effective frequency on the NLR7301 airfoil-flap configuration was 6.0.

The fliperon motion should be defined such that the maximum amplitude of the fliperon tip is equal to the boundary layer thickness. Larger amplitudes did not lead to an additional improvement of the lift coefficient, while too small amplitudes did not improve the lift coefficient at all.

On the NACA-0015 airfoil the maximum increase in lift coefficient obtained by the application of a fliperon was 20% with respect to the uncontrolled situation. The corresponding momentum coefficient was 0.016, which makes the fliperon both an effective and an efficient method of flow control in this case.

On the NLR7301 airfoil flap configuration the maximum increase in lift coefficient was 21.2%, with a corresponding momentum coefficient of 0.144. Although the fliperon is still effective in this case, the momentum is now used less efficiently compared to other types of active flow control. Here the advantage of the fliperon is that it is less complex than several other flow control methods.

There are many ways in which the current research can be continued. In future numerical research it would be interesting to perform a large eddy simulation to investigate the influence of the cavity shape on the produced vortices in more detail. Further it is recommended to investigate the effect of different fliperon motions.

Since the current research has shown the effectiveness of the fliperon as flow control device, the risk of a wind tunnel experiment is reduced. In such an experiment the simulations can be validated, and the optimal frequency and amplitude ratio can be determined more accurately. Also the influence of 3D effects can be investigated. Furthermore the efficiency of the fliperon can be determined more accurately by measuring the required power.

Table of Contents

Pı	eface	9		V
Sι	ımma	ary		vii
Li	st of	Figures	S	xiii
Li	st of	Tables		xvii
N	omen	clature	:	xix
1	1.1 1.2 1.3	Outlin	low separation control?	. 2
2	Flov	v separ	ration control	7
	2.1	Flow s	separation	. 7
	2.2	Flow c	control techniques	. 10
		2.2.1 2.2.2 2.2.3	Passive flow control	. 12
	2.3	Govern	ning parameters	
		2.3.1	Dimensionless frequency	. 16
		2.3.2 2.3.3	Momentum coefficient	
	2.4	Resear	rch on flow control and fliperons	. 18

Setu	up of th	ne numerical simulations	23
3.1	Grid ge	eneration	23
	3.1.1	General grid shape	23
	3.1.2	Grid elements	25
3.2	Setup	of steady simulations	27
	3.2.1	Boundary conditions	27
	3.2.2	Turbulence modeling	28
	3.2.3	Solver settings	30
3.3	Unstea	dy simulations with dynamic meshes	31
	3.3.1	Dynamic mesh model	31
	3.3.2	Application to fliperon motion	33
Flow	v contr	ol on a ramp	37
		•	37
			38
			39
			39
	4.3.2	Flow field analysis	42
Elou		al an the NACA 0015 sinfail	47
			47
5.1	5.1.1		48
	5.1.2		48
5.2	Applica		52
	5.2.1	Implementation of the fliperon	52
	5.2.2	·	53
	5.2.3		54
5.3	Conclu	•	62
Flow	v contr	ol on the NLR7301 airfoil-flap configuration	63
6.1		·	63
6.2			69
	6.2.1	Current situation	69
	6.2.2	New flap design	69
	6.2.3	Results of steady simulation	72
6.3	Flow se	eparation control	74
	6.3.1	Springboard type fliperon	75
	6.3.2		79
	6.3.3	3 3	
	0.5.5	Improved cavity type fliperon	83
	6.3.4	Improved cavity type fliperon	83 88
	3.1 3.2 3.3 Flow 4.1 4.2 4.3 Flow 5.1 5.2 5.3 Flow 6.1 6.2	3.1 Grid get 3.1.1 3.1.2 3.2.2 Setup 3.2.1 3.2.2 3.2.3 3.3 Unstead 3.3.1 3.3.2 Flow control 4.1 Setup 4.2 Flow flow control 4.3.1 4.3.2 Flow control 5.1 Post-st 5.1.1 5.1.2 5.2 Application 5.2.1 5.2.2 5.2.3 5.3 Conclustification for control 6.1 Turbul 6.2 Adaptitication 6.2.1 6.2.2 6.2.3 6.3 Flow states of 6.3.1 6.3.2 flow states of 6.3.1 6.3.2 flow states of 6.3.1 6.3.2 flow states of 6.3.1 flow states of 6.3.1 flow states of 6.3.1 flow states of 6.3.2 flow states of 6.3.2 flow states of 6.3.2 flow states of 6.3.2 flow states of 6.3.1 flow states of 6.3.2 flow states o	3.1.1 General grid shape 3.1.2 Grid elements 3.2 Setup of steady simulations 3.2.1 Boundary conditions 3.2.2 Turbulence modeling 3.2.3 Solver settings 3.3 Unsteady simulations with dynamic meshes 3.3.1 Dynamic mesh model 3.3.2 Application to fliperon motion Flow control on a ramp 4.1 Setup of the test case 4.2 Flow field without flow control 4.3 Controlled ramp flow 4.3.1 Influence of frequency and amplitude 4.3.2 Flow field analysis Flow control on the NACA-0015 airfoil 5.1 Post-stall flow field 5.1.1 Reference work 5.1.2 Steady simulations 5.2 Application and results of flow control 5.2.1 Implementation of the fliperon 5.2.2 Fliperon frequency and amplitude 5.2.3 Unsteady simulations 5.3 Conclusion of the test case Flow control on the NLR7301 airfoil-flap configuration 6.1 Turbulence model validation 6.2 Adaption of the configuration 6.2.1 Current situation 6.2.3 Results of steady simulation 6.3 Flow separation control 6.3.1 Springboard type fliperon 6.3.2 Cavity type fliperon

<u>Ta</u>	able o	of Contents	xi	
7	Con	clusions and recommendations	95	
	7.1	Conclusions	95	
	7.2	Recommendations for future research	97	
Bi	bliog	raphy	101	
Α	Dyn	amic mesh model	103	
	A.1	Example of a user-defined function	103	
	A.2	Dynamic mesh parameters	103	
	A.3	Computational effort	105	
В	MSI	ES analysis	107	
	B.1	Input files	107	
	B.2	Results	108	
C	NLF	R7301 airfoil-flap coordinates	111	

Table of Contents

xii

List of Figures

1.1	2D view of flow that is separated from the upper side of an airfoil [25]	2
1.2	An aircraft just before landing. The flaps are deflected to increase the maximum lift coefficient.	3
2.1	The increasing pressure over the surface causes flow separation at point s_2 . Figure adapted from [2]	8
2.2	With increasing angle of attack, the separation point moves more and more towards the leading edge of the airfoil [17]	10
2.3	Placing a pair of vortex generators at small and opposite angles with respect to the flow direction will result in two counter rotating vortices that interact with the boundary layer [13]	11
2.4	The zigzag-tape is a commonly used turbulator and can have many different shapes	12
2.5	The self-activated movable flap is closed at low angles of attack and moves up automatically at higher angles [20]	13
2.6	Schematic drawing of a synthetic jet actuator	14
2.7	Schematic side view of two different types of fliperons [10]	15
2.8	Schematic drawing of vortex generation by means of a fliperon	16
2.9	Schematic drawing of the simplified airfoil-flap configuration used in [10] and [18].	19
2.10	Schematic drawing of the airfoil-flap model with fliperons on two different locations as used in [5]	20
2.11	Drawing of the test setup used by Van der Jagt [11]	21
3.1	The complete grid with the conical shaped front side in green and the straight backside in blue. The airfoil surface is coloured magenta.	24
3.2	Quadrilateral cells on and close to the flap surface, while triangular cells cover the nearfield and the farfield	25
3.3	$y^+\text{-values}$ for the upper and lower side of the main element and the flap. Note that flow separation occurs on the trailing edge of the flap. The simulation was based on the realizable $k-\epsilon$ turbulence model with standard wall functions	26
3.4	An example of spring-based smoothing for a cylindrical cell zone where one end of the cylinder is moving [3]	32

3.5	A block of triangular cells is located around the fliperon in order to enable the use of remeshing methods for updating the grid.	34
3.6	Spring-based smoothing and remeshing update the deformed grid such that each time step the flow calculations can be performed on a grid of sufficient quality.	35
4.1	Schematic representation of the test case geometry with the fliperon (red) in front of the backward ramp (dimensions in meters).	38
4.2	Velocity vectors (uniform length, skip factor 4) for ramp flow without flow control. The vectors indicate the direction of the flow velocity, while their colour indicates the magnitude of the velocity (in m/s)	39
4.3	Instantaneous pressure distributions over the ramp for fliperon motions with different frequencies, but with a constant amplitude ratio of 3.7	41
4.4	Pressure distributions over the ramp at $t=3.75\ ms$ for fliperon motions with different amplitude ratios, but a constant dimensionless frequency of 1.0	42
4.5	Instantaneous flow field of motion 2 after 3 fliperon oscillations ($F^+=0.7$ and $A_{max}/\delta=3.7$)	44
5.1	The NACA-0015 grid	49
5.2	Contour plot of velocity (magnitude) in m/s , representing the flow field around the NACA-0015 airfoil at $\alpha=20^\circ$, $M=0.12$, $Re=0.9\cdot 10^6$	50
5.3	Skin friction distribution over the airfoil at 20° , showing separation at $x/c\approx 0.65$ ($M=0.12$, $Re=0.9\cdot 10^6$)	50
5.4	Contour plot of velocity (magnitude) in m/s , now at $\alpha=20^\circ$, $M=0.12$, $Re=2.7\cdot 10^6$	51
5.5	Contour plot of vorticity (magnitude) in s^{-1} , showing a large vortex at the trailing edge caused by flow separation ($\alpha=20^\circ$, $M=0.12$, $Re=2.7\cdot 10^6$).	52
5.6	Aft part of the NACA-0015 airfoil. The rotating fliperon is drawn in green and is now in its lowest position ($\theta=0^{\circ}$)	53
5.7	Development of the airfoil lift coefficient in time at different fliperon frequencies.	55
5.8	Influence of maximum fliperon amplitude on the development of the lift coefficient.	56
5.9	Development of the velocity field during one fliperon oscillation in simulation A (velocities in m/s)	57
5.10	Instantaneous velocity field at the end of the fifth fliperon oscillation of simulation B. The larger vortices are less capable of interacting with the separated flow.	58
5.11	Vorticity contours (in s^{-1}) at the end of the last simulated fliperon oscillation. See also figure 5.5 for the vorticity field of the clean airfoil.	59
5.12	Development of the lift coefficient in simulation C	60
5.13	Development of the drag and aerodynamic moment coefficient in simulation C.	60
5.14	The increased fliperon frequency of simulation C results in vortices with a smaller diameter that seem to be perfectly capable of following the airfoil surface	61

List of Figures xv

5.15	Instantaneous velocity field at the end of the seventh fliperon oscillation in simulation D. The larger maximum amplitude results in slightly more circular vortices.	61
6.1	The NLR7301 airfoil with the flap deflected over 20°	64
6.2	Comparison of experimentally and numerically obtained pressure distributions at $\alpha=6.0^{\circ}.$	66
6.3	Comparison of experimentally and numerically obtained pressure distributions at $\alpha=10.1^{\circ}.$	68
6.4	Contour plot of the x-velocity, indicating flow separation (negative x-velocities) immediately at the flap leading edge.	70
6.5	Geometry of the main airfoil (NLR7301) and the new flap	72
6.6	Contour plot of the x-velocity. On the adapted configuration flow separation does not occur on the first half of the flap surface	73
6.7	Skin friction coefficient at the flap upper surface (green) and lower surface (blue).	73
6.8	Overview of the different fliperon geometries applied on the flap of the NLR7301 configuration. The solid lines show the maximum fliperon deflection, the dashed lines indicate the minimum deflection angle (starting position of each oscillation).	74
6.9	Development of the oscillation-averaged lift coefficient in time caused by the application of the springboard type fliperon.	76
6.10	Development of the average aerodynamic coefficients in time when a springboard type fliperon is applied.	77
6.11	Developed of the vorticity field with the springboard type fliperon. The contours indicate the vorticity magnitude in s^{-1}	77
6.12	Schematic drawing of the development of (1) primary and (2) secondary vortices.	78
6.13	Development of the vorticity field during one oscillation of the springboard type fliperon in motion II: $F^+=6.0$, $A_{max}/\delta=1.2$ (vorticity in s^{-1})	80
6.14	Development of the average lift coefficient in time when the fliperon oscillates above the original cavity	81
	Vorticity fields resulting from different motions of the original cavity type fliperon. Contours indicate vorticity magnitude in s^{-1}	82
6.16	Development of the vorticity field during one oscillation of the original cavity type fliperon in motion II: $F^+=6.0$, $A_{max}/\delta=1.0$ (vorticity in s^{-1})	84
6.17	Development of the average lift coefficient in time when the fliperon oscillates above the new cavity.	86
6.18	Vorticity fields resulting from different motions applied to the fliperon above the new cavity. Contours indicate vorticity magnitude in s^{-1}	88
6.19	Development of the vorticity field during one oscillation of the fliperon above the new cavity (vorticity in s^{-1}). Motion II: $F^+=6.0$, $A_{max}/\delta=1.0$	89
B.1	Pressure distribution and streamlines for a flap deflection of 35°	109
B.2	Separation is predicted much earlier in the fully turbulent simulation (red asterisk) than in the simulation with free transition (green asterisk)	109

xvi List of Figures

List of Tables

2.1	increase	21
4.1	Overview of performed simulations and their results	40
5.1	Overview of the parameters describing the different fliperon motions	54
6.1	Aerodynamic force coefficients at $\alpha=0.0^\circ$ for numerical simulation with different turbulence models compared to experimental values	65
6.2	Experimental and numerical aerodynamic force coefficients at $\alpha=6.0^{\circ}.$	66
6.3	Experimental and numerical aerodynamic force coefficients at $\alpha=10.1^{\circ}.$	68
6.4	Overview of performed simulations in which flow control is applied on the NLR7301 airfoil-flap configuration.	75
6.5	Overview of the resulting lift coefficient increases from different fliperon geometries.	90
A.1	Overview of the parameters used in the dynamic mesh model	104
A.2	Grid zones and their corresponding motion type for the NLR7301 airfoil-flap configuration.	104
A.3	Computation times for the different configurations	105

xviii List of Tables

Nomenclature

 A_{max} Maximum amplitude of fliperon tip

 $egin{array}{ll} c & & {
m Airfoil\ chord} \ C_D & & {
m Drag\ coefficient} \ C_L & & {
m Lift\ coefficient} \ \end{array}$

 C_M Aerodynamic moment coefficient w.r.t. quarter chord point

 c_p Pressure coefficient $C_{L_{\alpha}}$ Lift curve slope

 $\langle c_{\mu} \rangle$ Oscillatory momentum coefficient

 C_{μ} Momentum coefficient f Excitation frequency F^{+} Dimensionless frequency

G Slot width

k Turbulent kinetic energy

L Body length

m Maximum airfoil camber

M Mach number

n Coordinate normal to the surface

p Pressure

p Position of maximum camber on airfoil

Re Reynolds number based on main airfoil chord

Strouhal number

t Maximum airfoil thickness

t Time

u' Oscillatory velocity component

 u_{τ} Friction velocity

U Velocity

 U_{∞} Free stream velocity

V Flow velocity

x Chordwise coordinate

 x_{TE} Distance from fliperon hinge to trailing edge

Nomenclature $\mathbf{x}\mathbf{x}$

$y \\ y^+ \\ z$	Normal coordinate Indicator of boundary layer grid cell size Spanwise coordinate
$egin{array}{l} lpha \ lpha_s \ \gamma \ \delta \ \delta_{flap} \ \Delta \ \epsilon \ \eta \ heta \ \mu \ ho \ au_w \ \phi \ \omega \ \omega \end{array}$	Angle of attack Stall angle Ratio of specific heats Boundary layer thickness Flap deflection angle Change in variable; final-initial Dissipation rate of turbulent kinetic energy Coordinate normal to the surface Fliperon deflection angle Viscosity Density Wall shear stress Slope of mean camber line Angular velocity Specific dissipation rate of turbulent kinetic energy
2D $3D$ CFD DNS CG FMG LE LES $NACA$ NLR PIV $RANS$ $S - A$ SST TE	2-dimensional 3-dimensional Computational Fluid Dynamics Direct Numerical Simulation Center of Gravity Full Multigrid Leading Edge Large Eddy Simulation National Advisory Committee for Aeronautics National Aerospace Laboratory Particle Image Velocimetry Reynolds Averaged Navier-Stokes Spalart-Allmaras Shear-Stress Transport Trailing Edge

T.J.A. Dolle MSc. Thesis

Chapter 1

Introduction

Flow separation is a physical phenomenon that can occur in many engineering applications where a fluid flows over a solid surface. Examples are the flow of oil through a pipe and the airflow over a golf ball, a windmill blade and an aircraft wing. These situations are quite different, but have one thing in common: the flow separation is unwanted and postponement of the separation will lead to an improved aerodynamic performance. In this thesis the focus will be on the aircraft wing, but probably the results can also be valuable outside this application.

1.1 Why flow separation control?

The wings of an aircraft have one main task: generating a lift force that can keep the aircraft in the air. So in cruise flight the lift force should be equal to the weight of the aircraft. The corresponding lift coefficient is much lower than the maximum lift coefficient that can be reached by the wings. During maneuvers, take-off and landing a much higher lift coefficient is required, because the load factor increases (maneuvers) or the velocity of the aircraft is quite low (take-off, landing).

Increasing the lift coefficient can be done in many ways. The easiest way is to increase the angle of attack of the wing. However, each wing has its maximum lift coefficient that occurs at the angle of attack known as the stall angle. Increasing the angle of attack beyond the stall angle will result in an air flow that is no longer attached to the wing, as is shown in figure 1.1. This means a decrease in lift coefficient and an increase in drag coefficient, which are both highly unwanted effects.

In order to increase the maximum lift coefficient of a wing high-lift devices can be used (see figure 1.2). Normally these high-lift devices consist of a leading edge slat and a trailing edge flap that can consist of several elements as well. Due to the deflection of these high-lift devices the camber, and often also the area of the wing increase resulting in a much higher lift coefficient. The price that has to be paid for this is a decrease in

2 Introduction

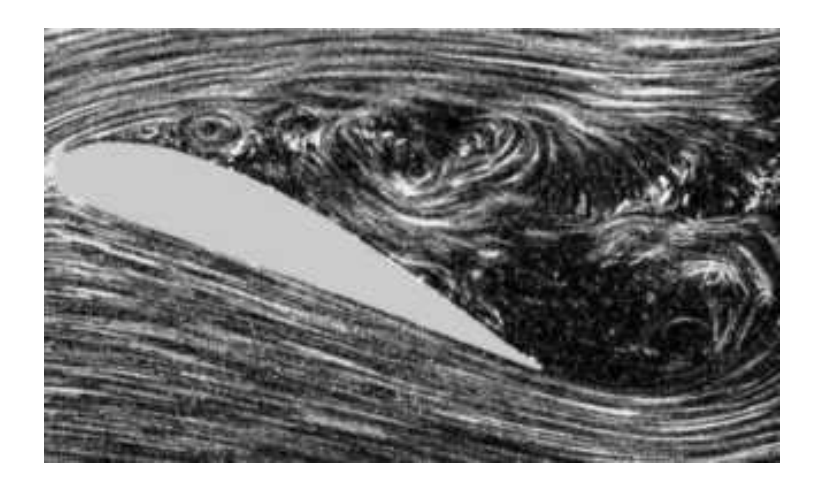


Figure 1.1: 2D view of flow that is separated from the upper side of an airfoil [25].

stall angle. Beyond the stall angle flow separation can now occur on both the main wing element and the high-lift devices.

So although high-lift devices are useful in increasing the lift coefficient at a given angle of attack, the maximum lift coefficient is still determined by the occurrence of flow separation. Therefore it is very useful to try to influence the flow over the wing and the high-lift devices such that flow separation is postponed. This is called flow separation control. Although this topic has been studied for over a hundred years, it still has the interest of scientists today. In the search for more efficient aircraft with more efficient wings, the concept of flow separation control has become one of the most important topics. Flow control can be applied in many different ways. In general two types of flow control are distinguished: active and passive flow control. Passive flow control methods do not require additional energy to influence the flow. Well-known examples are vortex generators and turbulators. Active flow control methods need additional energy to influence the flow. This energy is for example needed to activate pumps (for blowing or boundary layer suction) or to bring surfaces into motion. These surface motions can be used to generate specific flow structures, as is the case with synthetic jets [16] and fliperons [10]. The term fliperon is used in literature ([18], [10]) for a small, rigid surface that is connected to the main surface by means of a hinge. The fliperon can rotate about the hinge and perform an oscillating motion, that will influence the flow over the main surface.

1.2 Outline of the thesis project

The main subject of this thesis work is flow separation control by means of an oscillating fliperon. More specifically, the goal of this thesis can be formulated as: to numerically investigate the performance improvements of an airfoil-flap configuration when active flow control by means of an oscillating fliperon is applied. This thesis should

make clear whether the fliperon is an effective and efficient flow separation control device. The effectiveness can be seen as a measure for the performance of the flow control device. An effective flow control device is able to increase the lift coefficient significantly. Efficiency is defined here as the ratio of the additional lift and the price that has to be paid for the additional lift. This price contains not only the additional costs, but also the weight and the complexity of the fliperon system are taken into account.

The background situation in which this thesis work should be placed is the landing phase of an aircraft as shown in figure 1.2. As was seen in the previous section, the landing is one of the flight phases in which the postponement of flow separation would be very useful. During the landing approach the flight speed is low and the flaps are maximal deflected. The maximum lift coefficient is the most important parameter in this phase; the drag coefficient is not so important. The application of flow control can lead to a larger maximum flap deflection at which separation occurs, resulting in a higher maximum lift coefficient and a lower stall speed. Another advantage of the higher maximum lift coefficient is the possibility to decrease the area of the high-lift devices and so saving weight and reducing drag in other flight phases.



Figure 1.2: An aircraft just before landing. The flaps are deflected to increase the maximum lift coefficient.

The research of this thesis work will be a completely numerical research, in which the flow solver program Fluent 6 will be used. Although this subject is also suited for experimental research, no experiments are performed within this thesis work. The risk of such an experiment is rather high, since the effectiveness of a fliperon on a flap is not fully proven. If the numerical research will lead to positive results, this research can serve as a foundation on which wind tunnel experiments can be based.

In the thesis statement was mentioned that the fliperon will be investigated on an airfoil-flap configuration, which means that the problem will be considered in 2D. The main reason is that the largest effects of the fliperon motion will occur in chordwise direction. Further the complexity and the calculation time are much smaller for a 2D numerical simulation than for a 3D simulation. However, it should be realized that several 3D effects

4 Introduction

like cross-flow and the influence of wing tip vortices can not be taken into account in this research.

1.3 Setup of the thesis and the report

In order to reach the goal of investigating the influence of a fliperon on the flow over an airfoil-flap configuration, several steps need to be taken. First of all, the aerodynamic theory behind flow separation and flow control is studied. This study, of which the results are presented in chapter 2, makes clear how flow separation can occur and what flow control should do to prevent this. Further the most important flow control parameters are introduced and reference researches about flow control are discussed.

The next step is to create a general setup for the numerical simulations. This means that grids have to be generated and that the flow solver settings have to be examined. Because the fliperon is moving, some special dynamic models will be used in the simulations. All these aspects and much more numerical topics are discussed in chapter 3.

With this solid background in both physics and numerics the first numerical simulations are performed. In order to gain experience with the dynamic models of the flow solver, a simple test case is considered. In this test the separated flow over a ramp is studied, and flow control by means of a fliperon is applied to improve the flow field. Although the physical phenomena are not the main topic of this test case, the influence of the fliperon motion parameters frequency and amplitude is considered as well. The setup of this case and the results are discussed in chapter 4.

With the experience of the first test case, a second test case is performed as described in chapter 5. In this test case the separated flow over the NACA-0015 airfoil is investigated and again flow control by means of a fliperon is applied. Since the NACA-0015 is a single-element airfoil, the flow field and the application of a fliperon will be less complicated than for a multi-element airfoil. The influence of the fliperon frequency and amplitude is studied in more detail here. Further a closer look is taken at the influence of the fliperon motion on the produced and the existing flow structures. The results of this test case are significant, because it becomes clear if the fliperon is able to reattach separated flow and to increase the lift coefficient.

Finally the application of flow control by means of a fliperon is simulated on the NLR7301 airfoil-flap configuration. The flap is deflected over 35°, which means that flow separation occurs on the trailing edge of the flap. Several types of fliperons will be applied to counteract the separation. Next to this influence of the geometry again the influence of the fliperon frequency is examined. A detailed analysis of the flow structures reveals how the flow field is changed by the fliperon. By comparing the results reached with the fliperon to other methods of flow control, some conclusions about the efficiency of flow control by means of a fliperon can be drawn. The complete analysis of flow control on the NLR7301 airfoil-flap configuration is presented in chapter 6.

The conclusions that follow from the test cases and the final application of a fliperon on an airfoil-flap configuration are presented in chapter 7. This chapter also presents recommendations for further research, which can be both numerical and experimental.

6 Introduction

Chapter 2

Flow separation control

Before flow control can be applied in a numerical simulation, some theoretical background knowledge is needed about the physical principles and phenomena that will take place. It is also important to realize that quite some experience is already gained by several experimental researches about this topic. This chapter will make an attempt to summarize the available information and experiences, such that the processes of flow separation and flow control will become clear. Finally, this understanding should be helpful when setting up the simulations. Of course it is not possible to present all information here, so references will be given in which more information can be found.

In order to find out what flow separation is exactly, a closer look at boundary layer flows is taken in section 2.1. When it has become clear how flow separation occurs, several flow control techniques can be applied to counteract the separation. These techniques will be discussed in section 2.2. It will turn out that the amount of flow separation control can be characterized by a couple of dimensionless parameters. In section 2.3 these parameters will be explained in detail. Finally, an overview of experimental research related to flow separation control by means of fliperons will be presented in section 2.4.

2.1 Flow separation

When a fluid flows over a solid surface, the viscosity of the fluid causes friction between the surface and the adjacent fluid. This friction results in a shear stress on the solid surface and a force that causes deceleration of the flow near the surface. Exactly at the surface the flow velocity is zero: this is called the no-slip condition.

The boundary layer is the region of the flow in which the flow velocity is lower than the free stream velocity. This region starts at the solid surface and has a finite hight, commonly known as the boundary layer thickness. At this hight the flow velocity has become (almost) equal to the free stream velocity. Within the boundary layer the velocity depends on the distance from the surface. This boundary layer velocity profile can have different shapes, as will be explained now.

Next to friction also the pressure field influences the flow over the solid surface. If the pressure over the surface is increasing (often indicated as an adverse pressure gradient), it becomes more difficult for the fluid elements to follow the surface and flow against the increasing pressure. This adverse pressure gradient causes a change in the boundary layer velocity profile, as can be seen in figure 2.1. At the beginning of the surface (at s_1), the fluid elements contain enough energy to follow the surface. The derivative of the fluid velocity with respect to the distance perpendicular to the surface, $\frac{\partial V}{\partial n}$, is positive. At a certain point s_2 the adverse pressure gradient and the friction have slowed down the fluid elements that much, that they do not contain enough energy to follow the surface any more. At this point, the velocity gradient $\frac{\partial V}{\partial n}$ is zero at the surface. Beyond this point (for example at location s_3), the fluid elements are pushed back by the strong pressure and reversed flow occurs. The fluid elements are separated from the surface now, and a wake of circulating flow will occur.

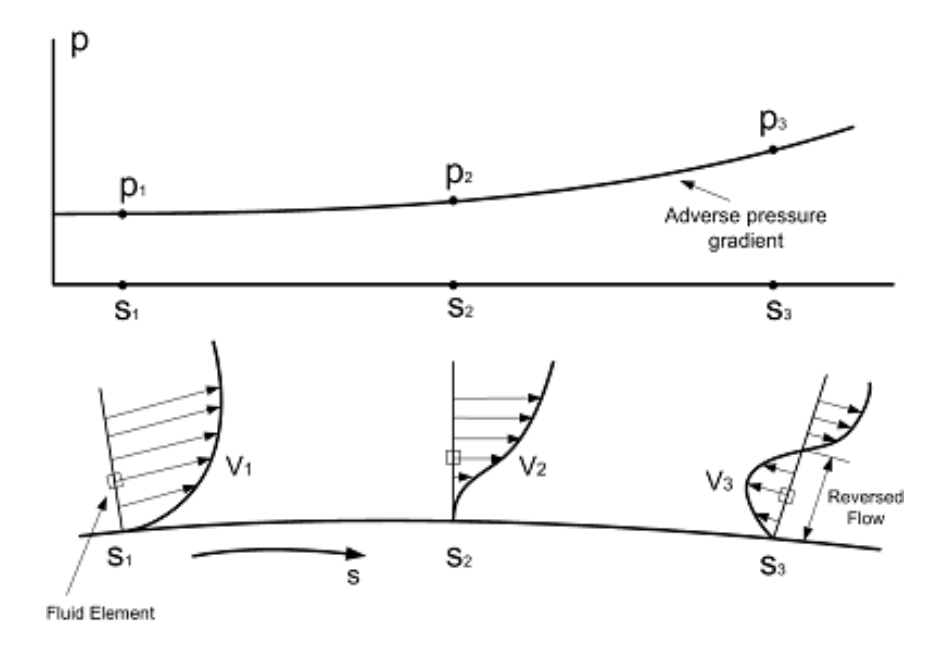


Figure 2.1: The increasing pressure over the surface causes flow separation at point s_2 . Figure adapted from [2].

The pressure distribution over an airfoil develops in the same way. On the upper surface an adverse pressure gradient occurs and so a flow separation point can be found. Beyond that point reversed flow occurs in the wake.

The adverse pressure gradient becomes stronger when the airfoil has a larger angle of attack. This process is illustrated in figure 2.2. At small angles of attack, the flow will have enough energy to follow the whole airfoil surface and no separation will occur. Increasing the angle of attack leads to a larger deflection of the flow and to an increase in the lift force that is generated. However, with increasing angle of attack also the separation point will move from the trailing edge towards the leading edge of the airfoil. At a certain angle of attack

the amount of separated flow becomes that large, that increasing the angle of attack results in a decrease in lift. This angle of attack is called the stall angle, and is thus also the angle at which the maximum lift coefficient is found.

Next to this trailing edge stall also leading edge stall can occur on thin airfoils with small nose radii. This type of stall is much more abrupt, since a large part of the flow separates at once. Because airfoils that suffer leading edge stall are not well suited for flow control, here the focus will be on airfoils that show trailing edge stall as described above.

On a multi-element airfoil, for example a main element with a deflected flap, more or less the same effects can occur on the flap. When the main element is at a small angle of attack and the flap is deflected over a small angle, all the flow will be attached. Increasing the flap deflection angle will result in a separation point that moves from the trailing edge of the flap towards the leading edge. When the main element also has a large angle of attack, flow separation may first occur at the trailing edge of the main element. In this case the wake of the main element will influence the flow around the flap, which will often result in flow separation from the flap as well.

Now consider an airfoil at an angle of attack that is larger than the stall angle: the airfoil is in the post-stall regime. This means that the airfoil is still generating some lift, but much less than the earlier reached maximum. Some flow is still attached to the upper surface near the leading edge of the airfoil, but also a reasonable amount of flow is separated. In figure 2.2, the post stall regime is found just between the situations at $\alpha = 16^{\circ}$ and $\alpha = 20^{\circ}$. And this is exactly the regime where flow control techniques can be applied.

The aim of flow control is to improve the flow around the airfoil or airfoil configuration and so increase the lift or reduce the drag. This can be done by attaching the flow that was originally separated in the post-stall regime. When this flow is reattached, the maximum lift coefficient will increase, just as the stall angle. Considering the airfoil as airplane wing element, many beneficial effects can be found. Examples are a lower stall speed and so an enlarged flight envelope, or the reduction of the size (and weight) of the high lift devices on the wing.

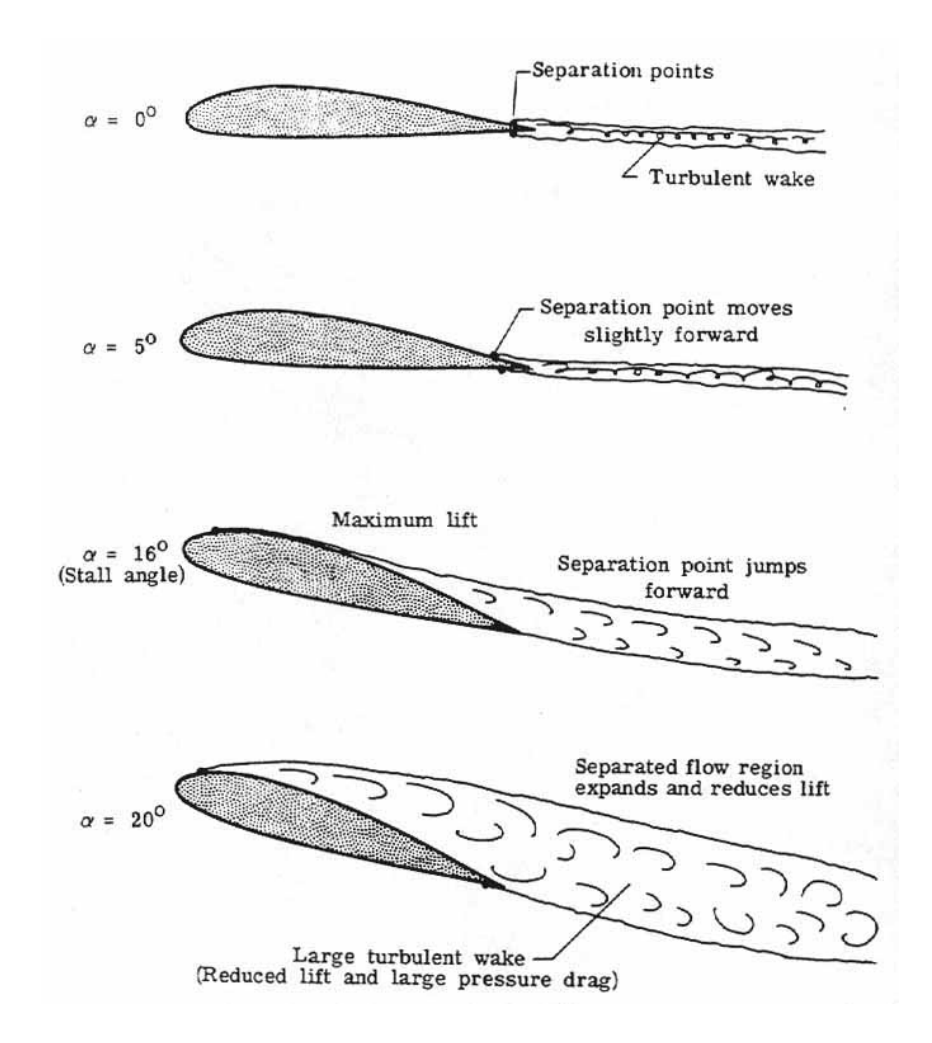


Figure 2.2: With increasing angle of attack, the separation point moves more and more towards the leading edge of the airfoil [17].

2.2 Flow control techniques

Already in the year 1904 the German aerodynamicist Ludwig Prandtl investigated the topics of flow separation and flow control. Since that time many different methods for flow separation control have been developed. These methods can be divided into two groups: passive flow control methods and active flow control methods. The difference is that passive flow control methods do not need additional energy to perform their job, where active methods make use of actuators for which power supply is needed. Consequently, passive flow control methods are in general less complex and easy to use, but may have some negative side effects in situations where they are not needed. Active methods are generally more effective and can be applied when needed, but the underlying systems are often complex and expensive. In the following sections, examples of both types of control methods will be discussed in more detail. Finally the control method that will be used in the current thesis work is presented.

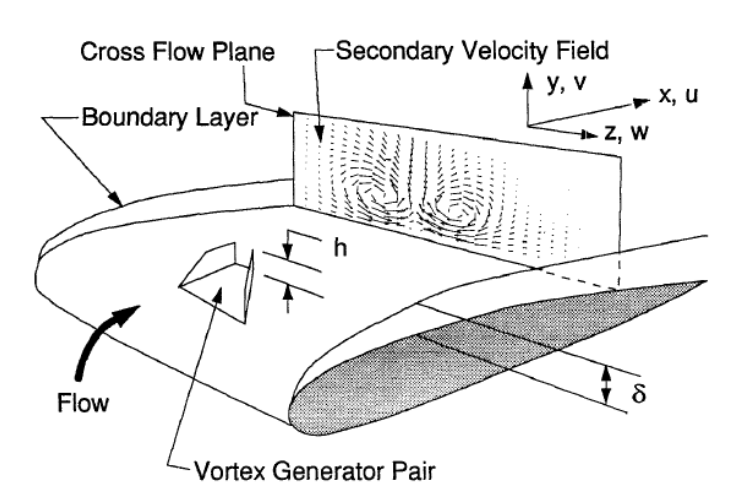


Figure 2.3: Placing a pair of vortex generators at small and opposite angles with respect to the flow direction will result in two counter rotating vortices that interact with the boundary layer [13].

2.2.1 Passive flow control

One of the most well-known methods for passive flow separation control is the use of vortex generators. Vortex generators can have many different shapes, but their height is usually in the order of the boundary layer thickness, so not more than a few centimeters on large wings. The vortex generators are mounted on the wing, in the direction of the flow or at a small angle with respect to the flow direction, as is shown in figure 2.3. When the flow passes the vortex generators, vortices occur from their edges. These vortices contain energy and interact with the boundary layer flow of the wing. In this way the boundary layer is energized, which makes it more resistant to adverse pressure gradients. This postpones separation, and so improves the aerodynamic characteristics of the wing. In the same way vortex generators can be applied on the flap of an airfoil-flap configuration, as was demonstrated in [13].

Next to the classic vortex generators, there is another technique that uses the vortices of a second object to interact with the boundary layer of the main flow. An example is the use of cylinders, as was demonstrated in [23]. The cylinders are not mounted on the surface, as would be the case with traditional vortex generators, but are located at a small distance from the surface. When the flow passes the cylinder, it sheds a Von Kármán vortex street that interacts with the surface boundary layer. The shed vortices mix air from inside and outside the boundary layer, resulting in a transfer of momentum. And so the separation of the boundary layer is prevented or postponed. Although this method is more difficult to apply on a real aircraft wing, the theoretical results are promising.

Another example of passive flow control is the use of turbulators. Turbulators are

very small devices, that locally increase the surface roughness. In figure 2.4 some examples of turbulators are shown. If an airfoil suffers from laminar separation near the leading edge, it can be effective to create artificial transition such that a turbulent boundary layer is formed that stays attached to the airfoil [6]. The artificial transition can be realized by applying zigzag-tape, tape with bulges or another form of roughness. Although this sounds very easy, the design of a turbulator is quite a complicated process. The influence of several parameters, for example the angles in the zigzag-tape, is difficult to calculate and often has to be optimized by trial and error.

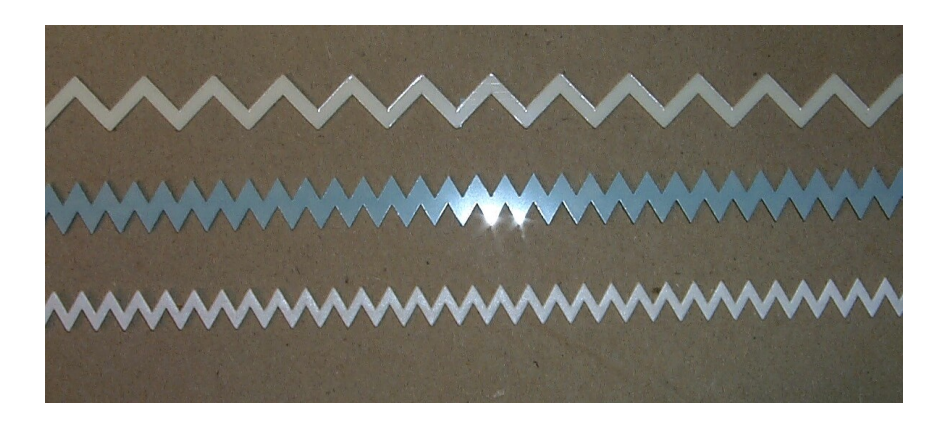


Figure 2.4: The zigzag-tape is a commonly used turbulator and can have many different shapes.

The last example of passive flow control that will be mentioned here is the use of deforming and moving surfaces. This technique can also be applied in many different ways, but the general principle is the same: the local aerodynamic forces influence the shape of the surface such that the flow field improves.

An example of moving surfaces is the self-activated movable flap as presented in [20] and shown in figure 2.5. At low angles of attack, the flap remains attached to the airfoil and does not have any influence. If flow separation and reversed flow occur near the trailing edge, the movable flap moves up. This results in a blockage of the reversed flow, such that it can not influence the leading edge suction peak. This causes a delay of the flow separation and an increase in lift coefficient. The design of the movable flap is based on the wings of birds, which also have several layers of feathers that move in different ways.

2.2.2 Active flow control

Opposed to passive flow control, for which no additional energy is needed, active flow control methods always require additional energy. A first example of a traditional active flow control technique is boundary layer suction (for more detailed information see [24]). The idea is rather simple: the lower part of the boundary layer, which is also the part that contains the smallest amount of energy, is removed and replaced by the layer just above it. This layer contains much more energy and that results in a much fuller boundary

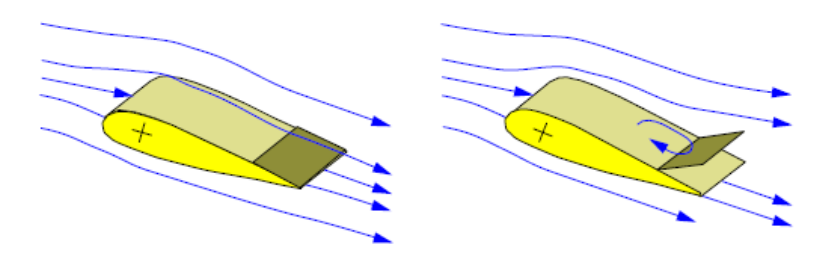


Figure 2.5: The self-activated movable flap is closed at low angles of attack and moves up automatically at higher angles [20].

layer velocity profile. In laminar flows, boundary layer suction can be used to stabilize the boundary layer and to postpone transition. In turbulent flows boundary layer suction is also very useful [24]. The thickness of the boundary layer is reduced and so separation is postponed. Considering an airfoil, this results in a higher stall angle and an increase in maximum lift coefficient up till about 20% [7].

Another active flow control method is periodic excitation. This means that air is alternatingly blown into or sucked away from the boundary layer. If the same amount of air is blown out as was sucked in, the control system is called a zero-net-mass-flux control. Periodic excitation is a more efficient way of flow control than steady blowing or suction, because the flow can now be excited at frequencies that correspond to the natural frequencies of instabilities in the separating flow. Furthermore periodic excitation generates a flow with a larger momentum and is able to control the mixing of that flow with the less energetic flow layers [10], [15]. In this way the momentum of the boundary layer is increased, which postpones separation and increases the lift coefficient of the airfoil.

An example of active flow control in which no mass is added to the fluid is the use of a synthetic jet [16]. A synthetic jet is in fact nothing more than a cavity inside the airfoil that is connected to the airfoil surface by means of a small orifice. One of the walls of the cavity is made of a flexible material, usually called a diaphragm. When the diaphragm is activated (for example by using a piezoelectric material), it starts vibrating. As a consequence of the pressure waves that occur from the upward and downward motion of the diaphragm, vortical ring flow structures are emitted from the small orifice into the boundary layer of the airfoil, see figure 2.6. These high energy vortices transfer momentum to the boundary layer, resulting in a separation point that moves towards the trailing edge of the airfoil.

The last example of active flow control that will be presented in this section are deforming surfaces. These surfaces differ from the surfaces discussed in the previous section about passive flow control in the sense that here an actuator controls the movement of the surface, instead of the aerodynamic forces that control the movement in case of passive flow control.

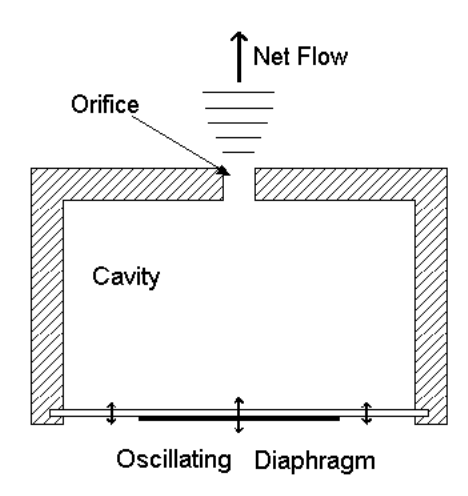


Figure 2.6: Schematic drawing of a synthetic jet actuator.

An example of flow control with deforming surfaces is the morphing wing concept [22]. This type of flow control is often used in the transonic regime, because small changes in the airfoil shape will have a large influence on the occurrence and the strength of shock waves. With actuators the wing camber can be adapted, which will result in a significant drag reduction. On a slightly smaller scale morphing surfaces can also be build in a flap. In this way the camber of the flap can be adapted to the flight situation, which might be more efficient than controlling the flap deflection angle only. A disadvantage of this technique is that the actuation system is complex and therefore also quite expensive.

Deforming surfaces can also be used as flow control devices in another way. In [21] the active flexible wall concept is introduced. This system consists of a flexible dielectric membrane, that can be build on an airfoil as part of the skin. Actuators control the vibration of the flexible membrane. The vibrations of this wall surface cause pressure and velocity fluctuations that interact with the boundary layer in such a way that momentum can be transferred. However, at this moment the technique is limited to marginally separated flows.

2.2.3 Flow control by means of a fliperon

In this thesis work flow control will be performed by means of a fliperon. This technique is an active flow control technique and belongs to the category of the surface excitations [18], [10]. In this case there are no deforming surfaces; the actual flow control is performed by the oscillating fliperon that adds momentum to the boundary layer. The fliperon itself is nothing more than a small piece of solid material that is connected to the airfoil surface. When activated (usually electrically), the fliperon can perform small rotations around the connection hinge line. An oscillation is defined here as an upward rotation to the point of maximum deflection and a downward rotation back to the original position.

Two different types of fliperons can be distinguished: the springboard type fliperon and the cavity type fliperon. Both types are shown in figure 2.7. The springboard type fliperon is placed above the airfoil surface. At its most downward position, it is possible that the fliperon touches the surface (at that moment the fliperon deflection angle θ is exactly zero), but it is also possible that a small angle always remains between the fliperon and the surface. The cavity type fliperon should be placed above a cavity in the airfoil surface. A fliperon deflection angle of zero degrees means that the fliperon is at the position where the original airfoil surface was located. A positive deflection angle corresponds to an upward motion of the fliperon, while a negative deflection angle means a downward fliperon motion into the cavity. The shape of the cavity can be rectangular or triangular. The depth is usually quite small.

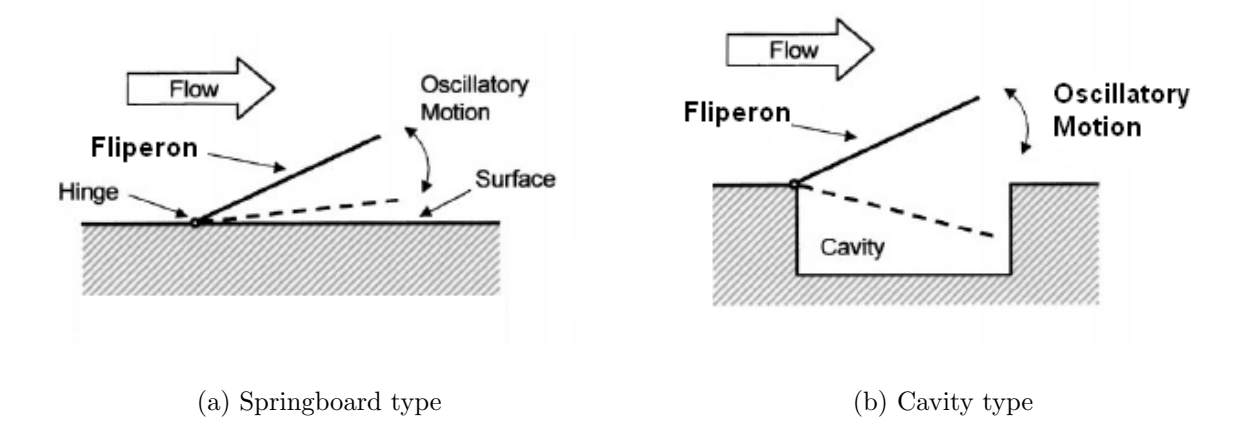
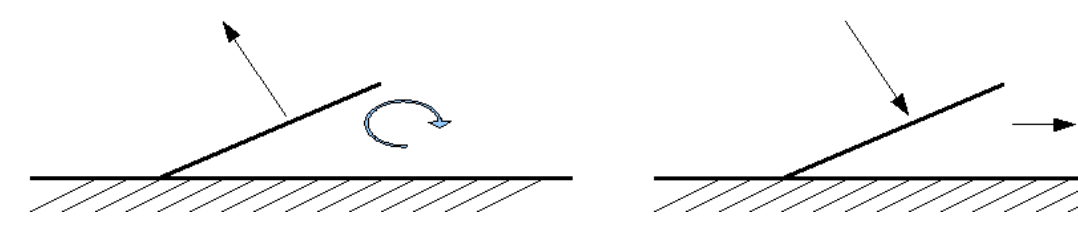


Figure 2.7: Schematic side view of two different types of fliperons [10].

The physical background of both types of fliperons is the same and has been investigated experimentally in [11] and [5]. In figure 2.8 the effect of an oscillating fliperon is drawn schematically. The fliperon oscillates such that vortices occur on the tip. These vortices are generated during the upward motion of the fliperon (figure 2.8(a)). During the downward motion they separate from the fliperon and travel downstream to interact with the boundary layer on the airfoil (figure 2.8(b). Because the vortices are high energy flow structures, they are able to transfer momentum into the boundary layer. Consequently, the boundary layer becomes more resistant to adverse pressure gradient and can stay attached to the surface for a longer distance. This means less separation and an increase in lift coefficient. In the current research the application of a fliperon on both a single element airfoil and an airfoil-flap configuration will be investigated.



- (a) During the upward motion of the fliperon a vortex is generated.
- (b) During the downward motion the vortex is released and pushed into the boundary layer.

Figure 2.8: Schematic drawing of vortex generation by means of a fliperon.

2.3 Governing parameters

In the previous section several different flow control techniques were introduced. In order to compare these techniques to each other and also to compare different flow situations, several dimensionless parameters are introduced. In case of flow control by means of a fliperon the three most important parameters are: the dimensionless frequency F^+ , the momentum coefficient C_{μ} and the ratio of the maximum fliperon deflection over the boundary layer thickness $\frac{A_{max}}{\delta}$. In this section these parameters and their importance will be explained.

2.3.1 Dimensionless frequency

The first parameter that is considered is the dimensionless frequency F^+ . The dimensionless frequency is defined as:

$$F^{+} = \frac{f \cdot x_{TE}}{U_{\infty}} \tag{2.1}$$

In case of flow control with a fliperon f is the oscillating frequency of the fliperon, x_{TE} the distance from the fliperon hinge to the trailing edge of the airfoil and U_{∞} the free stream velocity. For other types of flow control this definition is also used, slightly adapted when necessary. For example in case of a synthetic jet actuator, f is defined as the frequency of the jet.

The dimensionless frequency is closely related to the Strouhal number $(St = \frac{f \cdot L}{U})$ in which f represents the vortex shedding frequency. The Strouhal number can also be seen as the ratio of two length scales: the length scale of the perturbations and the geometrical length scale.

According to Greenblatt [10], the value of F^+ should be of order unity. This conclusion is drawn by examining the amount of momentum that had to be added to get an initially separated flow reattached to a flap surface. It turned out that this momentum minimum occurs around $F^+=1$ and that this value of F^+ does not depend on the

Reynolds number. The detailed analysis of data with respect to flow control experiments in [10] indeed showed that the optimum dimensionless frequency is almost always in the range between 0.3 and 4.

2.3.2 Momentum coefficient

The amount of momentum that is added to the fluid can be expressed using the momentum coefficient [10]. Generally, this coefficient is defined as the ratio of the added momentum to the momentum in the free-stream:

$$C_{\mu} = \frac{\rho_j U_j^2 G}{\frac{1}{2} \rho_{\infty} U_{\infty}^2 L} \tag{2.2}$$

Here j refers to the properties of the jet, G represents the slot width and L the length of the body that is considered.

In the case momentum is added periodically, the jet velocity can be written as the sum of the mean jet velocity and the oscillatory jet velocity: $U_j = \bar{U}_j + u'_j$. In the same way as in equation (2.2) an oscillatory momentum coefficient can be defined as

$$\langle c_{\mu} \rangle = \frac{\rho_j u_j^{\prime 2} G}{\frac{1}{2} \rho_{\infty} U_{\infty}^2 L} \tag{2.3}$$

in which u'_i represents the root mean square of the oscillatory jet velocity.

When both steady and oscillatory momentum are added at the same time the momentum coefficient is written as $C_{\mu} = (c_{\mu}, \langle c_{\mu} \rangle)$.

Finally an oscillatory momentum coefficient is defined for the case in which there is no slot and excitation is achieved by mechanical means:

$$\langle c_{\mu} \rangle = \frac{1}{\frac{1}{2}\rho_{\infty}U_{\infty}^{2}L}\rho_{\infty}\int_{0}^{\infty}u'^{2}dy$$
 (2.4)

Here u' is the oscillatory velocity component adjacent to, and downstream of, the actuator.

Equation (2.4) is also the definition of the momentum coefficient that is used in this thesis, because the fliperon clearly is a mechanical device that adds momentum to the flow. Since the oscillatory momentum is the only momentum that is used here, also the notation C_{μ} will be used for the definition of equation (2.4).

The oscillatory velocity component is just the difference in flow velocity parallel to the surface between the situation in which no flow control is applied and the situation in which the fliperon is active. Here the momentum coefficient is always calculated on a line that is perpendicular to the airfoil surface. This line is located about 1%c behind the fliperon, such that the momentum input can be measured before it starts dissipating. Because the addition of momentum varies with the phase of the fliperon motion, the root

mean square of the velocities is used in the calculation of the momentum coefficient.

From the collected experimental data in [10], it turns out that the average momentum coefficient needed to reattach the separated flow over a deflected flap is approximately in the range $0.01\% < C_{\mu} < 3\%$. This range is a guideline for almost all forms of excitation, except steady blowing and acoustic excitation.

2.3.3 Amplitude ratio

The last dimensionless parameter discussed here is especially useful in case of flow control by means of a fliperon. The amplitude ratio is defined as:

$$Amplitude\ ratio = \frac{A_{max}}{\delta} \tag{2.5}$$

in which A_{max} is the maximum fliperon amplitude, in other words the maximum distance of the fliperon tip to the airfoil surface (measured perpendicular to the airfoil surface). δ represents the boundary layer thickness at the location of the fliperon.

The amplitude ratio is not that often used in literature, since there are many forms of flow control in which there can not be spoken about an amplitude or deflection. However, the parameter is important because it helps in determining the size of the fliperon. Once the value of the amplitude ratio with which effective flow control can be applied is known, the maximum fliperon amplitude becomes fixed. Combined with a chosen maximum fliperon deflection angle, the length of the fliperon is found.

From other research about flow control with a fliperon [11], [5], it was seen that effective flow control can be obtained with an amplitude ratio of order unity. This seems quite obvious, because the most efficient flow control is obtained when all of the momentum from the fliperon is transferred into the boundary layer. Exciting only the lowest part of boundary layer will not be sufficient to transfer enough momentum at all, while exciting more flow than just the boundary layer does not make sense because the free stream flow is insensitive to the additional momentum.

2.4 Research on flow control and fliperons

In the past years several investigation of flow control with fliperons have been performed. The majority consisted of wind tunnel experiments in which fliperons were applied at different configurations. In this section some of these reference researches will be discussed. For more information related to other forms of flow control, the reader is referred to [10].

The first research that will be discussed here is performed by Nishri [18] and is also mentioned in the overview presented by Greenblatt [10]. It consists of wind tunnel

experiments on a simplified airfoil-flap configuration as shown in figure 2.9. Both the airfoil and the flap are represented here as flat plates. The fliperon is located in the excitation slot at the trailing edge of the main element. It should be remarked here that some important results of this research with respect to te governing parameters were already discussed in the previous section.

The most important conclusion following from this research was that it is possible to reattach an initially separated flow to the flap surface by using an oscillating fliperon. The optimum dimensionless frequency for reattaching the flow (possibly with the occurrence of a bubble of separated flow) has a value of 1.0, although higher frequencies are needed to prevent separation. However, dimensionless frequencies larger than about 4.0 turned out to be ineffective, because the generated flow structures dissipated before reaching the trailing edge of the flap and so flow separation remained. The minimum momentum coefficient that was needed to get the flow reattached was in the order of $C_{\mu} = 10^{-4}$. This turned out to be an order of magnitude lower than the momentum coefficient that was needed to obtain attached flow by means of steady blowing.

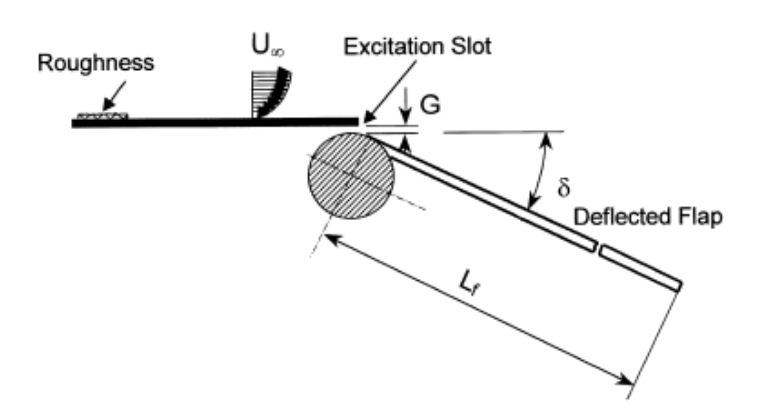


Figure 2.9: Schematic drawing of the simplified airfoil-flap configuration used in [10] and [18].

Interesting research about the application of fliperons is also performed at Delft University of Technology. Artois applied flow control by means of a fliperon on an airfoil-flap model and compared the results with the application of flow control by means of vortex generators [5]. Furthermore this research aimed at revealing the effects of periodic excitation on flow separation.

A springboard type of fliperon was build on the airfoil-flap model, shown in figure 2.10. The performance of the fliperon was measured during several wind tunnel tests. The fliperon was positioned at different locations, in order to find out the influence of the excitation location on the flow.

With respect to the performance of the fliperon it was concluded that flow separation can be postponed by applying flow control with a fliperon. To do so, the fliperon should oscillate at a dimensionless frequency close to 1 and a tip amplitude approximately equal

to the boundary layer thickness. The momentum coefficient was in the order of 10^{-4} . However, the vortex generators performed better in the sense that a higher pressure recovery factor was reached.

About the effects of periodic excitation on the boundary layer it was concluded that the fliperon works as a mixer across the boundary layer. Further it was found that a constant fliperon tip amplitude does not result in a constant momentum coefficient, because $< c_{\mu} >$ also depends on the boundary layer velocity profile which changes in streamwise direction along the model.

Another topic that was investigated was the influence of the excitation location. Unfortunately no general conclusion could be drawn, but it was observed that the fliperon can still be efficient even if it is located quite far ahead of the separation location.

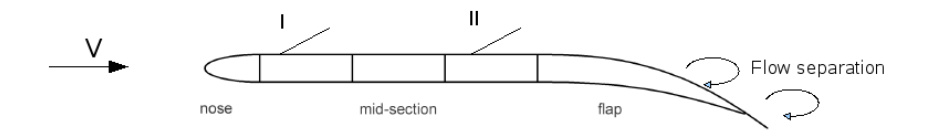


Figure 2.10: Schematic drawing of the airfoil-flap model with fliperons on two different locations as used in [5].

The last reference work discussed here is performed by Van der Jagt, also at Delft University of Technology [11]. In this experimental work flow separation from a ramp is investigated and the flow control is performed by means of a fliperon. The test setup is shown in figure 2.11. For comparison, flow control is also applied by means of two different types of vortex generators.

From the experiments it turned out that the fliperon was able to eliminate flow separation at the backside of the ramp completely. This was a better result than obtained with the normal vortex generators. Only the sub-vortex generators performed better; with these devices the highest recovery factor was found. The optimum fliperon parameters were a maximum tip amplitude of 1.25δ , and a dimensionless frequency of 1.2. However, this was the maximum frequency that the system could reach. Possibly a higher frequency would give even better results. The momentum coefficient that was found for this case was in the order of 10^{-3} .

Further it was found in this work that the effectiveness of the flow control decreases with increasing distance between the fliperon and the separation point. The possibility of making a cavity in the surface was also considered. It was found that a small cavity does not have any negative effects on the flow control, only the fliperon amplitude had to be increased slightly. If the cavity is too large, problems occur with the formation of the vortex at the fliperon tip.

Finally, the PIV measurements explain how the periodic excitation can eliminate separation (see also figure 2.8). During the upward motion of the fliperon, a vortex is formed. This vortex consists of smaller scale structures with a negative vorticity. The vortex causes

separation near the wall, resulting in the formation of small scale structures with a positive vorticity. During the downward motion of the fliperon both small scale structures mix and momentum can be transferred.

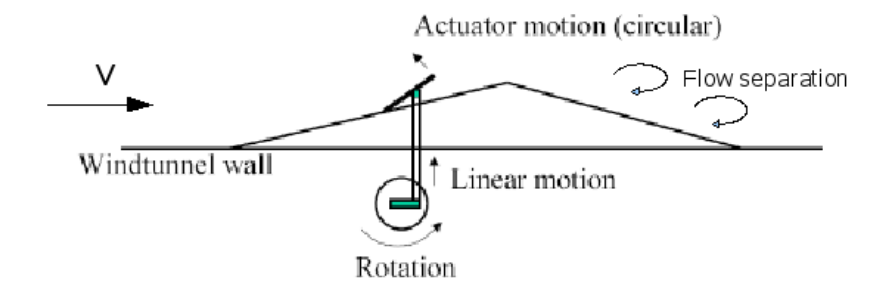


Figure 2.11: Drawing of the test setup used by Van der Jagt [11].

A summary of the discussed flow control methods is presented in table 2.1. This table also presents an indication of the order of magnitude of the increase in lift coefficient that can be expected with each method. However, for all methods hold that their effectiveness can well be outside this range, depending on the implementation in the configuration and the flow situation. Table 2.1 shows that the fliperon can also be an effective flow control device, so it is worthwhile to investigate it in more detail.

Table 2.1: Overview of flow control methods and corresponding order of lift coefficient increase.

Type	Flow control method	ΔC_L (%)	
Passive flow control	Vortex generators	[13],[6]	5 - 30
	Turbulators	[6]	10 - 15
	Self-activated movable flap	[20]	10 - 15
Active flow control	Boundary layer suction	[24],[7]	10 - 30
	Periodic excitation	[10],[15],[19]	10 - 25
	Synthetic jet	[16],[12]	20 - 40
	Deforming surfaces	[22],[21]	5 - 15
	Fliperon	[18],[10]	10 - 30

Setup of the numerical simulations

Modern flow solvers have a lot of adjustable parameters that influence the convergence and accuracy of the solution. Hence a good simulation can only be performed when the choices for the required parameters are based on a correct physical and numerical argumentation. The physical background was already discussed in chapter 2, so in this chapter the focus will be on the background of several numerical principles.

In close relation with the numerical background information, this chapter will also explain how the numerical simulations for this thesis work are set up. First of all the generation of the grids is discussed in section 3.1. In this thesis several different configurations will be studied that all require their own grid. However, each grid is build according to the guidelines explained in this section. After that the setup of steady simulations is discussed in section 3.2. In this section the boundary conditions are introduced, just as the turbulence models. Further quite some attention will be paid to the choices for the solver settings. In many cases the steady simulations will only serve as the starting condition for an unsteady simulation in which flow control by means of a fliperon can be applied. These unsteady simulations and the required dynamic mesh model will be discussed in section 3.3.

3.1 Grid generation

For the grids used in this thesis work, the grid generation software Gambit 2.4 will be used [4]. In this section the grid generation for an airfoil-flap configuration is explained. However, the generation of a grid for a single element airfoil can be done in exactly the same way. For other configurations these guidelines can also be followed, although adaptions will have to be made.

3.1.1 General grid shape

The outer boundary of the grid consists of two parts: a conical shaped front side and a straight backside, as is shown in figure 3.1. This shape has proven its effectiveness in many

airfoil flow simulations [4] and is therefore also used in this case. The grid should be large enough to cover the flow disturbances created by the airfoil. Furthermore the grid should be large enough to prevent reflections from the outer edges of the grid to influence the flow around the airfoil. For simplicity it is assumed here that the airfoil has a unit chord length and that the most forward point of the airfoil is in the origin of the coordinate system. Then the most forward point of the conical grid front side is located at (-15,0), while the rear ends of the conical section are placed at (15,15) and (15,-15). The straight backside is nothing more than the connection between the endpoints of the conical edge.

In order to keep the number of cells in the farfield limited, the farfield is virtually split into two domains. This means that a smaller, but equally shaped cone is placed into the main domain. The most forward point of the subdomain is (-5,0), with the endpoints placed at (5,5) and (5,-5). It should be clear that the subdomain is only a tool used during the mesh generation; it has no physical meaning and does not result in some sort of boundary in the numerical simulation. The grid in the subdomain is closer to the airfoil and will therefore be more dense; the grid outside the subdomain can be coarser since it is further away from the airfoil.

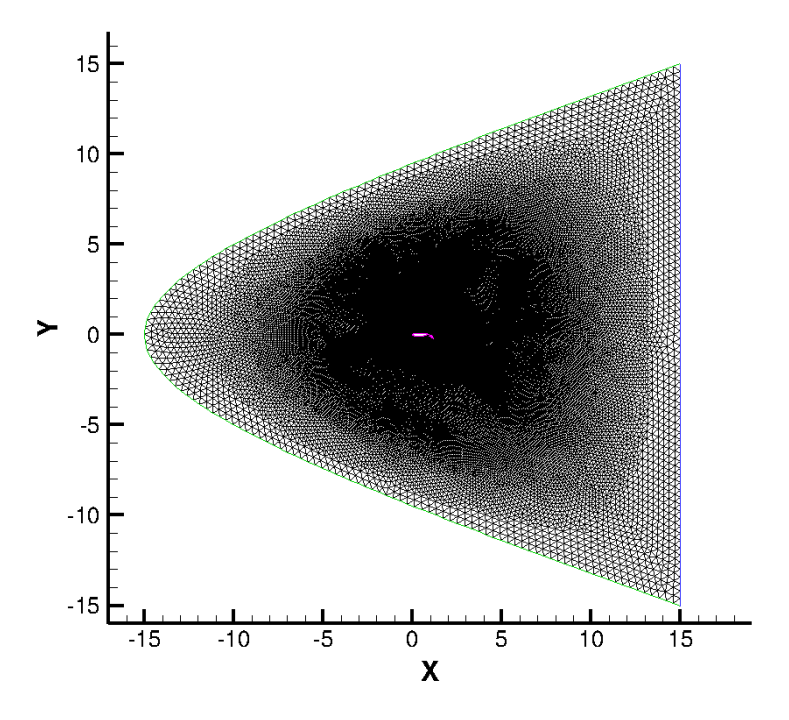


Figure 3.1: The complete grid with the conical shaped front side in green and the straight backside in blue. The airfoil surface is coloured magenta.

3.1.2 Grid elements

The grids constructed for this thesis work turned out to contain about 400.000 cells which can be subdivided into two types: quadrilateral cells that are used close to the airfoil surface and in the wake area, and triangular cells that are used in the rest of the domain (see figure 3.2). The quadrilateral cells form a boundary layer grid around the airfoil. This boundary layer grid has a height of 0.025c, such that it is slightly larger than the maximum expected thickness of an attached turbulent boundary layer. The number of cells in the direction perpendicular to the airfoil surface depends on the airfoil geometry and the flow situation. Considering an airfoil-flap configuration, separation is most likely to occur on the flap and possibly also on the trailing edge of the main airfoil. The flap boundary layer therefore consists of 30 cells perpendicular to the surface, growing with a ratio of 1.04. The boundary layer on the main airfoil consists of 19 cells with a growth factor of 1.06. At the trailing edge of the main airfoil this boundary layer continues and comes on top of the flap boundary layer.

In order to be able to simulate the wake area correctly, a fine grid with quadrilateral cells is required. Therefore an additional block with quadrilateral cells is placed on top of the boundary layer grid on the upper side of the airfoil configuration. This block starts on the first halve of the main element and continues above the flap boundary layers till a distance of several flap chords behind the flap. At the trailing edge of the flap also a block with quadrilateral cells is placed to capture the wake flow from the flap.

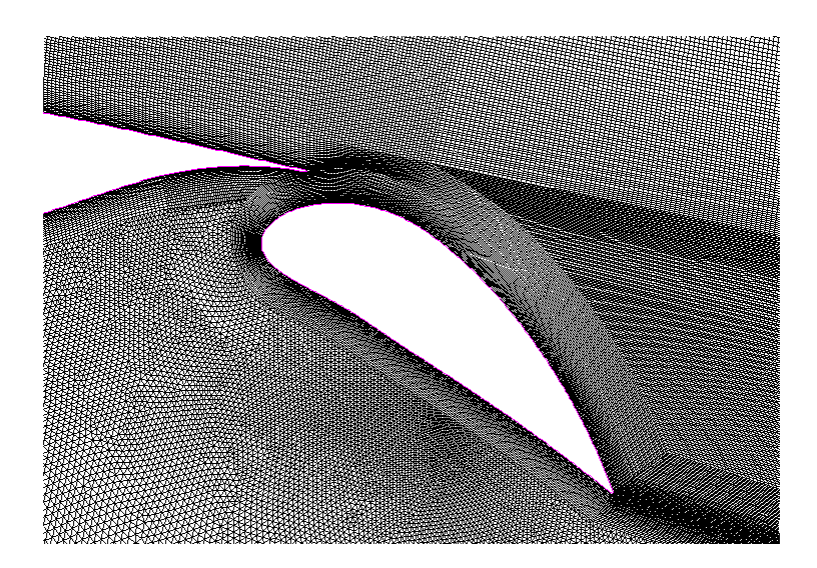


Figure 3.2: Quadrilateral cells on and close to the flap surface, while triangular cells cover the nearfield and the farfield

The dimensions of the cells in the boundary layer grid are of extreme importance for

the correct simulation of turbulent flows. If the first cell layer is not small enough, the simulation of the aerodynamic forces on the airfoil will become less accurate. A parameter that can be used to estimate the size of the boundary layer cells is the y^+ -value which is defined as:

$$y^{+} = \frac{\rho u_{\tau} y}{\mu} \tag{3.1}$$

Here u_{τ} is the friction velocity (= $\sqrt{\tau_w/\rho_w}$) and y is the distance from the center of the cell to the airfoil surface. From this definition it becomes clear that increasing the cell height in the boundary layer results in a larger y^+ -value. For the Spalart-Allmaras turbulence model and other turbulence models with standard or non-equilibrium wall functions acceptable values are in the range $30 < y^+ < 300$ [3]. Figure 3.3 shows the y^+ -distribution over an airfoil-flap configuration obtained with the current grid. It can be seen that the y^+ value is larger than 30 at most locations, but the condition is not satisfied everywhere. However, it turned out that increasing the y^+ -values in these areas by means of increasing the first cell height leads to less accurate simulation results. Decreasing the cell height and increasing the number of boundary layer cells, however, did not lead to better simulation results. Also with the grid adaptation tool of Fluent no grid improvements were found. Therefore it was decided that the current boundary layer grid is sufficiently fine and that it satisfies the y^+ -guidelines.

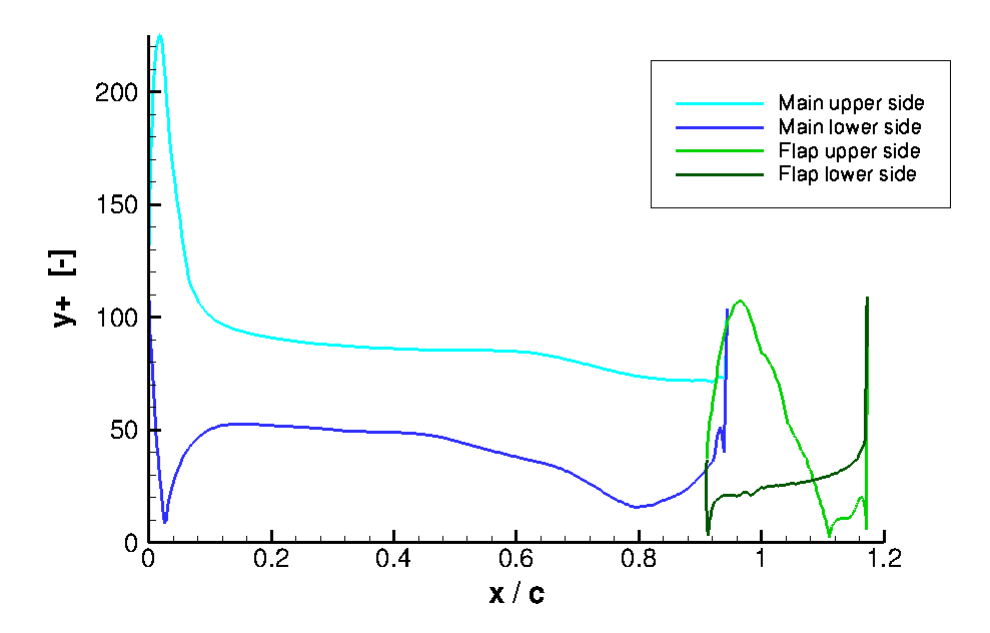


Figure 3.3: y^+ -values for the upper and lower side of the main element and the flap. Note that flow separation occurs on the trailing edge of the flap. The simulation was based on the realizable $k - \epsilon$ turbulence model with standard wall functions.

Outside the boundary layer the unstructured grid in the nearfield and in the farfield consists of triangular cells. An unstructured grid was chosen for several reasons. First of

all, an unstructured grid decreases the simulation time. With an unstructured grid it is possible to refine the grid only in specific areas close to the airfoil, while the farfield can be meshed much coarser. This leads to a decrease in the number of grid cells and so a reduction in computation time.

Another reason for choosing an unstructured grid is the geometry of the airfoil-flap configuration. Since the geometry results in some badly shaped areas, it becomes complicated to create a structured grid. In this case the generation of an unstructured grid will be easier, faster and will result in a better grid with less cells having a high skewness.

The last point considered in meshing the nearfield and the farfield is numerical diffusion, which is a source of errors in numerical simulations. The error can be limited by increasing the number of grid cells. Furtermore the numerical diffusion is minimized when the flow is aligned with the grid. However, outside the boundary layer it is not possible to determine the direction of the flow a priori. Because an unstructured grid is neither aligned nor non-aligned with the flow, it is suitable for meshing the nearfield and the farfield.

3.2 Setup of steady simulations

The flow calculations in this thesis work are all performed with the numerical flow simulation program Fluent 6.3.26. In this section will be explained which boundary conditions are used in the simulations, how the turbulence in the flow is taken into account and which solver settings are used. This section concentrates on the steady simulations, which will be the starting point of the unsteady simulations (discussed in section 3.3). It must be remarked here that these sections only provide a summary of the most important parameters and settings. For more information the reader is referred to the Fluent documentation in [3] and [4].

3.2.1 Boundary conditions

In the current grid three different boundaries occur: the conical front side, the straight backside and the surfaces of the airfoil and the flap. For each of these boundaries the boundary conditions will be discussed now.

The surfaces of the airfoil and the flap (both upper side and lower side) are categorized as wall boundaries. The standard settings for wall boundaries are maintained: the walls are solid, stationary and the no-slip conditions must be satisfied at the surface.

The conical shaped front side of the grid is categorized as pressure-inlet boundary. The boundary conditions that are prescribed at this boundary have a large influence on the flow through the whole domain; in fact these conditions determine the velocity of the incoming flow, the direction of the flow and the level of turbulence. The first parameters that have to be specified are the total gauge pressure and the initial gauge pressure. A gauge pressure can be seen as the difference between the operating pressure and the

actual pressure. From the Mach number at which the simulation should be performed, the pressure inputs at the inlet can be calculated using the isentropic relation

$$\frac{p_0' + p_{op}}{p_s' + p_{op}} = \left(1 + \frac{\gamma - 1}{2}M^2\right)^{\frac{\gamma}{\gamma - 1}} \tag{3.2}$$

Here M is the Mach number and the 'indicates a gauge value, which is the value that can be entered as boundary condition. Further p_{op} represents the operating pressure, which is set at 101325 Pa. The simulations with the airfoil-flap configuration in chapter 6 are performed at a freestream Mach number of 0.185. From equation (3.2) follows that this Mach number is obtained when the initial gauge pressure is set to zero and the gauge total pressure is set at 2448.335 Pa.

Next to the pressure, the direction of the incoming flow is specified on the pressure-inlet boundary. Depending on the angle of attack of the configuration, the x- and y-components of the fluid velocity should be specified here.

The last parameters that are specified are related to turbulence. However, the requested parameters depend on the chosen turbulence model. Therefore these boundary conditions will be discussed in section 3.2.2.

The straight backside boundary is categorized as pressure outlet boundary. The standard backflow settings are maintained, which means that the gauge pressure is zero and the backflow direction is perpendicular to the boundary. The boundary conditions with respect to turbulence are always set equal to the boundary conditions on the pressure inlet boundary.

Although it is not a real boundary condition, some attention has to be paid to the modeling of the fluid. In this case the fluid is air, and compressibility effects have to be taken into account because the maximum Mach number in case of the airfoil-flap configuration of chapter 6 is about 0.5. Therefore the fluid is modelled as ideal gas, with the viscosity calculated according to Sutherland's law.

3.2.2 Turbulence modeling

In the simulation of the flow over an airfoil the turbulence in the boundary layer should also be taken into account. The velocity fluctuations that occur in turbulent flows cause mixing of transported quantities like energy and momentum. Since these fluctuations can be of small scale and high frequency, it will be impossible to calculate them exactly with the current state of numerical flow solvers and computational power. Therefore modern flow solvers like Fluent solve an average form of the Navier-Stokes equations combined with a turbulence model to provide sufficient equations to express all the unknown variables in known quantities [3].

In the simulations performed for this thesis work the Reynolds Averaged Navier-Stokes (RANS) equations are solved. These equations prescribe the transport of the averaged

flow quantities for all scales of turbulence. The computational requirements are now orders of magnitude lower, while the accuracy of the solution is more than sufficient for engineering applications.

Because there is no uniform turbulence model that provides the solution for all applications, Fluent contains several turbulence models with a different number of equations and so a different accuracy. The turbulence models considered for simulating the flow around the airfoil-flap configuration are: the Spalart-Allmaras model (1 equation), the realizable $k - \epsilon$ model (2 equations) and the shear-stress transport $k - \omega$ model (2 equations). These models will be described briefly in this section. For more information about the physical background of these models, the reader is referred to [8] and [4], [3].

The Spalart-Allmaras (S-A) model is used often in simulations of flow around airfoils and should give particularly good results for boundary layer flows with adverse pressure gradients. Here the *strain/vorticity-based production* option is turned on (considers both the generation of vorticity near walls and the mean strain as sources of turbulence), in order to get a more accurate simulation of the production of turbulence. Further all constants are left at their default values. As boundary condition only the turbulent viscosity ratio has to be prescribed. This ratio was set at a value of 10, which is quite reasonable for external flow around airfoils [3].

The realizable $k-\epsilon$ model is quite a new version of the traditional $k-\epsilon$ model that is used in many engineering applications. The main differences are the way in which the turbulent viscosity is formulated and the way in which the transport equation for the dissipation has been derived. Further the term realizable means that mathematical constraints on the Reynolds stresses are satisfied consistent with the physics of turbulent flow. Within the $k-\epsilon$ model several wall functions can be used. Unless stated otherwise, the standard wall functions are used and all constants are maintained at their default values. These default values should lead to the best results in a range of conventional flow situations [3], to which also the performed simulations belong. Since the $k-\epsilon$ model is a 2-equations model, 2 boundary conditions have to be specified. Here it was decided to set the turbulent viscosity ratio at a value of 10 (just like in the Spalart-Allmaras model) and the turbulence intensity at 0.1%, which is a common value for modern wind tunnels.

The last turbulence model considered here is the shear-stress transport (SST) $k-\omega$ model. This model is a combination of the Wilcox $k-\omega$ model [3] and the $k-\epsilon$ model. It should result in reliable turbulence simulations for flows with adverse pressure gradients, flows around airfoils and transonic shock waves. When the model is used here the standard settings of Fluent are maintained, which means that only compressibility effects are included in the simulation. Again it is assumed that the performed simulations do not deviate too much from the range of conventional flow situations for which the model constants are optimized. The boundary conditions that are specified for the $k-\omega$ model are exactly the same as those specified for the $k-\epsilon$ model: the turbulent viscosity ratio is set at 10 and the turbulence intensity at 0.1%.

3.2.3 Solver settings

The physical problem is completely defined now, so the solver settings can be specified. First of all, the pressure based solver is used because this case belongs to the low-speed regime. The gradients are computed according to the Green-Gauss node-based evaluation, which means that the values at a node are calculated from the weighted average of the cell values that surround the node. Especially on an unstructured grid this approach is more accurate than the cell-based gradient evaluation.

For the starting simulations and the less complicated geometries the pressure-velocity coupling is set at coupled. For the airfoil-flap configuration the pressure-velocity coupling had to be changed to simplec, with zero skewness correction. The simplec coupling results in a segregated solving approach, in which the momentum equation and the pressure correction equations are solved separately. The coupled option solves the momentum equation and the pressure-based continuity equations together, leading to faster convergence. However, in complicated flow cases the coupled solver will encounter more problems in obtaining a (converging) solution. Therefore the simplec coupling was used in the airfoil-flap simulations.

In all cases under-relaxation factors are specified for the flow variables. These relaxation factors control the maximum change of the variables between two iterations. This is necessary because the equations that are solved are non-linear and large jumps in the values of the flow variables can deteriorate the convergence of the solution. For difficult flows with a lot of separation the under-relaxation factors need to be set at lower values. When the coupled solver is used, relaxation factors can also be specified for the pressure and the momentum equation in order to improve convergence.

The pressure is the only variable for which the standard discretization provides accurate results. For all other variables, including the turbulence variables, a second order upwind scheme is used. This has to do with the unstructured type of grid: since the flow is never aligned with the cells second order discretization is needed to limit the numerical diffusion. Although second order discretization schemes generally converge slower than first order schemes, they are used here because they will finally result in a more accurate solution.

The last aspect of the solver settings that should be discussed is the Full Multigrid (FMG) initialization. This initialization is used to start the simulation with a better initial solution and so obtain faster convergence. First a number of grid levels is constructed from the grid. Level zero is just the fine grid as it was, while at each higher level the grid becomes coarser. The initial solution is transported to the coarsest grid level. At the coarsest grid level a number of iterations is performed, till the convergence criterion or the maximum number of iterations is reached. The new solution is transported to the next, slightly finer grid level. The residuals that were calculated on the coarser grid are used to obtain a correction term for the solution on the finer grid level. Again a number

of iterations is performed, every time transporting the intermediate residuals from the current grid level to the coarsest grid level and the corrections from the coarsest grid level to the finer level. When sufficient convergence is reached, the solution is transported to a finer grid level. Also from this new level the intermediate residuals are transported down to the coarsest grid level while the corrections are transported up to the new level. This process is repeated till sufficient convergence on the finest grid level is reached.

The equations that are solved in FMG initialization are the inviscid Euler equations. These equations are first order discretized, making the FMG initialization an efficient process. In a small amount of additional time a much better initial solution is obtained, which will reduce the calculation time for the final simulation considerably.

3.3 Unsteady simulations with dynamic meshes

In the previous section the setup of the steady simulations was discussed. The results of the steady simulations are often used as starting point for the unsteady simulations. This means that all settings like the boundary conditions, the turbulence model and the solver settings remain unchanged in the unsteady simulations. The main difference is that now also the time-domain is discretized and a solution is calculated at each time.

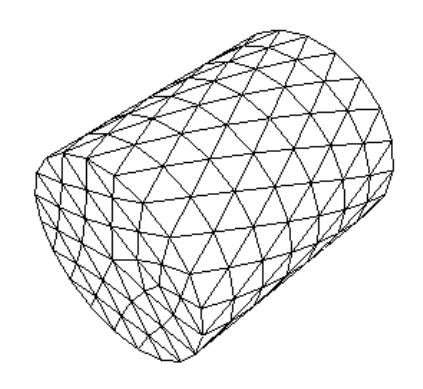
When flow control by means of an oscillating fliperon is applied, things get a little more complicated. In this case the dynamic mesh model has to be used, which handles the motion of the fliperon and the corresponding changes in the grid. In the first part of this section the dynamic mesh model will be introduced and its operating principles will be explained in general. In the second part of this section will be discussed how the dynamic mesh model can be used to simulate the oscillating fliperon on an airfoil configuration. Appendix A provides some additional information about the used settings for the dynamic mesh model.

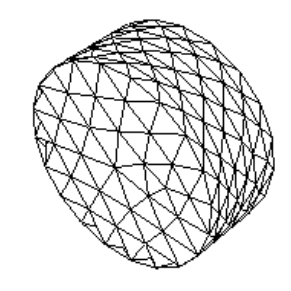
3.3.1 Dynamic mesh model

When some part of the configuration that is simulated is moving, the mesh that is attached to those surfaces should change as well. Fluent provides three different groups of methods for mesh motion. These groups are smoothing methods, dynamic layering and local remeshing methods. It is also possible to use a combination of methods or to use all three groups of methods simultaneously.

The smoothing methods consist of spring-based smoothing and Laplacian smoothing. In the spring-based smoothing method the edges between the grid nodes are seen as springs with a spring constant. Before the motion starts, the network of springs is assumed to be in equilibrium and all spring forces are zero. When a surface starts moving, the grid nodes on the surface are displaced and spring forces arise. The spring-based smoothing method now displaces the interior grid nodes such that a new equilibrium is found in which the spring forces are eliminated. An example of spring-based smoothing is shown in figure 3.4. Laplacian smoothing is a more simple and faster smoothing method. The new location of

each grid edge is adjusted to the geometric center of its neighbour vertices. To assure a mesh of good quality, the edge is only displaced if the skewness of the cell will improve. This methods works in 2D only for zones with linear grid elements.





- (a) Grid at the start of the motion.
- (b) Smoothed grid at the end of the motion.

Figure 3.4: An example of spring-based smoothing for a cylindrical cell zone where one end of the cylinder is moving [3].

The dynamic layering method can be used to control the height of cell layers in a structured grid area. On the moving surface, an ideal cell height is prescribed. Further a split factor and a collapse factor should be specified. If a layer of cells becomes smaller than the product of the collapse factor and the ideal cell height, the layer of cells is merged with the next layer. In the same way, if a layer of cells becomes larger than one plus the split factor times the ideal cell height, the layer of cells is split into two new layers. If the displacement of a surface is large compared to the local grid cell size, the quality of

If the displacement of a surface is large compared to the local grid cell size, the quality of the grid cells can decrease rapidly and negative cell volumes might occur. To prevent this, the remeshing methods can be used. These methods evaluate all cells and mark the cells that should be remeshed on one or more of the following criteria: the cell is larger than the maximum length scale that is specified, the cells is smaller than the minimum cell height that is specified or the cell skewness is higher than the maximum skewness specified. It is also possible to use a size function to specify the remeshing criteria. However, it is important to note that the remeshing methods can only be applied in grid zones with triangular cells.

Once the mesh motion is specified, it is important to indicate the motion of each zone in the grid. Fluent provides 4 types of motions:

• Stationary motion. This motion type can be used to explicitly declare that a zone is stationary. This means that the elements on this zone are not changed when the grid is updated to the next time step. This motion can be prescribed for grid

nodes that belong to both a moving and a non-moving grid zone. By default, the position of these nodes is allowed to change during the mesh update, but specifying the non-moving zone as stationary will prevent this.

- Rigid body motion. The motion of a grid zone can be classified as rigid body motion when the zone is rotating or translating. A user-defined function that prescribes the motion of the zone is required in this case. This user-defined function is nothing more than a function written in the C programming language, that prescribes for example the angular velocity of the rigid body. Next to the user-defined function, the location of the center of gravity of the rigid body and its initial rotation angle have to be specified. It should be remarked that this center of gravity is not the physical center of gravity that follows from the mass distribution, but just the reference point to which the motion is specified.
- Deforming motion. If the motion of a grid zone is classified as deforming motion, the shape of that grid zone and the positions of all nodes that belong to the grid zone are allowed to change. In the same way as the dynamic mesh specifications, smoothing and remeshing can be activated for this zone.
- User-defined motion. With this type of motion it is possible to simulate deforming surfaces that are moving as well. This is done again by means of a user-defined function. Because this type of motion is not used within this thesis work, details are omitted here. For more information the reader is referred to [4].

3.3.2 Application to fliperon motion

In the current thesis work the dynamic mesh model is used to simulate the oscillating fliperon on an airfoil configuration. As was already explained in section 2.3.3, the maximum deflection of the fliperon will be in the order of the boundary layer thickness. Considering the grid as presented in section 3.1.2, it is clear that the fliperon will move straight through the boundary layer grid of quadrilateral cells. However, the displacement of the fliperon tip is large compared to the size of the grid cells. This means that smoothing methods become incapable and that the use of remeshing methods will be necessary in order to prevent negative cell volumes. Since remeshing methods can only be applied on triangular grid cells, the boundary layer grid near the fliperon is adapted. As is shown in figure 3.5, the fliperon is placed in a block of triangular grid cells. By means of spring-based smoothing and remeshing the grid around the fliperon should remain a high quality grid.

As explained in the previous section, it is important to specify the motion type of each grid zone. In the current work the fliperon is classified as rigid body, whose motion is prescribed by a user defined function. This function prescribes the z-component of the angular velocity vector, ω_z , as a function of time. In most cases a sine-shaped motion of the form $\omega_z = a \cdot \sin(b \cdot t)$ is prescribed. In appendix A.1 an example of a user-defined

function can be found.

Further the fluid zone is the only zone that is classified as deforming. For this zone smoothing and remeshing are activated with the same parameters as used in the dynamic mesh model. All other zones, including the airfoil surfaces and the farfield boundaries, are classified as stationary. These zones are now no longer influenced by the dynamic mesh model. A summary of the specified parameters for the dynamic mesh model can be found in appendix A.2.

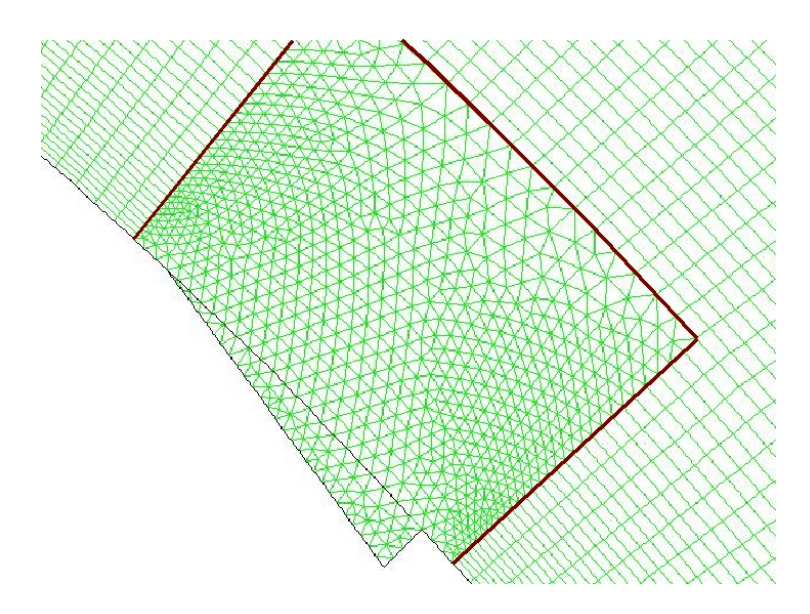


Figure 3.5: A block of triangular cells is located around the fliperon in order to enable the use of remeshing methods for updating the grid.

It is interesting to see how the dynamic mesh model operates in a simulation. Therefore an airfoil-flap configuration with an operating fliperon on the flap upper surface will be examined in several steps now. In figure 3.5 the starting situation at time $t_0=0$ is shown. This starting situation is equal to the solution of the steady simulation. In the starting situation the fliperon is aligned with the flap surface and so its deflection angle is equal to zero

Now the unsteady simulation can start. First of all, the actual time is calculated. For the first time step this will simply be t=0 and for each next time step holds $t_{new}=t_{old}+\Delta t$. With the actual time the angular velocity of the fliperon is calculated from the user-defined function. Then the change of the fliperon deflection angle is calculated by intergrating the angular velocity over the time. This difference is added to the old deflection angle to obtain the new fliperon deflection. The fliperon is moved to its new position and then the grid needs to be updated. Because remeshing is used, it is possible that cells split or merge so the number of cells and nodes can change during the grid update. When the grid is updated successfully, the solution of the previous time step is interpolated on the new grid. Now a number of computational iterations is performed to calculate a new solution for the modified configuration. When this solution is converged, the whole process starts again

from the beginning. So the new time is calculated, a new angular velocity is calculated from the user-defined function, the velocities are integrated to obtain the new fliperon deflection angle, the grid is updated and the solution for the next time step can be calculated.

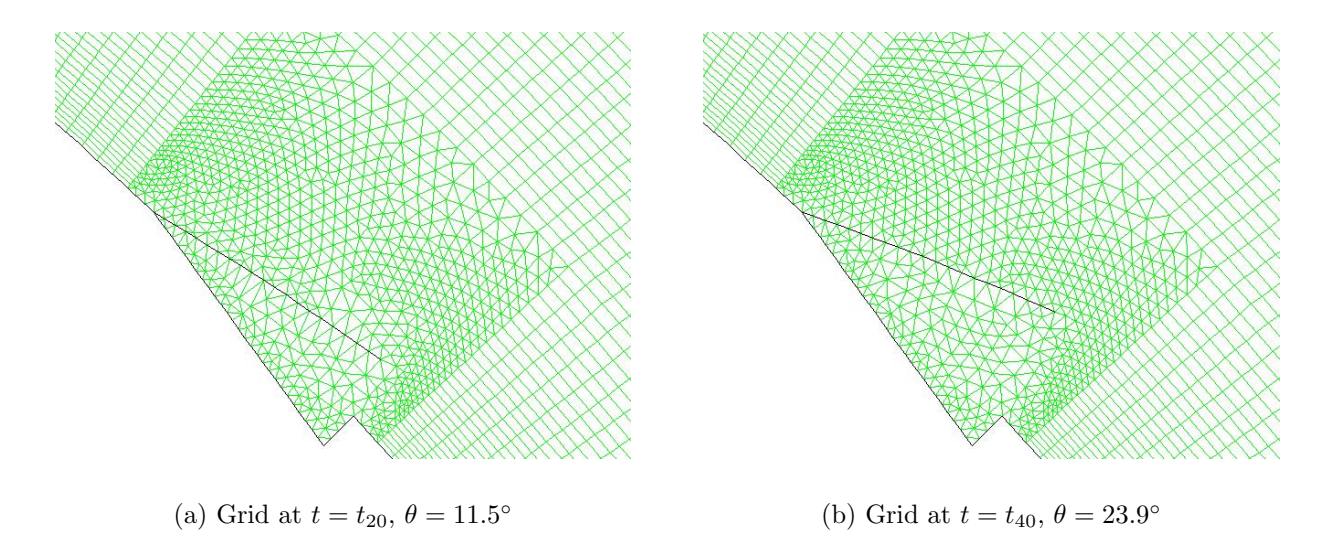


Figure 3.6: Spring-based smoothing and remeshing update the deformed grid such that each time step the flow calculations can be performed on a grid of sufficient quality.

Some steps in this process require a bit more explanation. It was mentioned that the fliperon deflection angle is calculated each time step by integrating the angular velocity. If many time steps are simulated, this may lead to some sort of drift that is caused by small errors in the numerical integration. This would mean that after a number of fliperon oscillations, the fliperon does not return exactly to the position from which it originally started. However, this drift can be easily prevented by using sufficiently small time steps. In the current simulations time steps of order $10^{-5} s$ and $10^{-6} s$ are used and it turned out that the fliperon drift was indeed very small and could be neglected.

Another interesting step is the grid update. Each time step the fliperon and the grid nodes that lie on the fliperon rotate to a new position. Consequently, the cells that are connected to the moving nodes are deformed. The spring-based smoothing and the remeshing should improve the quality of the deformed cells when needed. Figure 3.6 shows the same grid as figure 3.5 at $t=t_{20}$ and $t=t_{40}$, so after 20 and 40 updates. It can be seen that the grid has changed considerably, but is still of reasonable quality. However, if the fliperon is rotated over a large angle within a single time step, it is still possible that negative cell volumes occur. This always leads to an immediate crash of the simulation. So it is important to monitor the maximum change in fliperon deflection angle per time step, and keep this value below a certain maximum value. This maximum depends on the size of the grid cells and have to be found by experience.

Chapter 4

Flow control on a ramp

In the previous chapter was explained how an oscillating fliperon can be simulated numerically with the flow solver Fluent. However, setting up such a simulation requires some practical experience with the dynamic mesh model. Therefore the current test case is introduced. In this test case the flow over a backward ramp will be simulated. Without flow control, flow separation will occur at the ramp surface. A fliperon will be introduced in order to reattach the flow to the ramp surface.

The current test case is a rather simple case in several ways. First of all, the flow field ahead of the ramp is uniform (except the boundary layer at the walls). This makes it easier to see the effects of the fliperon oscillations on the flow field, because interference with other flow structures will not occur. Second, the boundary layer ahead of the ramp will be thin and therefore it will be easier to excite the complete boundary layer. Further the limited amount of grid cells required in this test configuration will result in short calculation times. Because the primary goal of this test case is gaining experience with the dynamic mesh model, several more physical aspects are not studied here. Although some attention will be paid to the influence of the dimensionless frequency and the amplitude ratio, the influence of the momentum coefficient is discarded in this test case. Also the influence of the size of the fliperon and its location will not be investigated.

4.1 Setup of the test case

As was mentioned before, the geometry of the test case is simple in order to limit the amount of grid cells. This will keep the calculation times as short as possible. The geometry can be seen as a channel, of which the bottom shows a backward ramp, see figure 4.1. The flow enters the channel uniformly from the left side (green border). The blue borders represent solid walls and the green border on the right should be interpreted as the outlet. The Mach number of the freestream flow is set at 0.185 ($V_{\infty} = 64 \, m/s$), which is the same Mach number as is used in the simulations with the airfoil-flap configuration of chapter 6. The Reynolds number based on the ramp length is $4.9 \cdot 10^5$. The ramp angle is chosen such

that separation occurs at the top of the ramp. It turned out that a value of 30° resulted in a well separated flow. The dimensions of the outer walls are chosen such that the walls do not influence the performance of the fliperon. The experimental work of Van der Jagt [11] was used as reference for this setup.

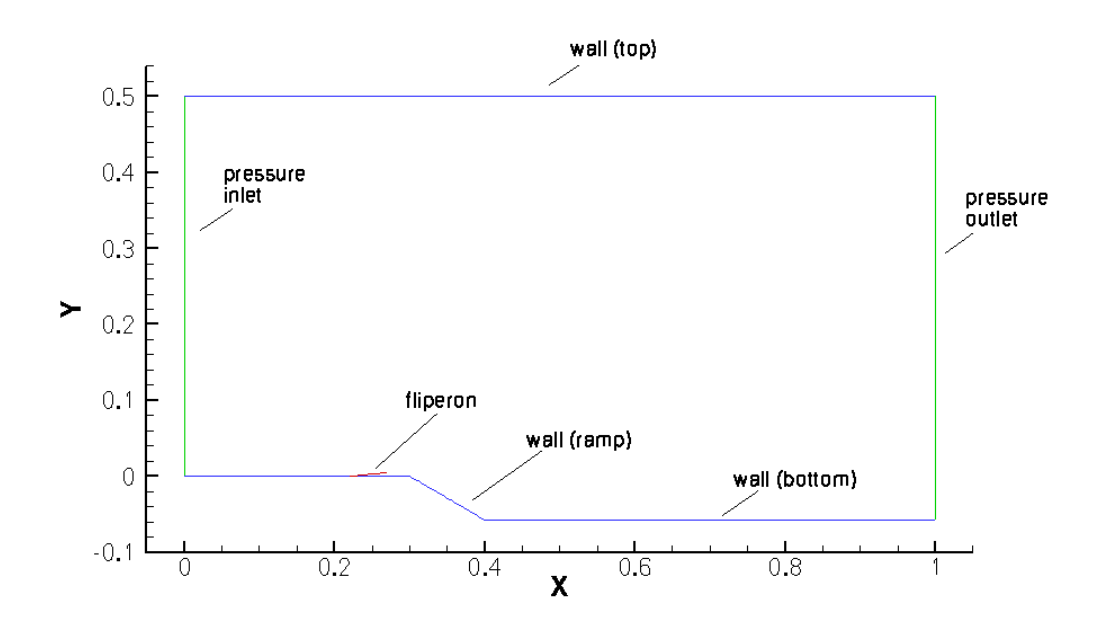


Figure 4.1: Schematic representation of the test case geometry with the fliperon (red) in front of the backward ramp (dimensions in meters).

4.2 Flow field without flow control

Without flow control, the numerical simulation shows clearly that the flow separates at the first part of the ramp. The velocity vectors corresponding to this case are plotted in figure 4.2. It can been seen that over almost the complete ramp the x-component of the velocity is negative. A backflow coefficient can be defined as the percentage of the ramp length on which the x-component of the velocity is negative. In this case without flow control, the backflow coefficient has a value of 89%.

Next to the backflow coefficient a pressure recovery factor can be used to indicate the effectiveness of the flow control. The change in pressure recovery factor is an indication of the change in the flow separation location. When the pressure coefficients over the ramp are plotted, a specific pressure value must be marked for the definition of the pressure recovery factor. In this case a c_p of -0.6 was chosen, because the displacements of the pressure curves are rather large at this value. This will result in a sufficiently large range of pressure recovery factors. The pressure recovery factor is now defined as:

$$pressure \ recovery \ factor = \frac{x - x_0}{L}$$

Here x_0 is the x-location (in meters) at which the graph of the ramp flow without flow control crosses the line $c_p = -0.6$, x the location where the graph of the controlled flow crosses the line $c_p = -0.6$ and L the length of the ramp in x-direction (here 0.10 m).

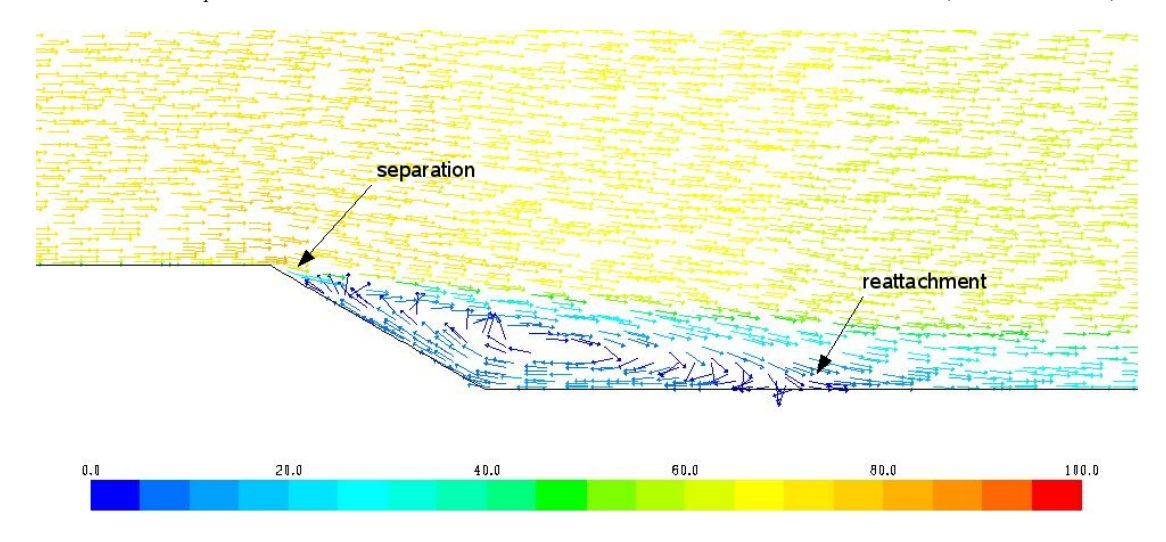


Figure 4.2: Velocity vectors (uniform length, skip factor 4) for ramp flow without flow control. The vectors indicate the direction of the flow velocity, while their colour indicates the magnitude of the velocity (in m/s).

4.3 Controlled ramp flow

In order to control the separated flow over the ramp, a fliperon is placed at an x-location of $0.22\,m$ ($0.7L_{ramp}$ ahead of the ramp) and at an angle of 5.9° with the wall surface. The length of the fliperon is set at $0.43L_{ramp}$. The position and the length of the fliperon are parameters that influence the performance of the fliperon, but these parameters were not optimized in this test case. A reasonable value was simply found by trial and error.

Two other important parameters that determine the effect of the fliperon are the dimensionless frequency and the amplitude ratio. According to Greenblatt [10], a dimensionless frequency of about 1.0 is optimal to get a separated flow reattached to a flap. The amplitude ratio is based on the boundary layer thickness ahead of the ramp, which is in this case about $5 \, mm$. Although amplitude ratios of about 1.0 were marked as optimal in literature (see section 2.3.3), higher amplitude ratios will be used here in order to guarantee sufficient excitation. These higher amplitude ratios will not have a negative effect on the fliperon performance as studied in this test case. An overview of all simulations performed in the test case can be found in table 4.1.

4.3.1 Influence of frequency and amplitude

For the first calculation some average values for the dimensionless frequency and the amplitude ratio were chosen: $F^+ = 1.0$ and $A_{max}/\delta = 3.7$. This resulted in an oscillation

Simulation	F^+	A_{max}/δ	Recovery factor	Backflow coefficient
Basic ramp flow	-	-	0.000	0.89
Fliperon motion 1	1.0	3.7	0.080	0.00
Fliperon motion 2	0.7	3.7	0.120	0.72
Fliperon motion 3	1.3	3.7	0.070	0.00
Fliperon motion 4	1.0	2.6	0.020	0.70
Fliperon motion 5	1.0	4.8	0.125	0.10
Fliperon motion 6	0.7	4.8	0.175	0.58

 Table 4.1: Overview of performed simulations and their results

period of $1.25\,ms$, which was divided in 20 timesteps when running the numerical simulation. After simulating 3 periods, the instantaneous pressure distribution over the ramp is examined. This pressure distribution is plotted with the red line in figure 4.3. Compared to the basic ramp flow (flow without flow control), it can be seen that the minimum pressure has decreased, while the maximum pressure has increased. Further it is clear that the pressure rise takes place more aft on the ramp, which indicates a positive pressure recovery factor of $\frac{0.313-0.305}{0.100}=0.080$. At the same time the backflow coefficient decreases to a value of almost zero, which indicates attached flow on the ramp. However, this is only the case at the instantaneous picture taken $3.75\,ms$ after the start of the fliperon movement. At the end of this section the development of the flow field in time will be discussed further. Not too many conclusions should be drawn from this first simulation, but at least it can be said that the fliperon seems able to influence the flow in a favourable way.

Now the influence of the frequency on the fliperon performance is investigated. The dimensionless frequency is reduced to 0.7 and the same calculation is repeated. The pressure distribution after 3 periods is shown by the blue line in figure 4.3. It can be seen that the range of pressure coefficients is smaller now and that the pressure recovery factor increased to 0.120. The backflow coefficient has now a value of 0.72, which means that still the largest part of ramp faces backward flow. However, as will be seen later on, the backward flow can also be caused by vortices that roll over the surface of the ramp.

When the dimensionless frequency is increased to 1.3, opposite effects can be seen: the range of pressure coefficients increases while the pressure recovery factor decreases to a value of 0.070. The backflow coefficient is now again almost 0, which indicates attached flow. From the pressure distribution in figure 4.3 it is observed that when the pressure coefficient on the ramp surface is large enough, total reattachment will occur instantaneously. Based on these observations, it can also be said that increasing the dimensionless frequency leads to a lower pressure at the start of the ramp, a higher pressure further aft on the ramp and a smaller pressure recovery factor. The opposite holds for a decreasing frequency.

Also the influence of the amplitude ratio of the fliperon is examined, see figure 4.4. Again the first simulation with $F^+ = 1.0$ and $A_{max}/\delta = 3.7$ is taken as starting point. When the amplitude ratio is decreased to 2.6, only the pressure on the last part of the

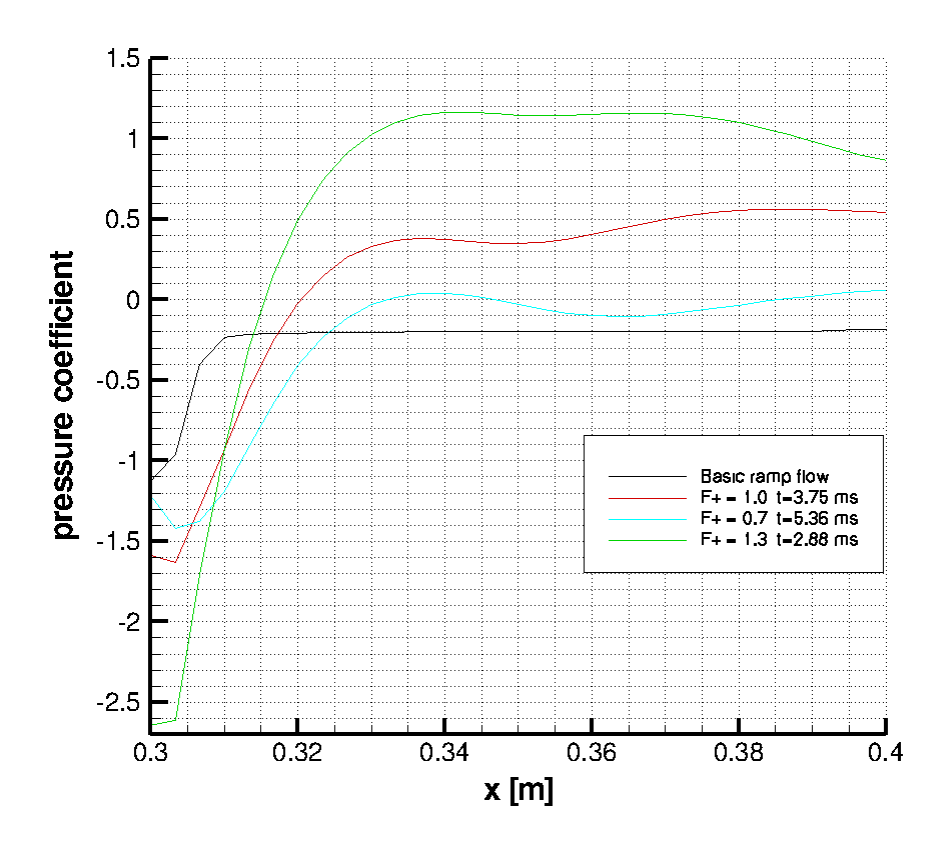


Figure 4.3: Instantaneous pressure distributions over the ramp for fliperon motions with different frequencies, but with a constant amplitude ratio of 3.7.

ramp shows a small increase compared to the uncontrolled ramp flow. The pressure recovery factor is only 0.020 and the backflow coefficient has still a value of 0.70. These are all indications that this lower amplitude is not efficient and that the fliperon does not perform optimal in this case.

Increasing the amplitude ratio to 4.8 shows opposite effects: the pressure range extends considerably and the pressure on the last part of the ramp shows a large increase. The backflow coefficient is reduced to about 0.10, but this backflow is caused by a vortex that rolls over the ramp surface. The pressure recovery factor also shows an increment. It is clear that this larger maximum amplitude has a positive effect on the fliperon performance.

It is observed that no consistent relation between the pressure recovery factor and the backflow coefficient is found in this case. This is caused by the backflow coefficient, that turns out to be incapable of indicating whether the flow is attached to the surface. A large backflow coefficient can have many causes, of which separated flow is one. But also a passing vortex or an enclosed bubble of separated flow can cause an increase in backflow coefficient. This will be explained in more detail in the next section, in which the flow

field is investigated.

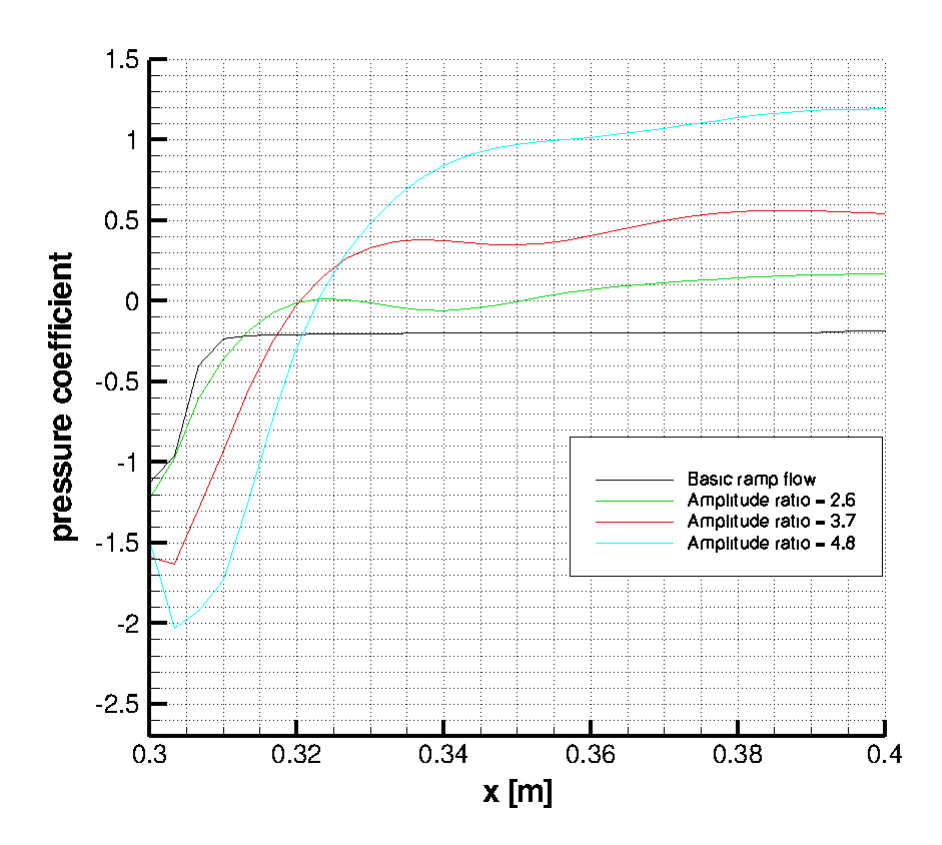


Figure 4.4: Pressure distributions over the ramp at $t=3.75\ ms$ for fliperon motions with different amplitude ratios, but a constant dimensionless frequency of 1.0.

4.3.2 Flow field analysis

An important question that is not answered yet is the question what exactly happens to the flow when the fliperon starts oscillating. This is a complex physical process in which vorticity plays a major role. To answer the question more simulation results are studied. In figure 4.5(a) the flow over the ramp is shown in terms of velocity vectors. This is again an instantaneous view, obtained from simulation 2 ($F^+ = 0.7$ and $A_{max}/\delta = 3.7$) after three fliperon oscillations were performed. Note that the vector length is uniform in this figure; the arrows only represent the direction of the flow. The colour indicates the magnitude of the velocity vectors. In figure 4.5(b) the corresponding vorticity contours of simulation 2 are shown.

In figure 4.5(a) large velocities are seen directly behind the fliperon. Since the fliperon has just finished an oscillation at this time, the large velocities indicate that air is pushed away by the fliperon in a powerful way. At the first part of the ramp a very small vortex

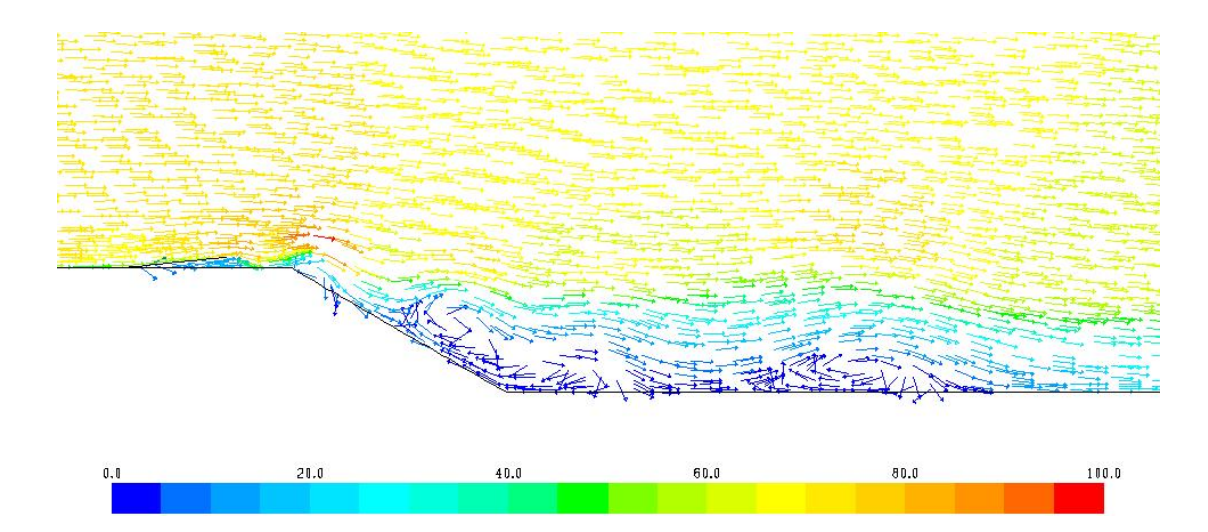
can be seen. This is the clockwise rotating vortex produced during the last oscillation of the fliperon, which is also clearly visible in figure 4.5(b). On the second part of the ramp, the second, much larger vortex is visible. The velocities are still quite small and at the ramp surface the x-velocity is negative. However, this negative x-velocity does not mean that the flow is completely separated. In fact the stream of vortices pushes the flow towards the ramp and the horizontal wall. Thus the vortices are the solution for the flow separation, but also the cause of the negative velocities. This can also be seen on the first part of the horizontal wall after the ramp: the vortex from the first fliperon oscillation is still visible and pushes the flow to the surface. Above the vortices the flow is again more or less aligned with the free stream flow. The non-circular vortex that is visible further aft on the horizontal wall is the residual of the flow that was separated before the fliperon started oscillating. This vortex also causes some negative x-velocities further aft on the horizontal wall.

So now it is clearly shown that each fliperon oscillation produces a vortex. The strength of the vortex will depend on the maximum amplitude and the frequency of the fliperon. The frequency of the fliperon motion will also determine how close the vortices follow-up each other, which will have consequences for the effects on the flow over the ramp. In the simulations it was seen that a larger amplitude ratio seems to have a more favourable effect in terms of increasing pressure on the ramp and a larger pressure recovery factor. Increasing pressure on the ramp can also be obtained by decreasing the dimensionless frequency, which will result in a higher pressure recovery factor as well.

The optimization of the fliperon movement depends strongly on which criteria are seen as most important. For attached flow on the ramp the fliperon motion should be different from the motion that results in the highest pressure on the ramp. The goal for this test case, as was mentioned in the introduction of this chapter, was to obtain attached flow on the ramp surface. Based on the minimization of the backflow coefficient, the optimum parameters are a dimensionless frequency of 1.0 or 1.3, and an amplitude ratio of 3.7. However, when backflow caused by attached vortices is neglected, larger maximum amplitudes can also be seen as optimal.

In order to indicate the performance of the fliperon it is better to use the pressure recovery factor, since that parameters gives a better indication of the change in the separation location that will finally lead to a change in lift if an airfoil is considered. For a maximum pressure recovery factor a dimensionless frequency of 0.7 can be used, or an amplitude ratio of 4.8. The combination of both a frequency of 0.7 and an amplitude ratio of 4.8 is even more optimal: it resulted in a pressure recovery factor of 0.175. Finally it must be remarked here that this is a rather limited optimization, since only several discrete values of the dimensionless frequency and the maximum amplitude are investigated.

The last topic that should be addressed in the discussion of this test case is the time span of the simulations. The simulations presented here all covered three fliperon oscillations, corresponding to time spans between $2.88 \ ms$ and $5.36 \ ms$. The pressure



(a) Velocity vectors coloured by velocity magnitude in m/s, uniform vector length, skip factor 4.

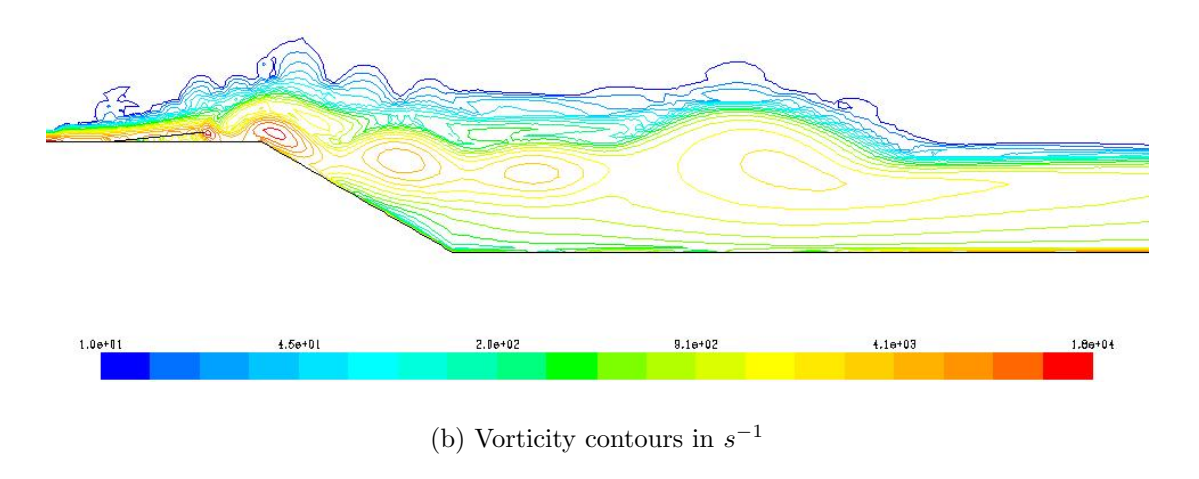


Figure 4.5: Instantaneous flow field of motion 2 after 3 fliperon oscillations ($F^+ = 0.7$ and $A_{max}/\delta = 3.7$).

distributions presented in figures 4.3 and 4.4 are instantaneous distributions, taken after the third fliperon oscillation. A better representation of the pressure distribution would be a time-averaged distribution, which depends to a lesser extend on the current position of the fliperon.

Some simulations have run for a longer time so that the fliperon could perform more oscillations. In general, the instantaneous pressure distributions after 5 oscillations showed some small differences with respect to the pressure distributions after 3 oscillations. The instantaneous pressure distributions after 10 oscillations were however almost equal to

the distributions after 5 oscillations. From these observations follows that the results presented in this section are a good indication of what happens in the flow field, but should not be seen as exact solutions.

Overall, it can be said that this test case has provided the required results. The influence of the fliperon motion on the ramp flow has become clear and the effects of the dimensionless parameters F^+ and A_{max}/δ are established. This provides a sufficiently solid base to apply an oscillating fliperon on an airfoil from which the flow is (partly) separated.

Chapter 5

Flow control on the NACA-0015 airfoil

In the previous chapter flow control by means of a fliperon was successfully applied on a ramp. However, the ramp configuration is rather different from the airfoil-flap configuration on which the fliperon will be applied in the final case. Therefore a second test case is introduced. In this test case flow control by means of a fliperon will be applied on the NACA-0015 airfoil. The results can be compared with numerical results obtained by Munts [16]. In this reference work the separated flow over the NACA-0015 airfoil was successfully controlled by means of a synthetic jet.

This chapter will start with a steady investigation of the flow field around the NACA-0015 airfoil at angles of attack beyond the stall angle. When this flow field is known, flow control can be applied. Section 5.2 discusses the fliperon geometry and its implementation, as well as the influence of the fliperon motion on the flow field. Next to that the results of several unsteady simulations will be presented and discussed. In the last section of this chapter the results will be compared to the results of Munts and conclusions about the effectiveness of flow control by means of a fliperon will be drawn.

5.1 Post-stall flow field

Before any flow control technique can be applied, the flow field around the airfoil should be known. In [16] the $C_L - \alpha$ curve of the NACA-0015 airfoil is investigated in three ways: by means of wind tunnel experiments, by means of the numerical panel code XFOIL and by means of a Navier-Stokes solver called DSS2 code (see also section 5.1.1). It turned out that stall occurs at an angle of attack of about 18°. Since the flow control techniques will be investigated in the post-stall flow field, it is decided to put the NACA-0015 airfoil at an angle of attack of 20° as starting situation for the research.

In this section the results of the steady simulations will be presented. First the reference simulations of [16] will be analyzed and discussed. After that the performed Fluent simulations are explained and the results are compared with the results of the reference simulations. The results of these steady simulations are important for the determination

of the geometrical properties of the fliperon, like the size and the location on the airfoil surface.

5.1.1 Reference work

For the numerical simulations in [16], the DSS2 code is used as flow solver. This code is based on the numerical integration of the full Reynolds-averaged compressible Navier-Stokes equations. The NACA-0015 airfoil is meshed with a C-type structured grid consisting of approximately 28,000 cells.

The flow conditions used in the reference simulations are a Mach number of 0.12 and a Reynolds number of 0.9 million. In these conditions the turbulence is modelled with a modified version of the 1-equation Baldwin-Lomax model [16], called the curvature model.

The reference simulation performed in [16] is a steady simulation. Nothing is remarked about any unsteady effects, although it is likely that some unsteadiness will occur at this high angle of attack. The simulation shows massive flow separation at the given angle of attack of 20°. The flow separation starts around the point x/c = 0.25 and a large region of separated flow covers the aft part of the airfoil. The resulting lift coefficient has dropped to a value of about 0.90. Based on this observation it is concluded that the best location to apply the synthetic jet is at x/c = 0.30.

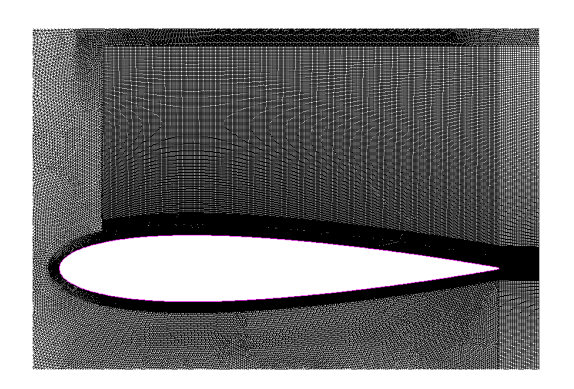
The application of the synthetic jet turns out to be very successful. With optimized settings, an increase in lift coefficient of about 80% can be obtained, which means that the lift coefficient at $\alpha=20^{\circ}$ rises from 0.90 (case without flow control) to about 1.6. In this case the optimized settings consist of the jet angle, the momentum coefficient and the jet oscillation frequency. It turned out that especially a large momentum coefficient results in a large increase of the lift coefficient.

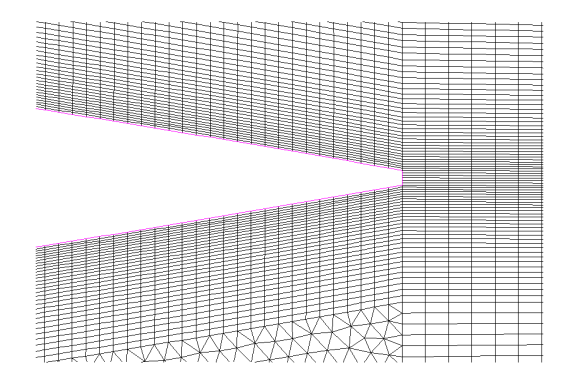
5.1.2 Steady simulations

The setup of the Fluent simulations for the NACA-0015 airfoil is almost equal to the general setup of the simulations as described in chapter 3. This means that the grid used is for the largest part unstructured, with a conical shaped pressure inlet boundary. The grid consists of about 450,000 cells and is shown in figure 5.1. It is clear that this grid is quite different from the grid used in [16], but in well-performed simulations this should not influence the final results.

In order to be able to compare the results at the end, it is tried to keep the conditions for the current Fluent simulations as close as possible to the conditions used in the reference simulations. This means that the freestream Mach number will be 0.12, with a Reynolds number of 0.9 million. This is realized here by assuming an airfoil chord of 0.33 m. The Baldwin-Lomax turbulence model used in the reference simulations is not available in Fluent. It is decided to use the realizable k- ϵ model here, because this model gave good

results in the NLR7301 simulations described in section 6.1. However, since phenomena like flow separation are significantly influenced by turbulence, differences in the outcome of the simulations are expected.





(a) The lower airfoil surface is covered with a single boundary layer grid, while the upper surface has a double boundary layer grid and an additional region of quadrilateral cells. (b) Close-up of the trailing edge, with quadrilateral cells in the boundary layer and the wake area, and triangular cells in the far field.

Figure 5.1: The NACA-0015 grid

In contrast to the results described in [16], no steady solution was found with the Fluent simulation. The solution does not converge monotonically, but starts oscillating. These oscillations are caused by unsteady flow phenomena that cannot be captured in a steady simulation. The results presented here are in fact instantaneous results, these results will change slightly in time.

The first result that will be analyzed is the velocity field. Figure 5.2 shows the flow field that was found for the NACA-0015 airfoil at 20° angle of attack. It can be seen that separation occurs on the rear part of the airfoil, resulting in a large bubble with low velocities. However, since the plot shows only the magnitude of the velocity vectors the exact separation location is not visible here.

From the examination of the boundary layer velocity profiles and the skin friction coefficient (see figure 5.3) more information about the separation location can be obtained. It was found that flow separation occurs in the region around x/c=0.65. This is a large difference with the results of [16], which show flow separation already at x/c=0.25. Consequently, also the lift coefficients do not have the same value. In the current simulation a lift coefficient of about 1.36 is found, while the reference value is only 0.90. In [16] also experimental results are used to validate the simulation. These experimental results show an even larger lift coefficient of about 1.55 at $\alpha=20^\circ$. The differences in turbulence modeling will certainly be one of the major causes of the different results. This holds for both the differences between the two numerical simulations, and the differences between the current numerical simulation and the experimental results.

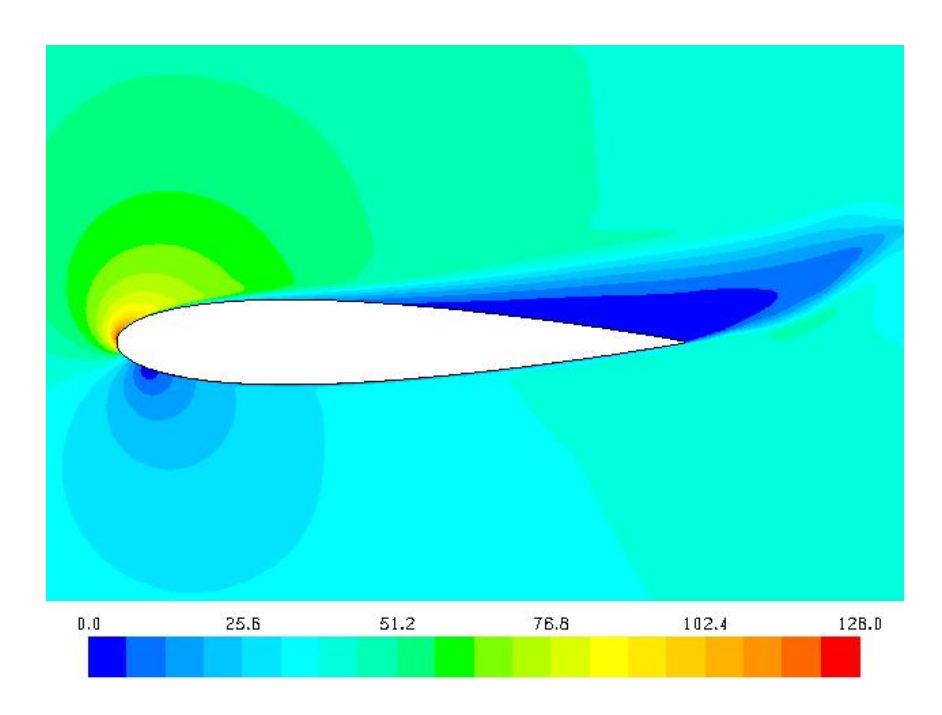


Figure 5.2: Contour plot of velocity (magnitude) in m/s, representing the flow field around the NACA-0015 airfoil at $\alpha=20^{\circ}$, M=0.12, $Re=0.9\cdot 10^6$.

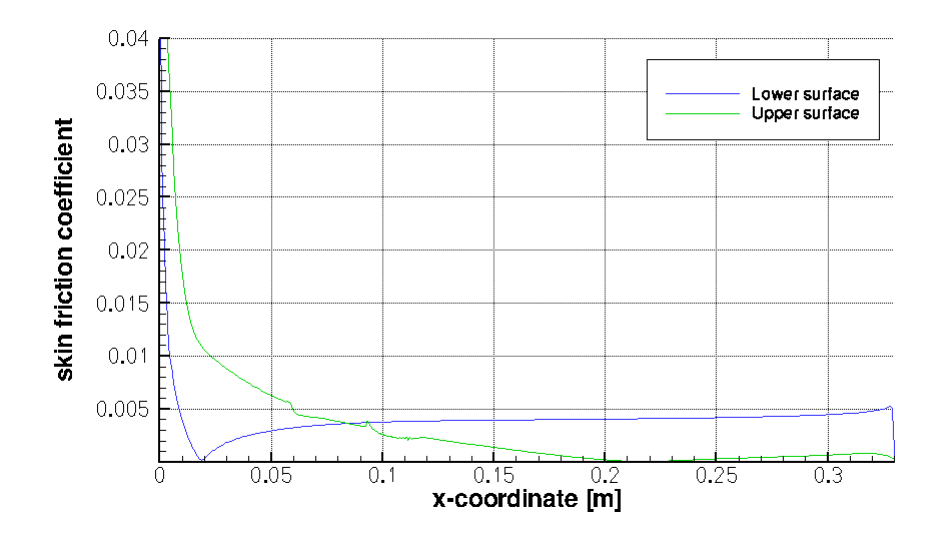


Figure 5.3: Skin friction distribution over the airfoil at 20° , showing separation at $x/c \approx 0.65$ ($M=0.12,\ Re=0.9\cdot 10^6$).

As was mentioned in the first part of this section, it was tried to perform the current Fluent simulations with almost the same conditions as used in the reference simulations. However, already in this stationary case the differences in the results turned out to be quite large. With the low Reynolds number as used in [16], the boundary layer just ahead

of the separation location will become very thick. With the performed Fluent simulation a boundary layer thickness of about 7.5% chord length was found at x/c = 0.60. As will become clear later on, this boundary layer thickness will require a fliperon with a length of 15% chord length. The implementation of such a large fliperon in the numerical simulations will be very difficult. Furthermore it should be remembered that the final application of the fliperon on the NLR7301 airfoil-flap configuration will take place at much higher Reynolds numbers. Those Reynolds numbers will be in the order of $4 \cdot 10^6$.

Therefore it is decided to leave the low Reynolds number regime in which the reference work was performed, and scale the grid back to its original shape. This means that the airfoil length is now 1.0 m, resulting in a Reynolds number of $2.7 \cdot 10^6$. The Mach number of 0.12 and all other conditions remain unchanged.

The new flow field is shown in figure 5.4. It can be seen that the separation bubble is smaller now, and that separation starts more aft on the airfoil. From the examination of the skin friction distribution it turned out that the flow separation now starts around x/c = 0.75. Consequently the lift coefficient increased slightly to a value of about 1.45. However, the most important change is the change in boundary layer thickness. The boundary layer thickness around x/c = 0.60 is reduced to about 4.5% of the chord length. This thickness is in the range in which a fliperon can be used for flow separation control. Finally figure 5.5 shows the vorticity contours. Due to the flow separation a large vortex occurs at the trailing edge of the airfoil. Further a lot of small vortical structures exist in the wake, and also some vorticity is found near the leading edge.

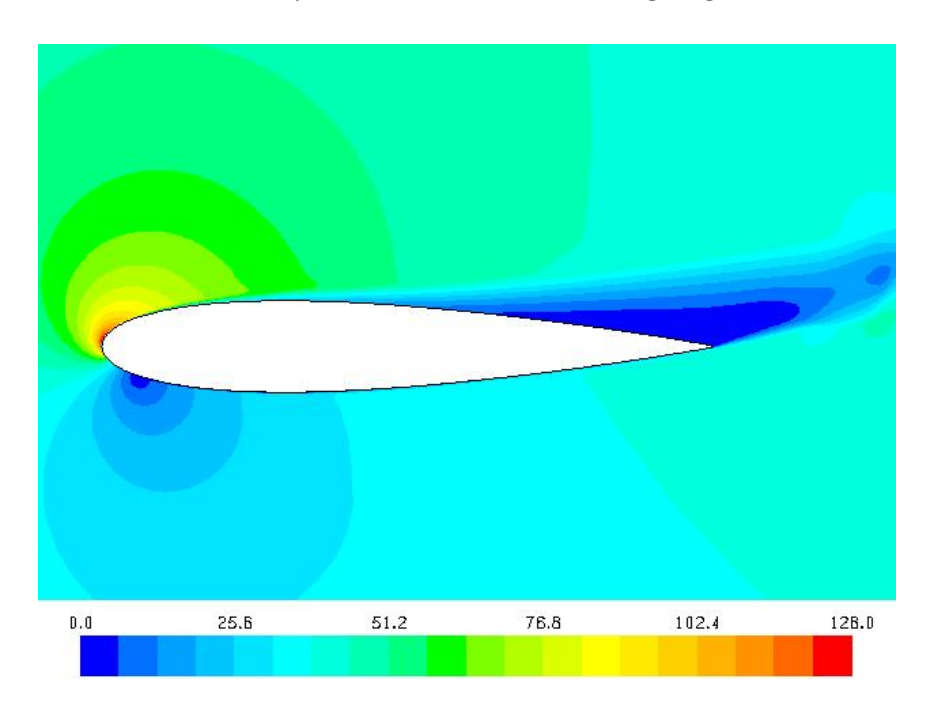


Figure 5.4: Contour plot of velocity (magnitude) in m/s, now at $\alpha=20^{\circ}$, M=0.12, $Re=2.7\cdot 10^6$.

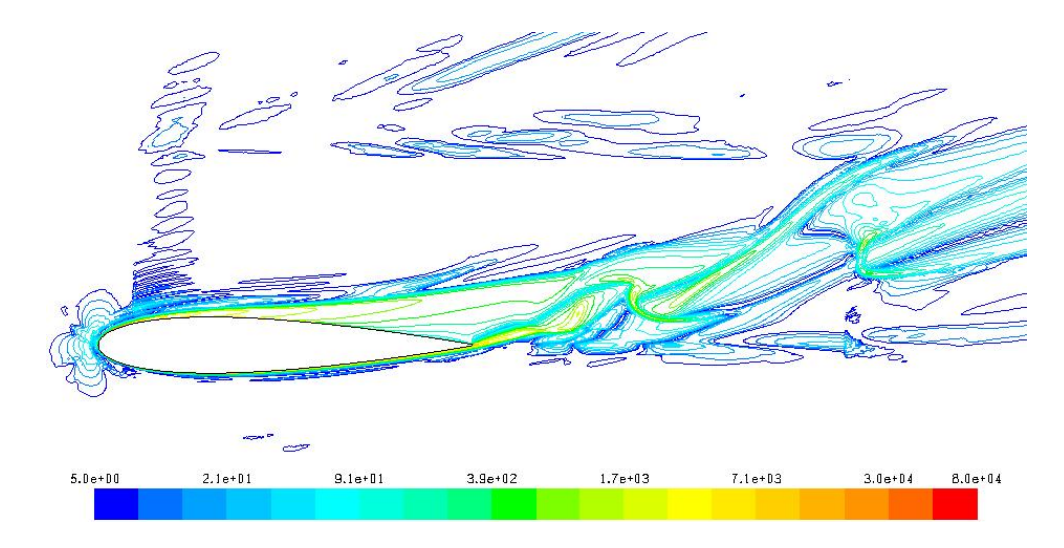


Figure 5.5: Contour plot of vorticity (magnitude) in s^{-1} , showing a large vortex at the trailing edge caused by flow separation ($\alpha = 20^{\circ}$, M = 0.12, $Re = 2.7 \cdot 10^{6}$).

Due to the large differences in the flow field of the (quasi) steady simulation and the change in Reynolds number, the results of the unsteady simulations in which flow control is applied will have to be judged with care. In [16] an enormous increase in lift coefficient (from 0.90 to about 1.60) is found due to the application of a synthetic jet at x/c = 0.30. However, in the current simulations it will not make sense to apply flow control at x/c = 0.30, since that will only destroy the attached flow at that point. It is decided to apply the fliperon at x/c = 0.52, so quite some distance to the separation point is maintained. It is not realistic to expect again an increase in lift coefficient of 80%; instead the aim is here to obtain at least the same maximum average lift coefficient of 1.60.

5.2 Application and results of flow control

In this section is explained how flow control by means of a fliperon is applied on the NACA-0015 airfoil. First the geometrical properties of the fliperon will be discussed. After that several different fliperon motions are introduced in order to investigate the influence of the frequency and the amplitude ratio. The results of the numerical simulations will be presented and the changed flow fields will be analyzed in detail.

5.2.1 Implementation of the fliperon

As was already explained in the previous section, the fliperon is placed some distance ahead of the separation location. The mentioned location of x/c = 0.52 is the most forward point of the fliperon and is also the point around which the fliperon will rotate.

The fliperon will have the same curvature as the NACA-0015 airfoil at that location. Opposed to the springboard type fliperon that was used in the test case with the ramp, a

cavity type fliperon is used in this case. This means that at the fliperon location a small part of the airfoil will be removed. Figure 5.6 shows the aft part of the NACA-0015 with the fliperon and the cavity below the fliperon. The fliperon is shown in its lowest position, so it rotates upward and never moves into the cavity. The cavity is never completely closed: when the fliperon is not deflected (deflection angle θ is zero) there remains a connecting gap between the cavity and the flow around the airfoil.

The required length of the fliperon depends on the local boundary layer thickness. The design criterion that was used here is the following: the length of the fliperon should be such that the amplitude of the fliperon tip equals the boundary layer thickness when the fliperon is deflected over 30°. This value for the deflection angle was derived from geometrical limitations for the dynamic mesh model, as was explained in section 3.3. In this case, with a boundary layer thickness of 0.045c, the fliperon length became 0.091c. About 5% of this length is taken as the minimum width of the connecting gap between the cavity and the flow around the airfoil. The other dimensions of the cavity were not studied explicitly in this test case.

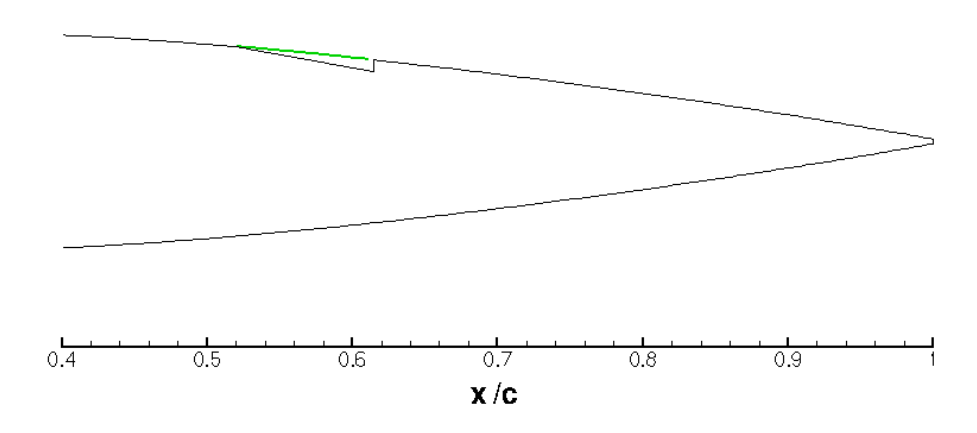


Figure 5.6: Aft part of the NACA-0015 airfoil. The rotating fliperon is drawn in green and is now in its lowest position ($\theta = 0^{\circ}$).

5.2.2 Fliperon frequency and amplitude

In this test case 4 unsteady simulations are performed. All simulations have a different user defined function that prescribes the motion of the fliperon. This results in different fliperon frequencies and different maximum amplitudes. All simulations start from the same point: the quasi steady solution of the flow over the airfoil at $\alpha = 20^{\circ}$ in which the fliperon is build in but not deflected. The steady lift coefficient at this starting point has a value of 1.39. (This is slightly lower than the lift coefficient on the clean airfoil that was mentioned before.)

The unsteady simulations are labelled A till D and their properties are listed in table 5.1. It should be remarked here that the properties F^+ and A_{max}/δ can be determined a priori from the angular velocity prescribed by the user defined function. The property C_{μ} can only be determined a posteriori, since the changed velocity field around the airfoil is used in this computation (see section 2.3.2).

V	view of the parameters describing the different						
		F^+	A_{max}/δ	C_{μ}			
	Simulation A	1.0	1.0	0.0089			
	Simulation B	0.8	1.0	0.0039			
	Simulation C	1.2	1.0	0.0163			
	Simulation D	1.0	1.1	0.0101			

Table 5.1: Overview of the parameters describing the different fliperon motions.

From table 5.1 it becomes clear that the simulations A till C can be used to investigate the effect of the fliperon frequency. In figure 5.7 the development of the lift coefficient of these simulations is plotted. The time span shown in this figure corresponds with about 7 fliperon oscillations for simulation A, 5 fliperon oscillations for simulation B and about 8 fliperon oscillations for simulation C. It can be seen immediately that the influence of the frequency on the lift coefficient is significant and that the highest frequency results in the largest increase in lift coefficient. In the worst performing case, simulation B, it becomes difficult to find back the periodicity of the fliperon motion. The physical backgrounds of these phenomena will be discussed in more detail in section 5.2.3.

In figure 5.8 the development of the lift coefficient in simulations A and D is plotted. In these simulations the frequency of the fliperon is the same, but the maximum fliperon amplitude differs. As can be seen from the figure, the enlarged amplitude results in larger fluctuations of the lift coefficient. However, the mean lift coefficient does not seem to be influenced that much by the slightly larger amplitude. It is a possibility that the maximum fliperon amplitude does influence the lift coefficient, but that some sort of saturation effect has occurred here. This could be tested by decreasing the maximum amplitude to for example 0.7δ and see what happens. Due to the large amount of time that is needed for a simulation, this simulation is not performed in this test case.

5.2.3 Unsteady simulations

Now the different simulations are studied individually and in more detail. Simulation A looked promising in figure 5.7 and therefore the simulation was continued till 12 fliperon oscillations were performed. The lift coefficient increased further and kept oscillating between the values of 1.57 and 1.67, with an average value of about 1.62. This means an average increase in lift coefficient of 0.23 or almost 17%.

In figure 5.9 the velocity vectors during the twelfth fliperon oscillation are shown. During the upward motion of the fliperon (figures 5.9(a) till 5.9(d)), a vortex is generated at the lower side of the fliperon. This vortex leaves the fliperon at the beginning of the downward

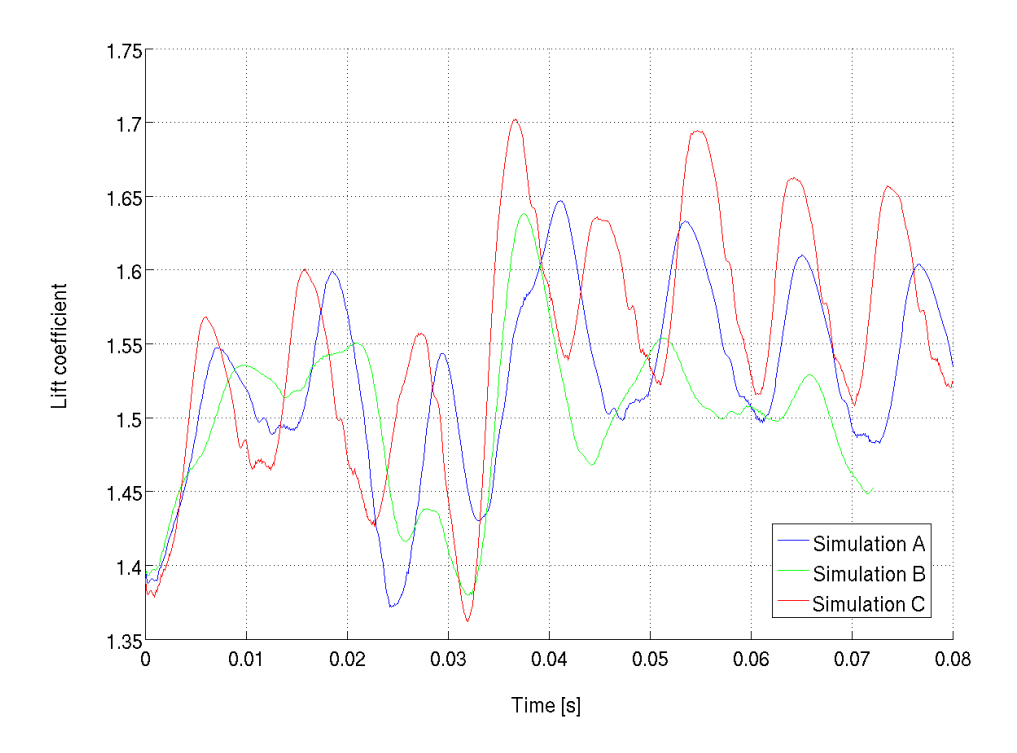


Figure 5.7: Development of the airfoil lift coefficient in time at different fliperon frequencies.

motion (figure 5.9(d)) and then rolls over the surface of the airfoil (figures 5.9(e) till 5.9(g)). The vortices generated by the fliperon interact with the vortices that originate from the flow that is separated near the trailing edge. Figure 5.11(a) shows a contour plot of the magnitude of the vorticity at the end of the twelfth fliperon oscillation ($t = 0.1383 \, s$). The vortices from the fliperon stay attached to the airfoil surface and then mix with the existing vortices. The interaction of vortices results in an increase of the total circulation around the airfoil and that causes an increase in lift coefficient.

From figure 5.7 it was already seen that simulation B was not that successful. The lift coefficient shows a slight increase to a value of about 1.50, but the periodicity of the fliperon motion is not seen in the lift coefficient. The momentum coefficient is another indicator that shows the limited efficiency of the flow control in this simulation. With a value of only 0.0039 it is clear that a relatively little amount of momentum is added to the flow. Looking at an instantaneous plot of the velocity field as shown in figure 5.10, it can be seen that the diameter of the vortices is larger than the diameter of the vortices seen in simulation A. As a consequence of that the vortices seem to be less powerful and are to a lesser extent capable of interacting with the separated flow at the trailing edge.

This is also illustrated by the vorticity plot in figure 5.11(b). It can be seen that the diameter of the vortices is larger while the maximum vorticity is about equal to the maximum vorticity of simulation A. This leads to a lower vorticity gradient, indicating weaker vortices that already start dissipating. The vortices are now less capable of interacting

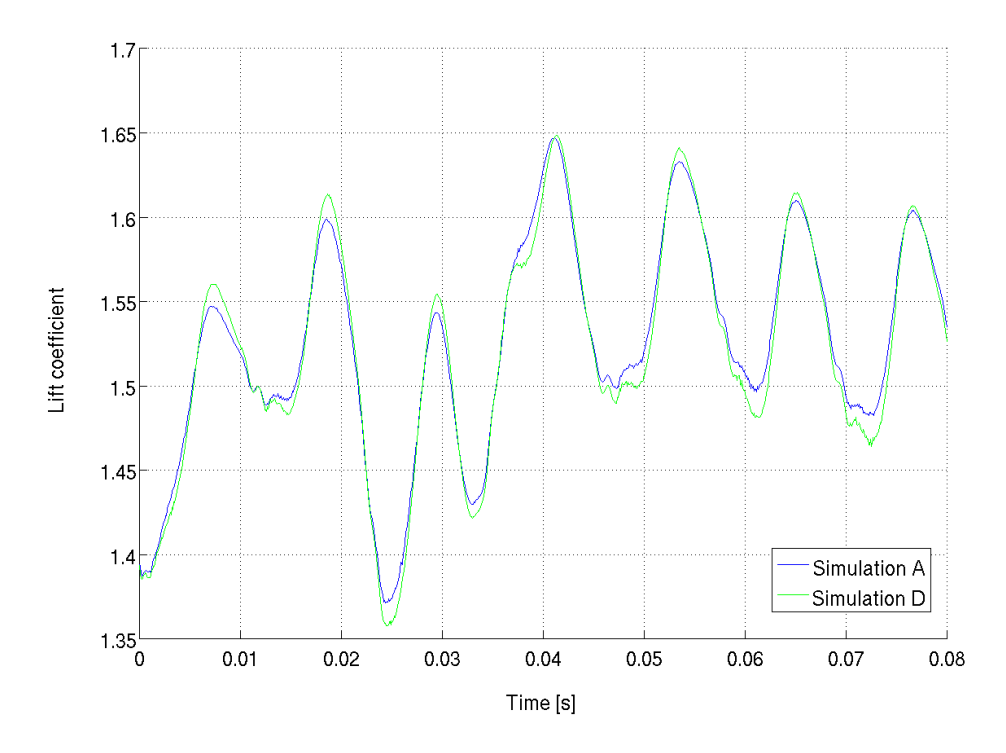


Figure 5.8: Influence of maximum fliperon amplitude on the development of the lift coefficient.

with the vortices from the separated flow at the trailing edge. In figure 5.11(b) it can be seen that the vortices do not exactly fit together, as was the case in simulation A. So this simulation has shown that decreasing the frequency of the fliperon is not very helpful in this situation.

Simulation C was the most successful simulation performed in this case. This simulation was also continued after $t=0.08\,s$ till finally 17 fliperon oscillations were performed $(t=0.163\,s)$. The development of the lift coefficient during these 17 oscillations is shown in figure 5.12. The average lift coefficient rises to a value of about 1.67, an increase of 20% with respect to the situation in which no flow control was applied. It would be an interesting case to find out what happens at larger frequencies and to investigate if even higher lift coefficients can be reached. Unfortunately, such an optimization would take too much time and is therefore not performed in this test case. However, such an optimization will be performed on the final application on the NLR7301 airfoil-flap configuration.

Until now the only aerodynamic coefficient that was studied is the lift coefficient. This is also the most important coefficient in this test case, but it does not mean that the other coefficients deserve no attention. Therefore the development of the total drag coefficient and the moment coefficient are plotted in figure 5.13. It can be seen that the drag coefficient oscillates with large amplitudes, but the mean drag coefficient does not really change in time. This can be explained by considering the different components of the drag coefficient.

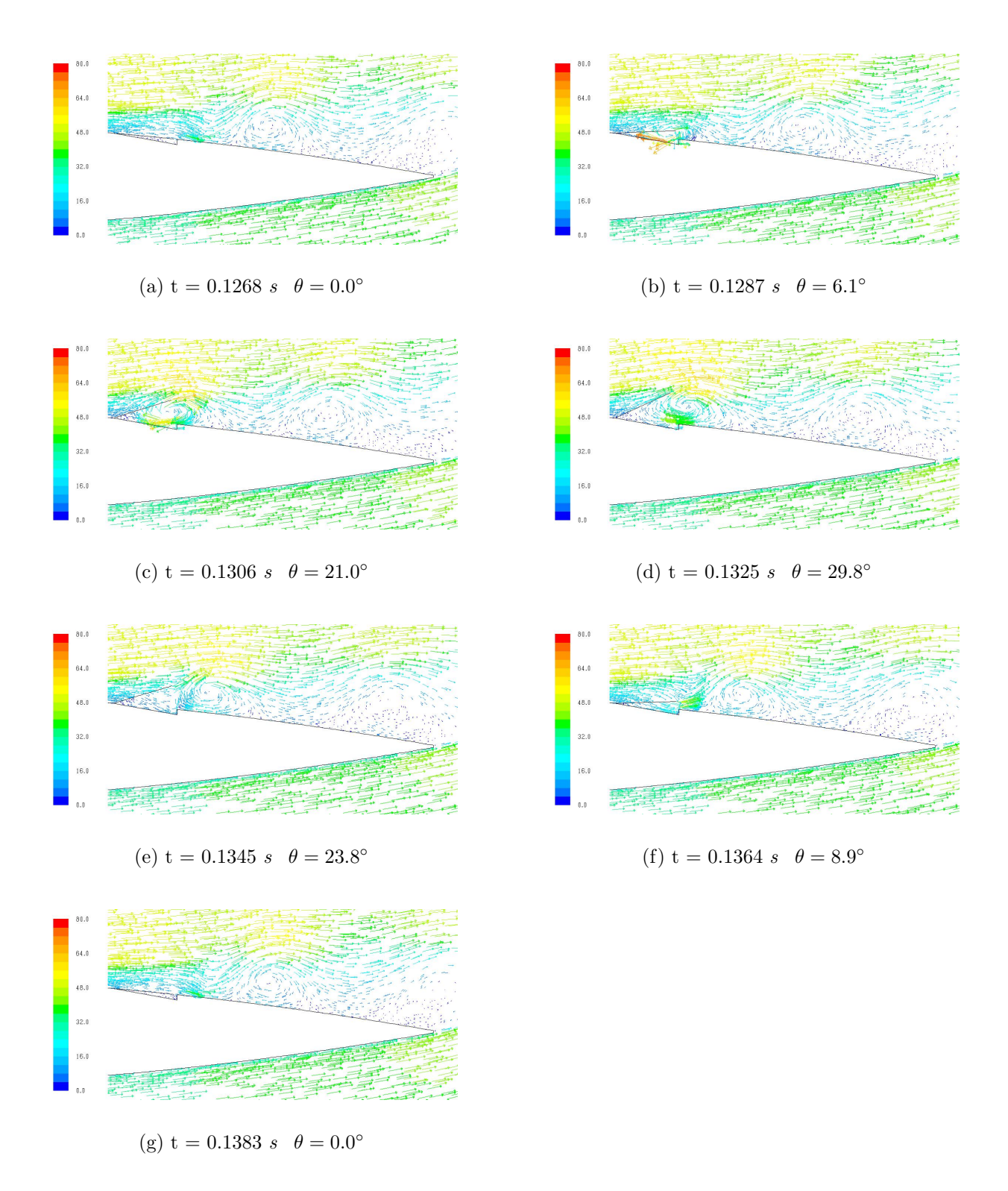


Figure 5.9: Development of the velocity field during one fliperon oscillation in simulation A (velocities in m/s).

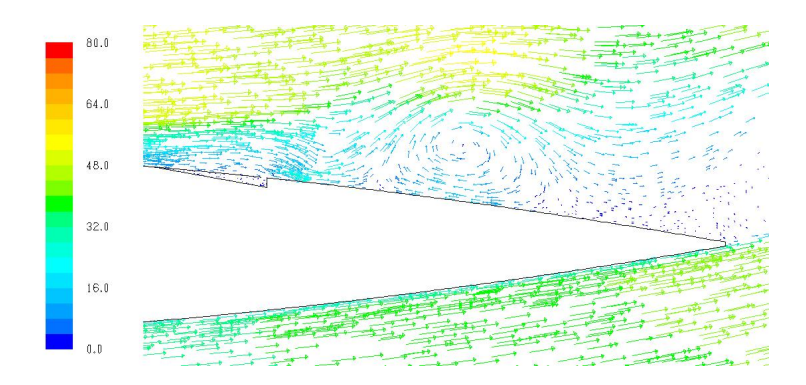


Figure 5.10: Instantaneous velocity field at the end of the fifth fliperon oscillation of simulation B. The larger vortices are less capable of interacting with the separated flow.

With an increasing amount of attached flow, the viscous drag coefficient will increase, but at the same time the coefficient for the pressure drag will decrease. These effects seem to cancel out each other in this case. The average moment coefficient increases during the simulation, primarily caused by the increase in lift coefficient. In case of a real aircraft during landing the increasing moment coefficient would result in lower loads on the horizontal tail surface.

An important question to ask at this simulation is why the flow control is so effective in this case. From the momentum coefficient, which has a value of 0.0163 over the last fliperon oscillation, it is clear that a large amount of momentum is added to the flow. It is remarked here that the time averaged momentum coefficient does not have the same value over each fliperon oscillation. The momentum coefficient over the 7th oscillation was for example higher than the momentum coefficient over the 17th oscillation; the value of the 7th C_{μ} was 0.0197. This indicates that not every fliperon oscillation results in exactly the same flow field. Further it shows that after 7 oscillations the flow field is not completely developed. As is also seen from figure 5.12, the lift coefficient has not arrived in its final periodic behaviour after 7 oscillations.

Figure 5.14 shows the instantaneous velocity field at the end of the 17th fliperon oscillation. It is clearly visible that the vortices have a smaller diameter in this case. So in agreement with the observations in the previous test case, it is seen here as well that increasing the frequency leads to vortices with a smaller diameter. In this case the smaller diameter turns out to be advantageous; the vortices stick to the airfoil surface and follow it closely. In this way much interaction between the vortices and the separated flow can take place. The same conclusions can be drawn from the vorticity contours in figure 5.11(c). The interaction is clearly visible and the vortices fit together like pieces of a puzzle. This prevents the vortices that originate from the separated flow from growing and their diameter remains rather small. In this way also the height of the wake in which the vortices occur remains small. Probably there is an optimum diameter for the vortices generated by the fliperon at which the interaction is maximized. At that frequency a maximum in lift coefficient increase will be found. Optimizing the fliperon motion till this point is, due to time constraints,

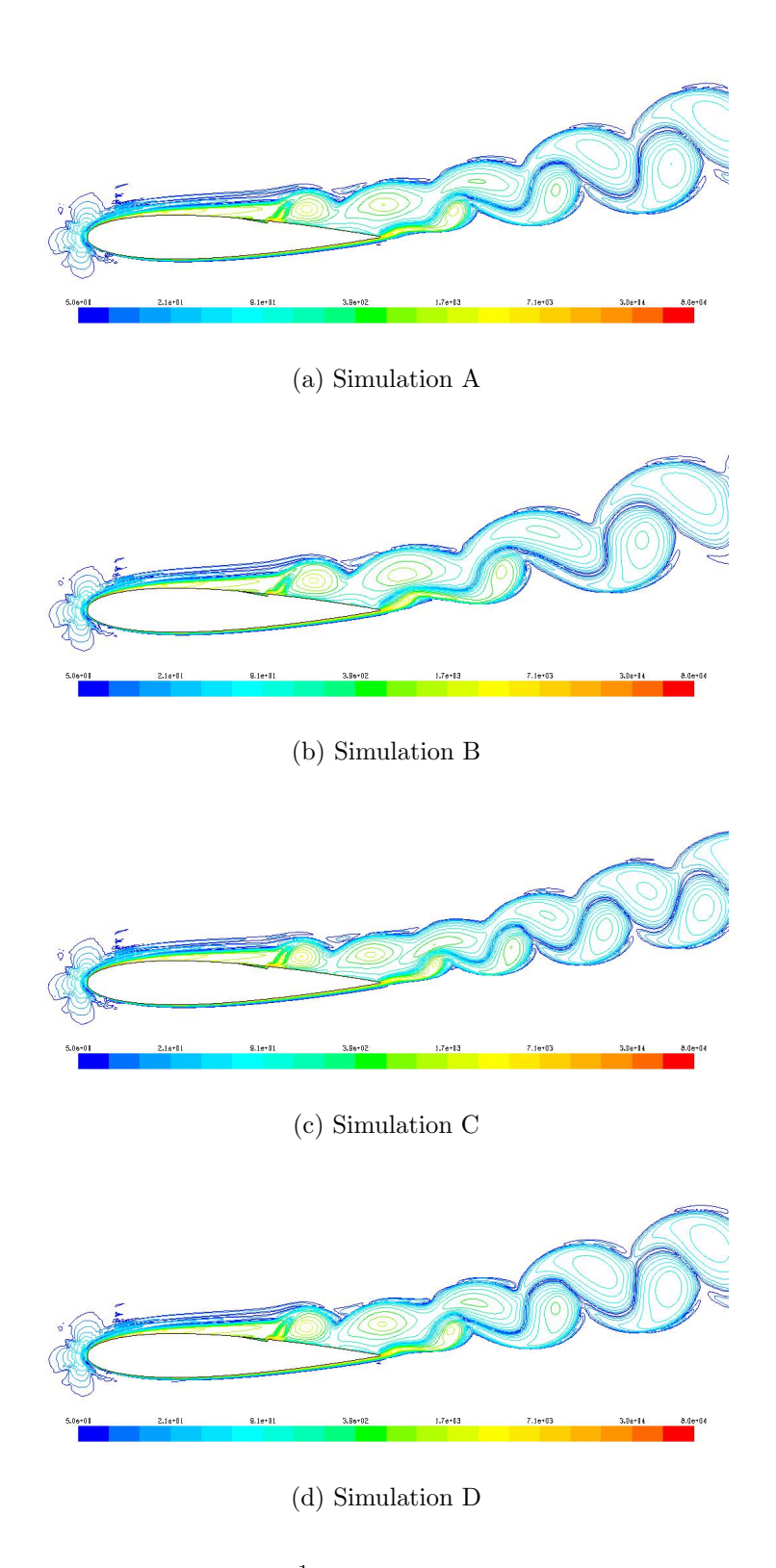


Figure 5.11: Vorticity contours (in s^{-1}) at the end of the last simulated fliperon oscillation. See also figure 5.5 for the vorticity field of the clean airfoil.

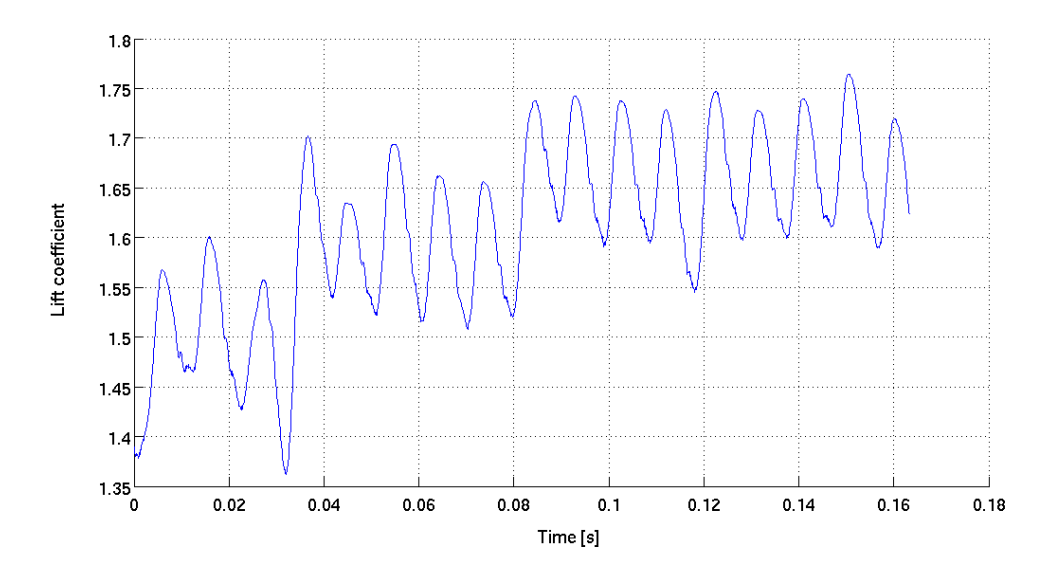


Figure 5.12: Development of the lift coefficient in simulation C.

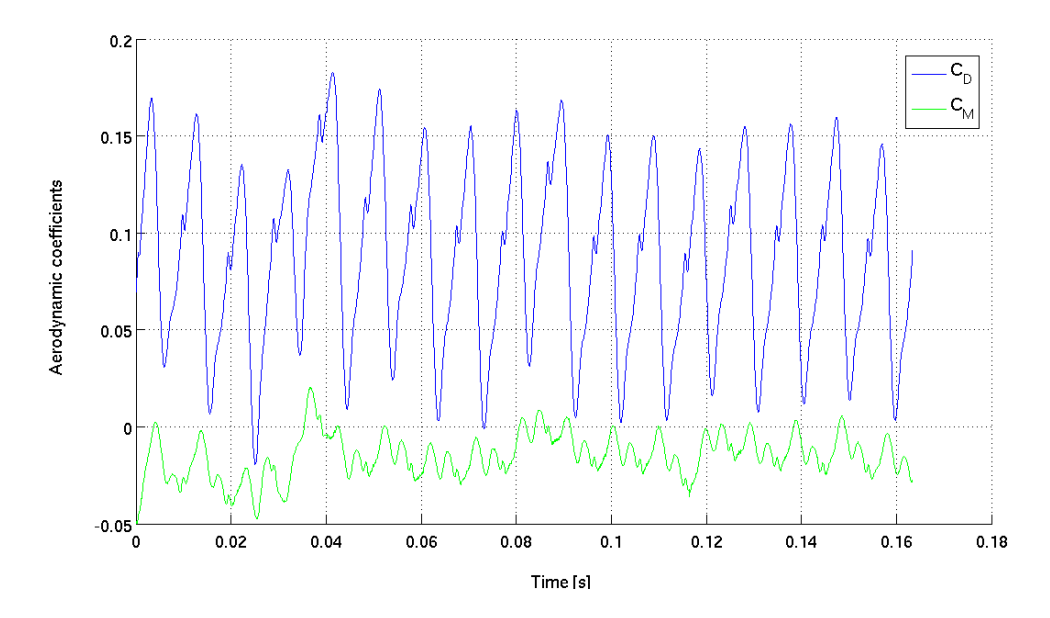


Figure 5.13: Development of the drag and aerodynamic moment coefficient in simulation C.

postponed to the final application on the airfoil-flap configuration.

The last simulation was simulation D in which the fliperon amplitude was enlarged. As was already seen in figure 5.8, this does not seem to make much sense. The average lift coefficient develops more or less in the same way as the the lift coefficient of simulation A. Although the momentum coefficient is a little larger in this case (0.0101 versus 0.0089 in simulation A), it is not really clear what happened with the additional momentum. As was already mentioned at the begin of this section, it looks like some sort of saturation effect

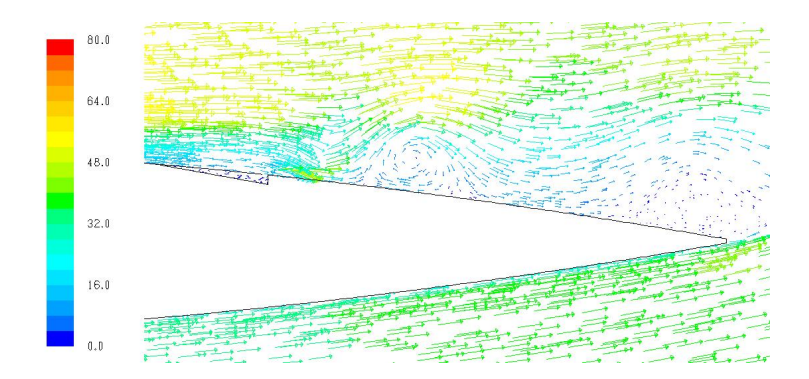


Figure 5.14: The increased fliperon frequency of simulation C results in vortices with a smaller diameter that seem to be perfectly capable of following the airfoil surface.

occurs which means here that adding momentum to the flow outside the boundary layer does not increase the energy of the separated flow because it does not help in producing better interacting vortices. According to this theory, the momentum coefficient and the lift increase should be lower when the maximum fliperon amplitude is smaller. Earlier unsuccessful simulations do indeed point in this direction. However, in order to draw strong conclusions, more cases with lower maximum amplitudes should be investigated. The velocity field at the end of the seventh fliperon oscillation is shown in figure 5.15. The flow field looks almost the same as the flow field in simulation A at the end of a fliperon oscillation, see figure 5.9(g). However, it can be seen that the shape of the vortices is slightly different. The vortices of simulation D are more circular, they are less flattened by the mean flow. Analysis of the vorticity contours in figure 5.11(d) strengthens this observation. But this figure also shows that the interaction between the vortices is not significantly changed; they fit together in the same way as was seen in simulation A. This explains why the average lift coefficient is not larger than the average lift coefficient of simulation A.

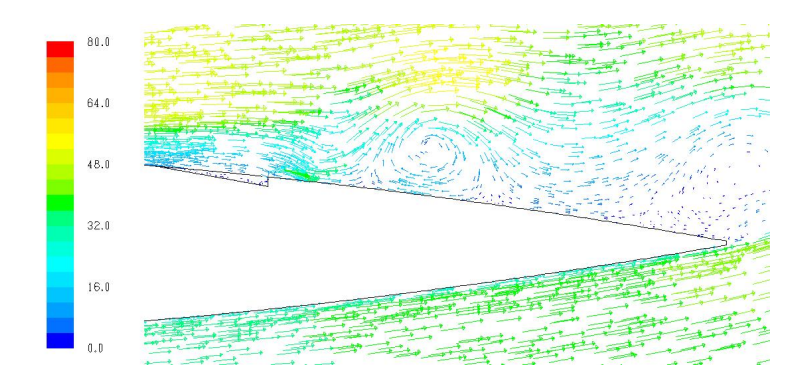


Figure 5.15: Instantaneous velocity field at the end of the seventh fliperon oscillation in simulation D. The larger maximum amplitude results in slightly more circular vortices.

5.3 Conclusion of the test case

This second test case, in which active flow control was applied on the NACA-0015 airfoil, has been very successful in two ways. First of all, a lot of insight was obtained in both the way the fliperon should be implemented and in the way the fliperon realizes its performance. The influence of the determining parameters F^+ , A_{max}/δ and C_{μ} on the flow field and on each other has become more clear. Secondly, this test case was successful because it demonstrated the capability of a fliperon to control separated flow and to increase the lift coefficient at the fixed, post-stall angle of attack significantly.

In the first part of this chapter the work of Munts was discussed [16]. Because the numerical tools used in this reference work are so different from the numerical tools used here, large differences occurred already in the steady simulation. Therefore it was decided not to compare every detail of the flow field. Instead the more general effects of flow control became the most important point of comparison.

After the application of a synthetic jet, a time-averaged lift coefficient of 1.6 is found in [16] for the NACA-0015 at 20° angle of attack. Further the drag coefficient is reduced to about 0.1 and the moment coefficient can be controlled by the momentum input, the jet angle and the jet frequency. The maximum momentum coefficient used for the flow control was 0.02 in this case.

The most successful application of the fliperon, found in simulation C, turns out to be even more effective than the synthetic jet. With a momentum coefficient of only 0.0163, the time average lift coefficient increases to a value of 1.67. The drag coefficient remains more or less unchanged and keeps its value of 0.08. So with a smaller momentum input, a larger increase in lift coefficient is reached. Furthermore the fliperon is less complex than the synthetic jet, making it cheaper and more reliable. This shows that the fliperon is both an effective and an efficient way of flow control in this case.

The demonstration of the fliperon performance was not the only goal of this test case. Investigation of the influence of the parameters F^+ and A_{max}/δ was also an important issue. It has become clear that the dimensionless frequency is the most important parameter. It determines also the diameter of the vortices generated by the fliperon. When the frequency is optimized, the interaction with the vortices that occur from the separated flow at the trailing edge is maximal. This will result in a maximal increase in lift coefficient. The maximum fliperon amplitude seems to be less important. It turned out that the maximum amplitude should be in the order of the boundary layer thickness and that larger amplitudes do not necessarily result in larger lift increments.

Flow control on the NLR7301 airfoil-flap configuration

In this chapter the application of an oscillating fliperon on the flap of an airfoil-flap configuration will be demonstrated. The best situation to do this is with a flow that is partly separated from the flap but is still attached to the main element. Since the flow around the flap is significantly influenced by the presence of the main element, this flow field will be more complicated than the flow field of a single element airfoil like the NACA-0015 airfoil. This chapter will present a lot of numerical results for the NLR7301 airfoil-flap configuration. First of all, the results of several validation simulations are discussed in section 6.1. In section 6.2 is explained how the configuration is adapted in order to obtain a flow field that is well suited for the demonstration of flow control. Then three different types of fliperons will be applied on the flap as flow control devices. The results that were obtained from these simulations are discussed in section 6.3. Finally the fliperon is compared to other types of flow separation control in section 6.4.

6.1 Turbulence model validation

As was already mentioned in section 3.2.2, three different turbulence models are examined for closing the numerical system of equations. In order to find out which turbulence model is best applicable to the flow around an airfoil-flap configuration, the numerical results obtained with the different turbulence models will be compared to experimental results. This comparison will also give an indication of the quality of the numerical simulation in general.

The National Aerospace Laboratory (NLR) has conducted wind tunnel tests on the NLR7301 airfoil with flap [1], which is shown in figure 6.1. The coordinates of this airfoil can be found in appendix C. One of the goals of these tests was to provide sufficient data to allow limited validation of CFD codes. These experimental results turned out to be also very useful for the validation of the turbulence models.

In this section the simulation results are presented for the Spalart-Allmaras turbulence model, the realizable $k-\epsilon$ model and for the shear-stress transport $k-\omega$ model. The NLR7301 airfoil-flap configuration is used with the flap deflected over 20° . Simulations are performed at angles of attack of 0.0° , 6.0° and 10.1° and they are compared to the experimental results. The experimental results consist for all of these situations of the lift coefficient and the aerodynamic moment coefficient. Further the drag coefficient and the pressure distribution were measured for $\alpha=6.0^{\circ}$ and $\alpha=10.1^{\circ}$. At $\alpha=6.0^{\circ}$ also several boundary layer velocity profiles were measured. In both the experiments and in the numerical simulations the Mach number was 0.185. The Reynolds number was slightly different due to the use of a unit chord length in the numerical simulations. The experimental Reynolds number was $2.5 \cdot 10^{6}$, while the Reynolds number of the simulations was $4.0 \cdot 10^{6}$. This small difference is not expected to have a significant influence on the results.

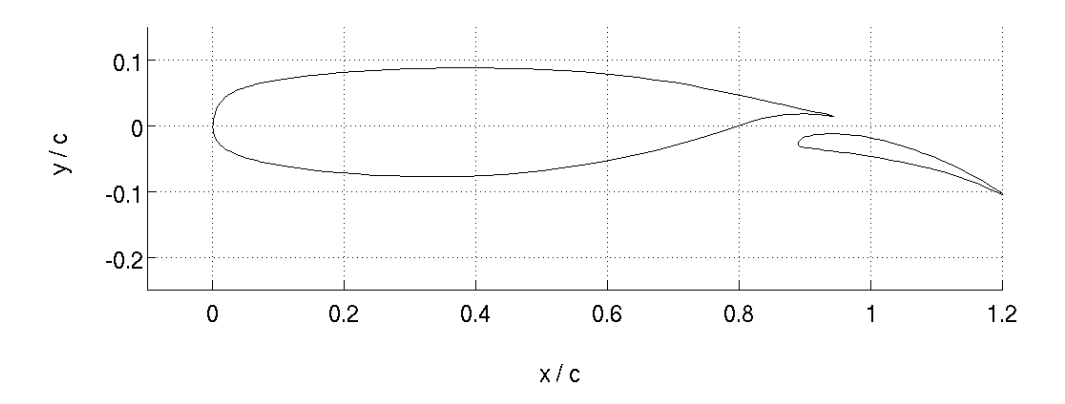


Figure 6.1: The NLR7301 airfoil with the flap deflected over 20° .

Results for 0.0° angle of attack

The pressure distributions over the airfoil-flap configuration that were obtained with the different turbulence models turned out to be almost equal at 0.0° angle of attack. Only in the simulation of the leading edge suction peak small differences were found. The Spalart-Allmaras model predicts the lowest pressure coefficient for this point (highest suction peak), but the difference with the realizable $k - \epsilon$ model is very small. The pressure coefficient predicted with the SST $k - \omega$ model is slightly higher.

The experimentally and numerically obtained aerodynamic force coefficients are summarized in table 6.1. It should be remarked here that the values in table 6.1 are the coefficients for the complete configuration. They consist of the forces on both the main element and the flap. The aerodynamic moment is defined with respect to the quarter-chord point (x/c = 0.25).

The predictions of the aerodynamic forces based on the different turbulence models do not differ much. Furthermore 6.1 shows that the differences between the simulations and the measurements are very small. The best lift coefficient prediction, which is obtained with the Spalart-Allmaras model, agrees very well with the experimentally obtained lift coefficient. It should be realized that the flow situation at zero angle of attack is a rather easy situation to simulate, but still these results indicate that the quality of the numerical simulation is good.

Table 6.1: Aerodynamic force coefficients at $\alpha=0.0^{\circ}$ for numerical simulation with different turbulence models compared to experimental values.

	C_L	C_D	C_M
Experimental	1.640	-	0.457
Spalart-Allmaras	1.640	0.0228	0.464
Realizable $k - \epsilon$	1.627	0.0235	0.460
Shear-stress transport $k - \omega$	1.617	0.0233	0.457

Results for 6.0° angle of attack

A large amount of measurement results is available for the situation in which $\alpha = 6.0^{\circ}$. First of all, the numerical results for the pressure distribution over the main element and the flap are compared to their experimental counterparts. Figure 6.2 shows these pressure distributions. It is clear that these simulations make sense: the differences between the numerical results and the experimental results are quite small. Just as for the case in which $\alpha = 0.0^{\circ}$, only small differences between the numerical simulations are observed. Again some differences can be seen at the leading edge suction peak. In this case the simulation based on the realizable $k - \epsilon$ model gives the best prediction of this peak. Further it can be seen that the pressure coefficients on the upper side of the main element and the flap are slightly underpredicted in each simulation.

Based on the pressure distributions, good agreement between experiment and simulations is expected with respect to the aerodynamic force coefficients. As can be seen in table 6.2, this agreement is certainly present. Although all numerical simulations underpredict the lift coefficient, the values are still very close to the experimental value. The observation that the lift coefficient is underpredicted corresponds with the underpredicted pressure coefficients on the upper surfaces of the main element and the flap. Just as in the situation with $\alpha=0.0^{\circ}$, the best prediction for the lift coefficient comes from the Spalart-Allmaras model. Further it can be seen that the numerically simulated drag coefficients are all larger than the experimentally measured drag coefficient. The simulation based on the Spalart-Allmaras model gives the best prediction, but the deviation of this drag coefficient prediction is, in a relative sense, much larger than the deviation of the lift coefficient prediction.

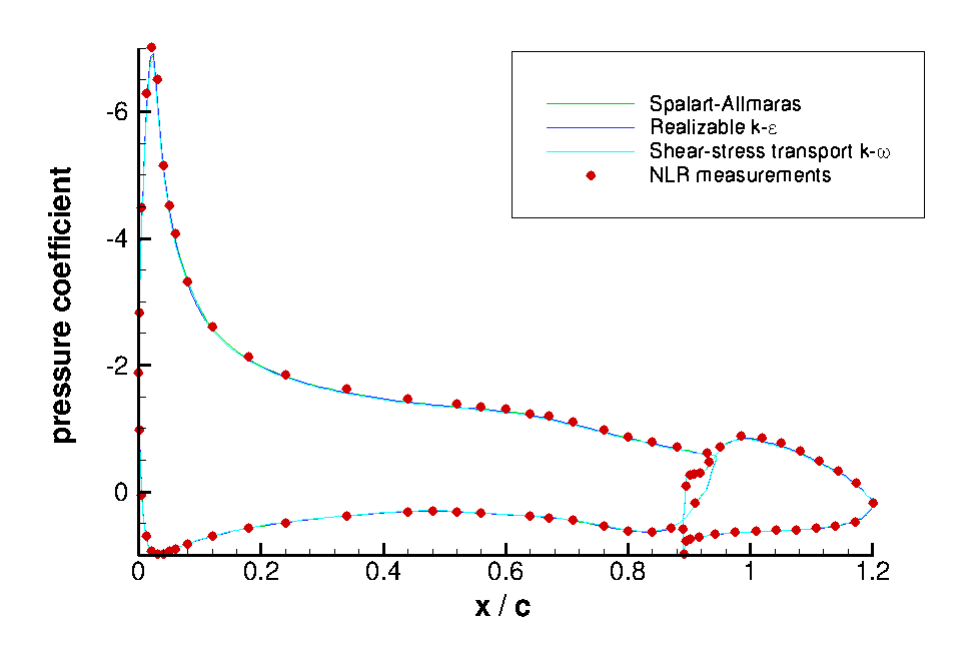


Figure 6.2: Comparison of experimentally and numerically obtained pressure distributions at $\alpha = 6.0^{\circ}$.

Table 6.2: Experimental and numerical aerodynamic force coefficients at $\alpha = 6.0^{\circ}$.

	C_L	C_D	C_M
Experimental	2.416	0.0402	0.471
Spalart-Allmaras	2.407	0.0410	0.480
Realizable $k - \epsilon$	2.398	0.0418	0.478
Shear-stress transport $k - \omega$	2.378	0.0421	0.473

In order to get a better idea of what happens close to the airfoil surface, the boundary layer velocity profiles are examined. These profiles were measured at several different locations on the main element and the flap. Here the choice was made to compare the numerical and experimental velocity profiles at 2 locations on the upper surface of the main element (x/c = 0.24 and x/c = 0.60) and on 1 location on the upper surface of the flap $(x_f/c = 0.12)$. Although the numerically simulated boundary layers were almost equal at these points, it was not possible to match these results with the measurements. Unfortunately, it was not clear which velocity components were measured in the experiment and how the distance to the airfoil surface was defined. Therefore further comparison was omitted.

Several other techniques were proposed in order to validate the numerical boundary layer results. First of all, the boundary layer grid was refined. This did not change the boundary layer velocity profiles significantly, which indicates that the grid size is correct and that the results are reliable.

Next to this two additional simulations were performed in which different wall functions were used within the $k-\epsilon$ turbulence model. In the first simulation enhanced wall treatment was used while in the second simulation non-equilibrium wall functions were applied. Again the differences were extremely small and did not compensate the additional computational effort.

Although these techniques do not form a watertight proof of the correctness of the simulated boundary layer velocity profiles, they give at least an indication of sufficient quality. Therefore the standard wall functions are remained as setting in the $k-\epsilon$ turbulence model for the coming simulations.

Reviewing the results for this situation in which $\alpha = 6.0^{\circ}$, it can be said that the main flow around the airfoil-flap configuration is simulated well. The pressure distribution, as well as the simulated values for the lift and aerodynamic moment coefficient, are in good agreement with the measured values. This can also be said for the simulated value of the drag coefficient, although its deviation from the measured value is larger.

Results for 10.1° angle of attack

From the NLR measurements follows that completely attached flow occurs in the situation in which the angle of attack is increased to 10.1°. This can be also been seen from figure 6.3, which shows both the experimentally measured and the numerically simulated pressure distributions. Obviously, this case is more difficult to simulate than cases at lower angle of attack because the pressure gradients are larger now. It is therefore not surprising that here the differences between the turbulence models become really visible. In figure 6.3 it can be seen that the realizable $k-\epsilon$ model gives the best simulation of the leading edge suction peak. Also on the upper surfaces of the main element and the flap the $k-\epsilon$ simulated pressure coefficients are closest to the measurements. The results of the Spallart-Allmaras model are not as good as the results of the $k-\epsilon$ model, but still reasonable. The results of the $k-\epsilon$ model are not that good, they show clear discrepancies with the measurements.

In table 6.3 the aerodynamic coefficients of the wind tunnel measurements and the numerical simulations are summarized. It can be seen that the coefficients resulting from the realizable $k-\epsilon$ model are closest to the experimentally obtained coefficients. The Spalart-Allmaras model follows as second best; the results of the SST $k-\omega$ model are much further away from the experimental results. As was already noticed earlier, the simulated results for the drag coefficient differ relatively more from the measurements than the lift and moment coefficient do. This is also seen in the current case and can possibly be explained by differences between the simulated and the real boundary layer flow that occur for example from different surface roughnesses.

Summarizing the three flow situations ($\alpha = 0.0^{\circ}$, 6.0° and 10.1°), it can be concluded that the simulations with the Spalart-Allmaras turbulence model and the realizable $k - \epsilon$ turbulence model were the best approximations of the wind tunnel experiment. However, it was observed that the realizable $k - \epsilon$ model gave the best results in the most difficult

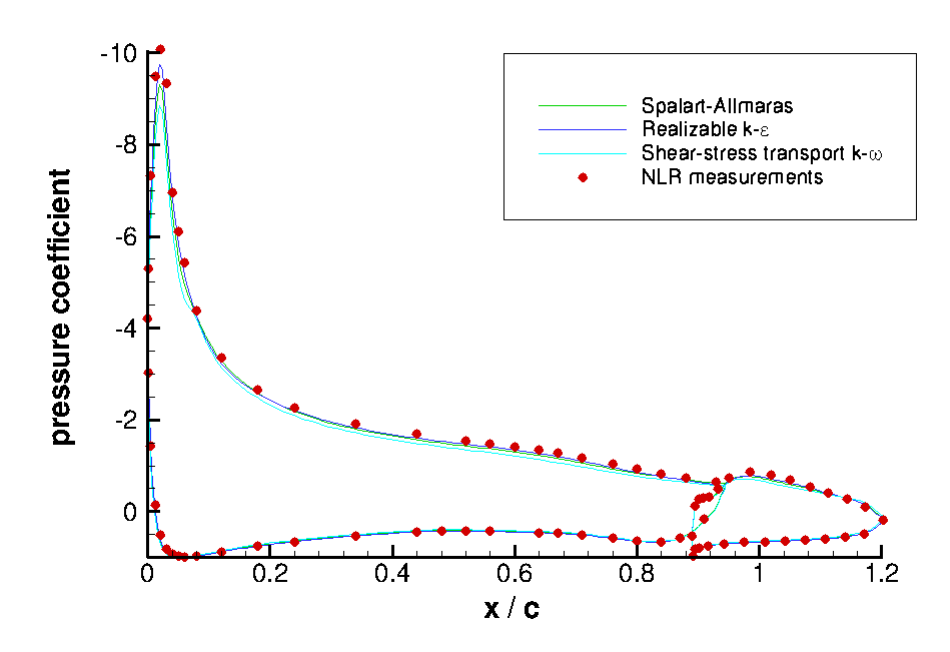


Figure 6.3: Comparison of experimentally and numerically obtained pressure distributions at $\alpha = 10.1^{\circ}$.

Table 6.3: Experimental and numerical aerodynamic force coefficients at $\alpha=10.1^{\circ}$.

	C_L	C_D	C_M
Experimental	2.877	0.0567	0.463
Spalart-Allmaras	2.766	0.0734	0.459
Realizable $k - \epsilon$	2.816	0.0644	0.465
Shear-stress transport $k - \omega$	2.638	0.0809	0.435

flow situation ($\alpha = 10.1^{\circ}$). Because the situations of the coming simulations will be even more difficult due to larger pressure gradients and flow separation, the realizable $k - \epsilon$ model is expected to give the best performance. So therefore the coming simulations will all be performed with this turbulence model.

Further the comparison of numerical and experimental results has shown that the general quality of the simulations is good. The simulated pressure distributions and lift coefficients do not differ much from their experimental counterparts. Only the drag coefficients do not match exactly. The small difference in Reynolds number may play a role here, but the largest differences will be caused by the modeling of the surface roughness, that is always an approximation of the real situation.

6.2 Adaption of the configuration

In order to obtain the required separated flow the flap was first, rather arbitrary, deflected over 60°. In this section will be discussed which problems occurred in the flow field of the deflected flap and how these problems are solved with a new flap design. Finally a steady simulation is performed to examine the new flow field and to obtain the parameters that are needed for the design of the flow control devices.

6.2.1 Current situation

In figure 6.4 the flow around the 60° deflected flap is shown. This figure reveals a couple of problems that occur in the current situation. First of all, the flap has a rather small nose radius which causes the flow to separate from the flap surface immediately at the nose. It is already known from previous experience ([10],[18] and section 5.2.1) that a fliperon is most efficient when it is placed some distance ahead of the separation location. However, in this situation the available space in which fliperon can be located is extremely small. Furthermore the vortices produced by the fliperon are only effective if they follow the flap surface, as was also seen in the previous test case. It will be hard to realize attaching vortices here, since the fliperon has to be placed that far upstream that it will not be able to push the vortices over the whole flap surface.

It is rather difficult, if not impossible, to solve these problems within the current flap geometry. Because the goal of this thesis work is to perform flow control by means of an oscillating fliperon and not to improve the NLR7301 airfoil specifically, it is decided that a completely new flap geometry will be designed. The main airfoil will remain its original shape and size. The requirements for the new flap are a larger nose radius such that enough space with attached flow is available to locate the fliperon. Furthermore the flap should be thick enough to store the fliperon actuators.

6.2.2 New flap design

The new flap will be designed as if it is a NACA 4-digit series airfoil. This approach is chosen because the 4-digit notation makes it possible to control the maximum camber and thickness of an airfoil easily. The meaning of the four digits can be explained as follows: the first digit indicates the maximum camber as a percentage of the chord length (symbol m). The second digit indicates the position of the maximum camber in tenths of the chord length (p). Finally, the last two digits indicate the maximum thickness as a percentage of the chord length (t). So for the NACA-2415 airfoil it is known that the maximum camber is 2%c and that this maximum is located at x/c = 0.40. The maximum thickness is 15%c. From [14] it is found that every NACA 4-digit airfoil has a mean camber line according to

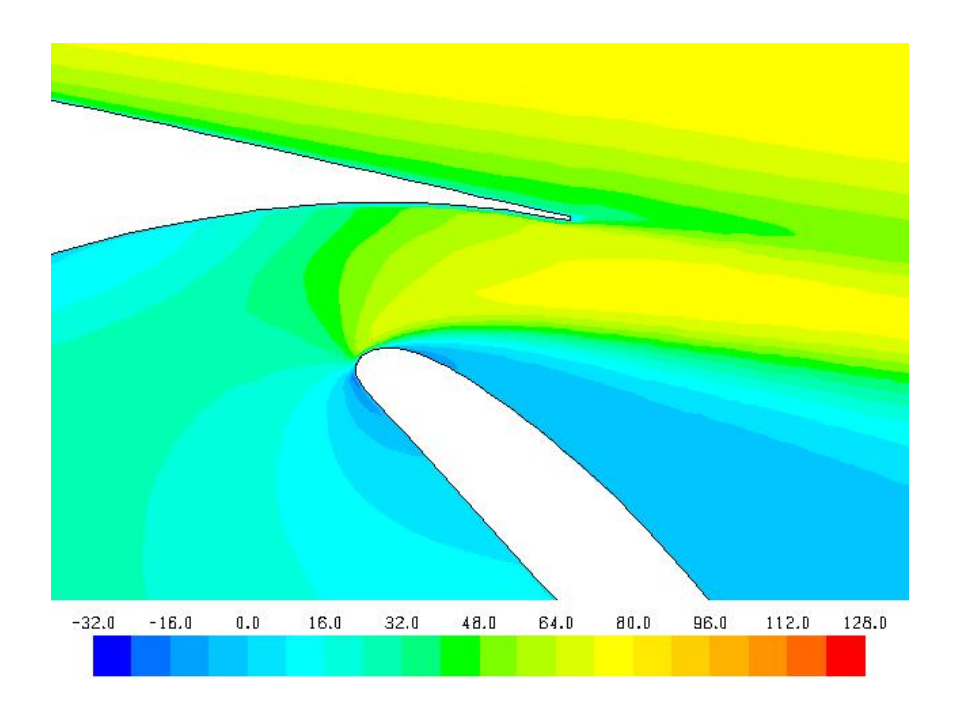


Figure 6.4: Contour plot of the x-velocity, indicating flow separation (negative x-velocities) immediately at the flap leading edge.

the following formula:

$$y_c = \frac{m}{p^2} \left(2px - x^2 \right)$$
 $0 <= x <= p$ (6.1)

$$y_c = \frac{m}{(1-p)^2} \left((1-2p) + 2px - x^2 \right) \qquad p <= x <= c$$
 (6.2)

The derivative of the mean camber line is represented by the symbol ϕ and defined as

$$\phi = \arctan\left(\frac{dy_c}{dx}\right) \tag{6.3}$$

For the whole range of x-values, the thickness with respect to the mean camber line follows from:

$$y_t = \frac{t}{0.2} \left(0.2969\sqrt{x} - 0.1260x - 0.3516x^2 + 0.2843x^3 - 0.1015x^4 \right)$$
 (6.4)

Now the coordinates of the upper surface (x_U, y_U) and the lower surface (x_L, y_L) can be calculated:

$$x_U = x - y_t \cdot \sin \phi \tag{6.5}$$

$$y_U = y_c + y_t \cdot \cos \phi \tag{6.6}$$

$$x_L = x + y_t \cdot \sin \phi \tag{6.7}$$

$$y_L = y_c - y_t \cos \phi \tag{6.8}$$

The new flap geometry was found by varying the values of m, p and t till a rather thick airfoil with a sufficiently blunt nose was obtained. The final values that were found are: m = 0.12, p = 0.30 and t = 0.25. So the flap has a maximum camber of 12%c located at 30%c and a maximum thickness of 25%c. Since m now consists of two digits, this profile does in fact not fit the four digit code. In this case this is not seen as a problem, since the airfoil-flap configuration is already a non-existing configuration.

Now the NACA profile has to be transformed to a flap that fits the NLR7301 configuration. First the complete flap is scaled by a factor of 0.32 in order to obtain the same chord length as the original NLR flap. Then the flap position and deflection angle have to be determined. This has to be done with care, since the consequences are large. The flap position influences the flow pattern around the trailing edge of the main element and the flow around the flap nose. The deflection angle determines the flap lift coefficient, but also the amount of flow separation. Because simulating different configurations with Fluent takes a lot of time, the 2D panel code MSES [9] will be used here to obtain the flap position and deflection angle.

With MSES it is possible to analyze and optimize multi-element airfoil configurations very quickly. In the first step the coordinates of the different elements are read and a grid is generated. In the second step the flow field is calculated. To do so, it is assumed that the viscous effects are only of significant influence in a small boundary layer and in the wake. Outside this domain the Euler equations are solved to obtain the inviscid flow field. A code based on boundary layer theory is used to solve the viscous part of the flow. Depending on the input of the user, the boundary layer is modelled with free or forced transition.

It is obvious that a flow solver like MSES is less accurate than a full Navier-Stokes solver like Fluent. Especially at angles of attack near and beyond stall, where a large part of the flow is separated, the accuracy of MSES is limited. Therefore the results obtained with MSES are used only as an indication of the flow field. The final configuration will then be analyzed with Fluent to obtain a more accurate solution of the flow field on which the design of the fliperon will be based.

So the goal of the performed MSES analysis was to obtain a flap position and deflection angle such that a limited amount of flow separation occurs. A manual approach was chosen here, which means that the flap position and angle are prescribed and that the corresponding flow field is calculated by MSES. MSES does also contain some optimization options, but these were not used here since it makes no sense to optimize the flap for maximum lift when no flow control is applied.

In appendix B the MSES input files and the resulting pressure distributions are shown. With free transition, a nice flow field was found when the flap nose is located at coordinates (0.91;-0.04) with a deflection angle of 35°. However, when a fully turbulent simulation is performed, which is also the case when Fluent is used, no converging solution is found. With a flap deflection of 30° it was possible to obtain a fully turbulent solution. This solution showed much more flow separation than the free transition solution. However,

because the flow separation in the free transition solution of 35° was quite mild, it was still decided to use this deflection angle for the final configuration. The final configuration is shown in figure 6.5 and its coordinates are listed in appendix C.

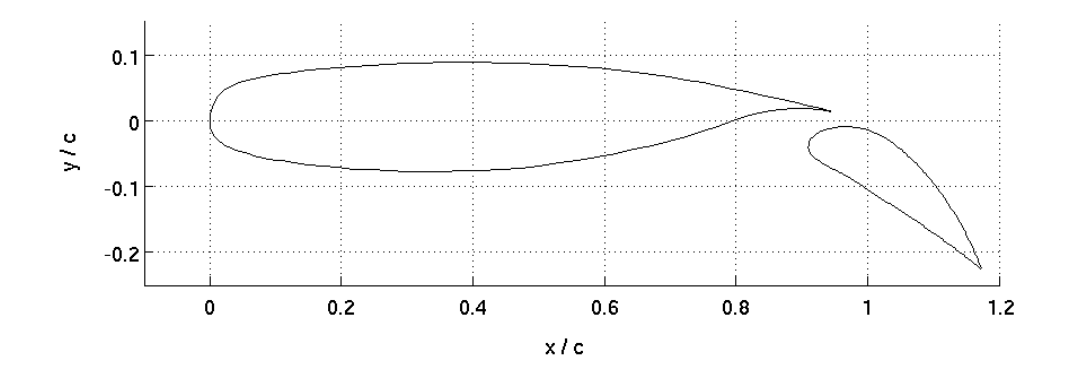


Figure 6.5: Geometry of the main airfoil (NLR7301) and the new flap.

6.2.3 Results of steady simulation

The analysis of the adapted configuration starts with a steady simulation. The conditions in the simulation are equal to the conditions in which the original NLR configuration was tested. That means that the main airfoil has an angle of attack equal to zero and the Mach number of the freestream flow is set to 0.185. This results in a Reynolds number of $4.0 \cdot 10^6$. Again it must be remarked that several unsteady effects occur in this situation. So the steady simulation shows oscillatory convergence, and the results presented can differ slightly from time to time.

In figure 6.6 a contour plot of the x-velocity distribution in the region around the flap nose is shown. Due to the changes in flap shape, position and deflection, flow separation now starts considerably further away from the flap leading edge. A large region of attached flow exists in which the fliperon can be implemented.

In order to obtain the exact separation location, the distribution of the skin friction coefficient is studied. As can be seen from figure 6.7, flow separation occurs at x/c = 1.11. It can be calculated that this point is located at about 63% of the flap chord.

The uncontrolled flow around the new configuration resulted in a total lift coefficient of about 2.97. The corresponding drag and moment coefficients are about 0.08 and 0.8, respectively. Remark that also these values are not fully converged, so small changes remain possible. The values for the aerodynamic coefficients that were predicted by MSES show large differences with the Fluent results. Since MSES is a panel code, it is known that it becomes less accurate if a large amount of flow separation occurs [9]. Therefore the result-

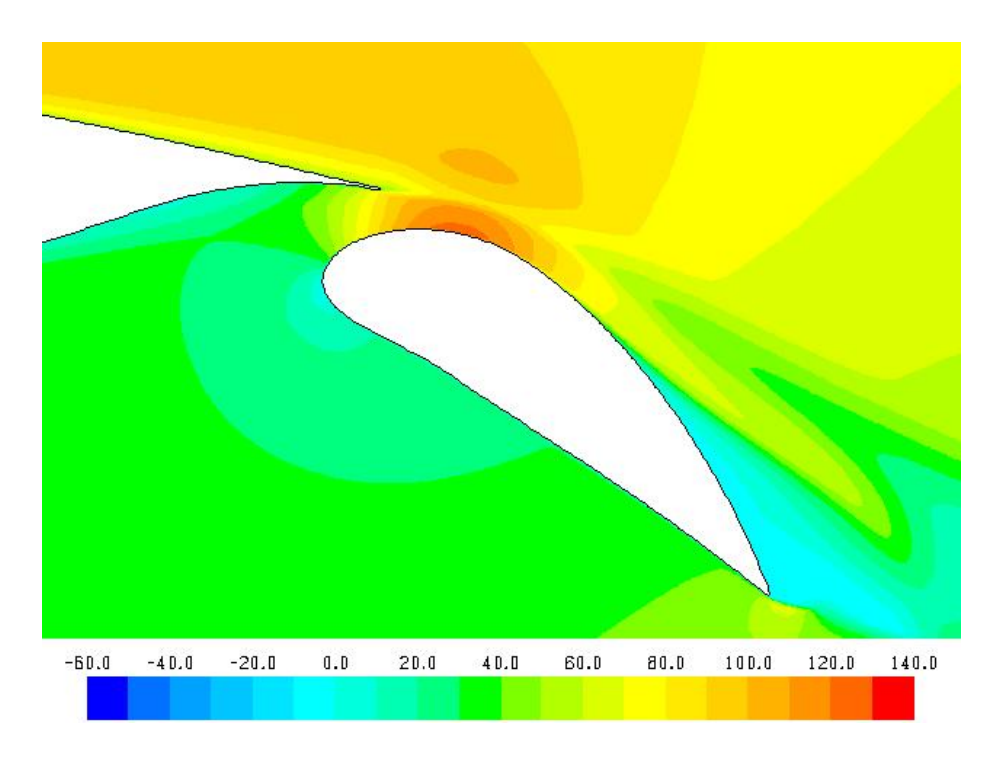


Figure 6.6: Contour plot of the x-velocity. On the adapted configuration flow separation does not occur on the first half of the flap surface.

ing aerodynamic coefficients of the MSES calculation should not be used here. MSES was only used to get an indication of the flow field in order to find a flap position.

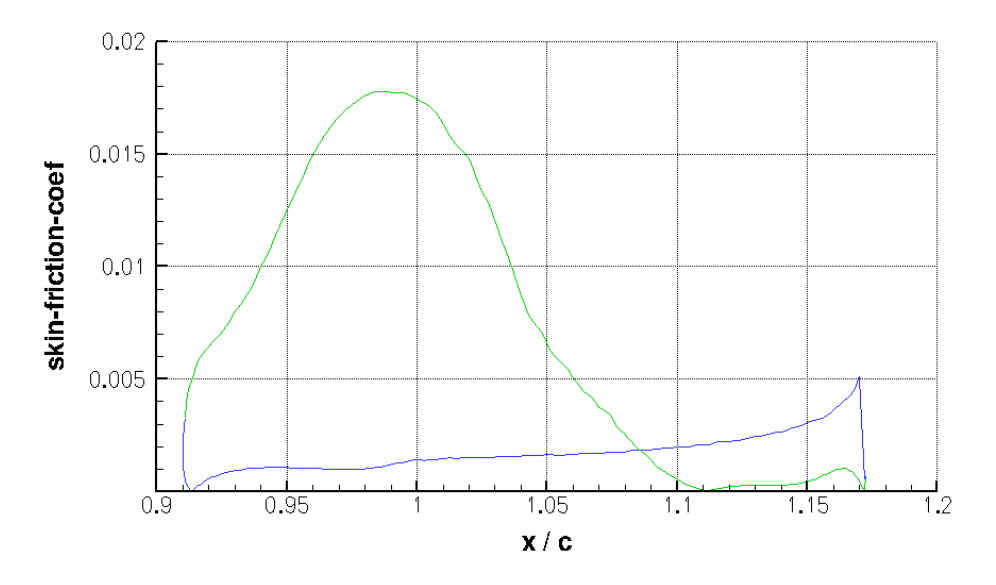


Figure 6.7: Skin friction coefficient at the flap upper surface (green) and lower surface (blue).

6.3 Flow separation control

From the test case with the NACA-0015 airfoil it was learned that the fliperon should be placed at a small distance ahead of the separation point. In that case the distance was about 23% of the airfoil chord. In the current case flow separation occurs at about 63% of the flap and therefore the fliperon (hinge) is placed at 43% of the flap chord (x/c = 1.065). Because there is no flow separation at the main element, no flow control is applied there. At the location of the fliperon, the boundary layer has a thickness of about 10 mm. The maximum fliperon deflection angle that is needed to reach an amplitude ratio of 1.0 is set at 25° (for the cavity type fliperon). This value is slightly lower than in the NACA-0015 case, in order to prevent dynamic mesh failures. The result is a fliperon with the same curvature as the flap upper surface and a length of 25.9 mm (8.1% flap chord length).

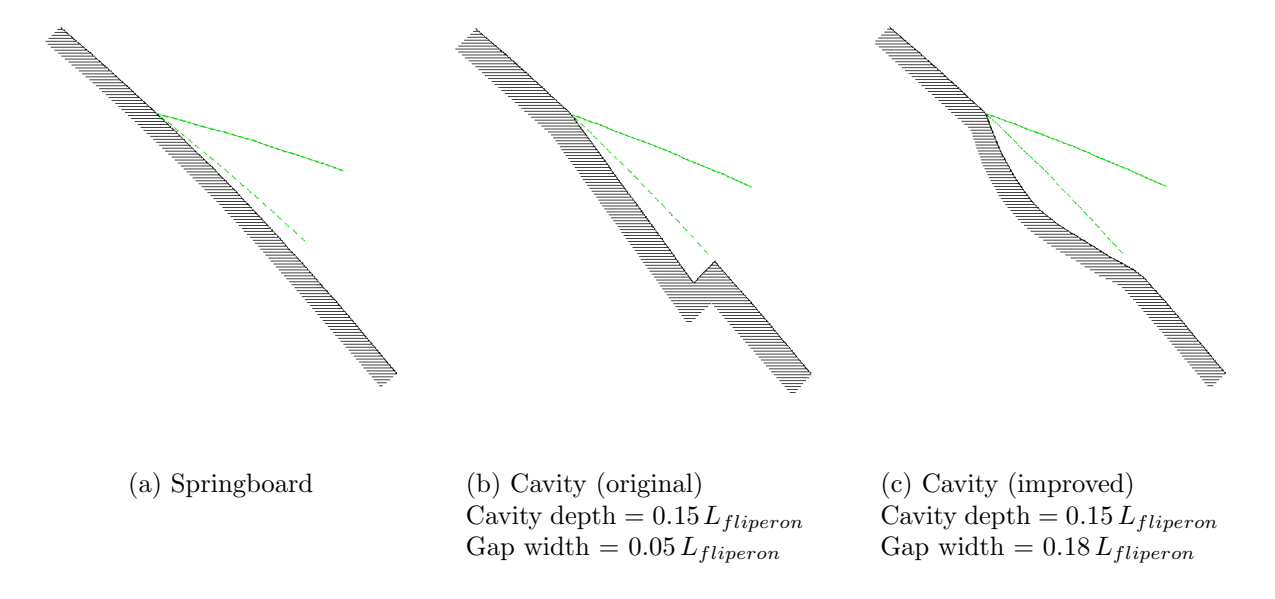


Figure 6.8: Overview of the different fliperon geometries applied on the flap of the NLR7301 configuration. The solid lines show the maximum fliperon deflection, the dashed lines indicate the minimum deflection angle (starting position of each oscillation).

For the NLR7301 airfoil-flap configuration three types of fliperons are used: the springboard type and the basic cavity type as introduced in section 2.2.3 and 5.2.1, and an improved cavity type in which the shape of the cavity is modified. The three fliperon geometries are also shown in figure 6.8. With all of these fliperon types several motions with different frequencies are performed. This means that a specific motion can be prescribed for more than one fliperon type. Remark that this can result in different amplitude ratios for the same motion, since the springboard type fliperon starts its motion with a deflection angle of 5° while both cavity type fliperons start without deflection. The frequency is completely defined by the prescription of the motion and is therefore independent of the type of fliperon that is used. The performed simulations are summarized in table 6.4.

001 m					
Fliperon type	Motion #	Oscillations	F^+	A_{max}/δ	C_{μ}
Springboard	I	64	4.0	1.2	0.1171
	II	143	6.0	1.2	0.2700
Cavity (original)	I	19	4.0	1.0	0.0198
	II	86	6.0	1.0	0.0834
	III	119	8.0	1.0	0.1065
Cavity (improved)	Ι	104	4.0	1.0	0.0872
	II	161	6.0	1.0	0.1443
	III	127	8.0	1.0	0.1497
	l IV	98	10.0	1.0	0.0892

Table 6.4: Overview of performed simulations in which flow control is applied on the NLR7301 airfoil-flap configuration.

From table 6.4 follows that the dimensionless frequencies applied here are much larger than the dimensionless frequencies applied on the NACA-0015 airfoil. This was necessary because the pressure gradients on the flap are much more adverse. This causes a stronger flow separation, which will require a larger momentum input and thus stronger vortices to reattach the flow to the flap surface. These stronger vortices can be generated by using higher frequencies than the frequencies used on the NACA-0015 airfoil.

In the coming sections the results of the simulations with the different fliperons are discussed. The first three sections will treat each fliperon geometry separately, such that the geometries can be compared in detail in the fourth section. Each section starts with the most general observation of the effect of flow control: the increase in lift coefficient. Then the vorticity field will be discussed, which is a first explanation for the lift behaviour. The sections end with the examination of several stages of a fliperon oscillation in order to investigate the exact influence of the geometry.

6.3.1 Springboard type fliperon

The performance of the springboard type fliperon was simulated with motions I and II. In figure 6.9 the development of the lift coefficient is plotted. Note that this displayed lift coefficient is time-averaged over each fliperon oscillation. This can be done since the lift coefficient looks like a sine function, with the same period as the fliperon motion. It was observed that the amplitude of the lift coefficient variation was significantly larger for the case in which motion II was prescribed. However, since the oscillations take place on a small scale, the effects do not influence the general performance of the airfoil-flap configuration. Therefore the general performance is best represented by the average aerodynamic coefficients. Although the average lift coefficients are not completely converged yet, their development is clear.

From figure 6.9 it becomes clear that the fliperon is certainly able to increase the lift coef-

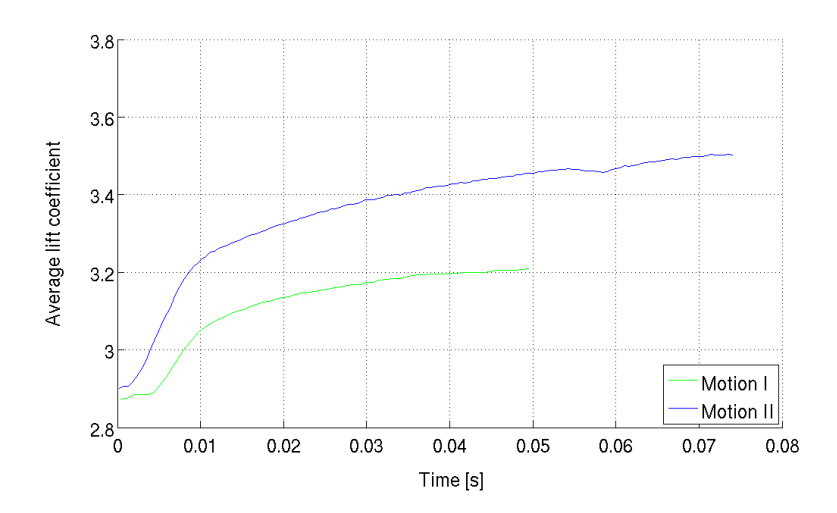


Figure 6.9: Development of the oscillation-averaged lift coefficient in time caused by the application of the springboard type fliperon.

ficient. At first instance, the lift coefficient decreases due to additional separation caused by the fliperon motion. When the first vortices arrive at the flap trailing edge, the lift starts increasing. When many vortices have passed the trailing edge, the system is fully developed and the lift coefficients converges slowly. In case of motion I the lift coefficient increases from 2.97 to 3.21, which is an increase of 8.0%. However, motion II turned out to result in a much better fliperon performance: the lift coefficient increases to 3.50, which is an increase of 18%. From table 6.4 follows that the momentum coefficient of motion II is also much larger than in case of motion I. This means that more momentum is added to the flow, and based on the lift coefficient it can be said that this additional momentum is used effectively.

In figure 6.10(a) the development of the aerodynamic moment coefficients (defined with respect to the quarter chord point x/c = 0.25) is plotted. The moment coefficient increases from 0.80 to 0.93 and 1.04 in case of motion I and motion II, respectively. The development in time shows many similarities with the development of the lift coefficient, but the convergence of the moment coefficients is slightly better. In the end the moment coefficients are more increased when more lift is generated, which can be a disadvantage in case of a landing aircraft because the forces on the horizontal tail plane have to increase to counteract the aerodynamic moment.

As can be seen from figure 6.10(b) the drag coefficients are not converged yet. It can be seen that these coefficients increase rapidly during the installation phase of the flow control, and then start decreasing slowly. The drag of the clean airfoil-flap configuration is about 0.08, so at this moment the drag is slightly larger. However, it is difficult to predict the final values of the drag coefficients and draw conclusions. It can only be remarked that for the situation of a landing aircraft, an increase in drag is not a problem.

As a consequence of the fliperon motion, the flow around the configuration has changed significantly. For both motion I and motion II the flow that was first separated has now

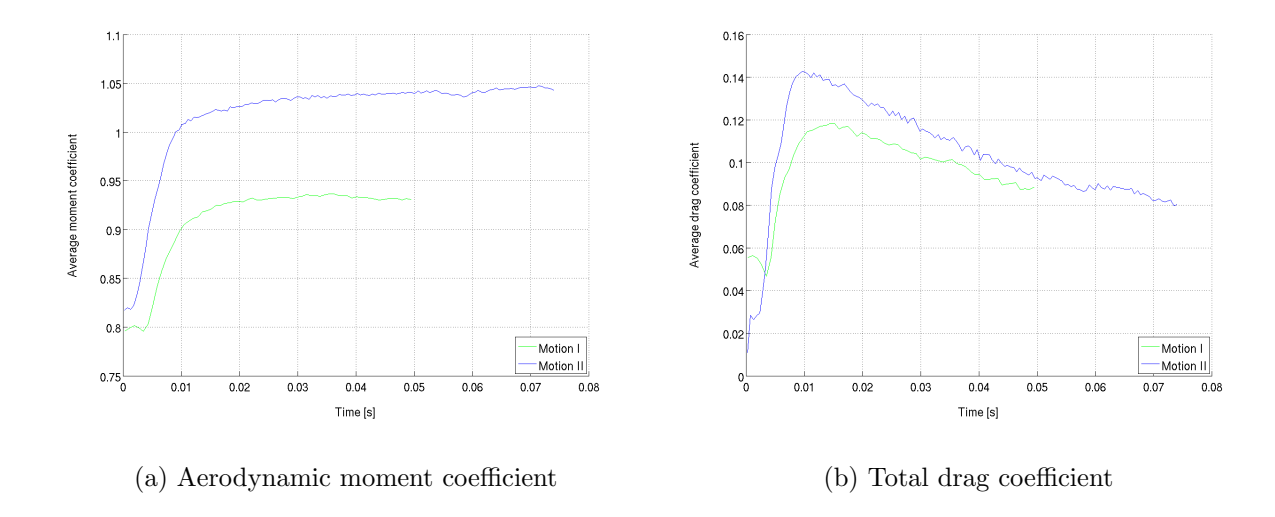


Figure 6.10: Development of the average aerodynamic coefficients in time when a spring-board type fliperon is applied.

reattached to the flap surface. In the same way as observed in the case of the NACA-0015 airfoil, the fliperon produces vortices that roll over the flap surface towards the trailing edge. At the trailing edge the vortices interact with the vortices that occurred from the separated flow. In this way the flow can reattach to the flap and the lift coefficient increases.

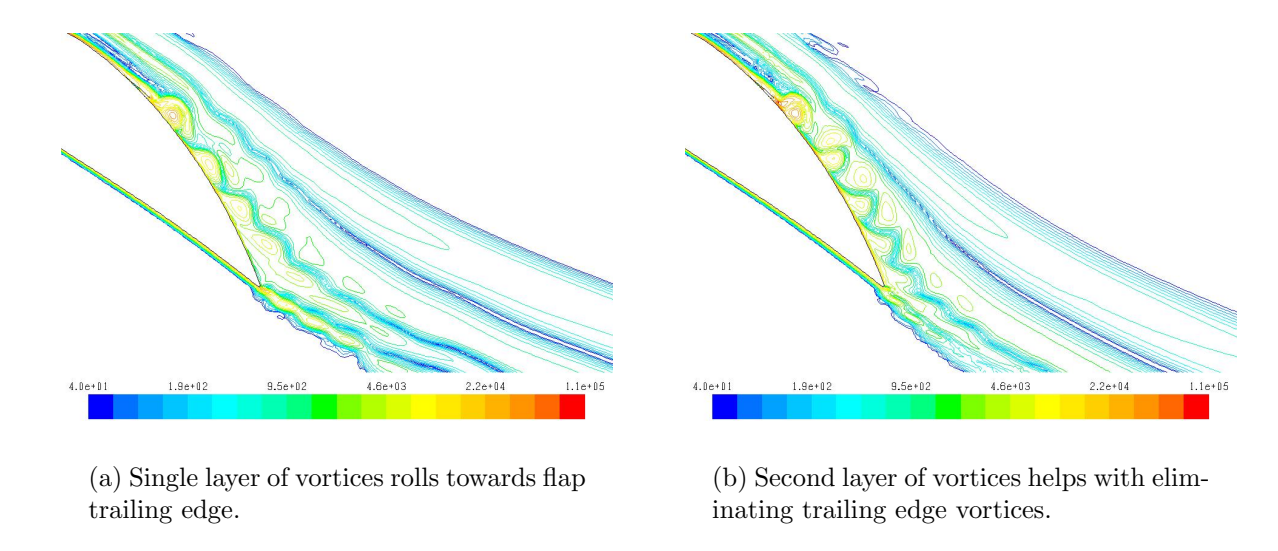


Figure 6.11: Developed of the vorticity field with the springboard type fliperon. The contours indicate the vorticity magnitude in s^{-1} .

In figure 6.11 an overview of the developed vorticity field is shown for both motion I and motion II. These are instantaneous pictures of the vorticity, both taken at a moment the fliperon was at its lowest position. It can be seen that motion II, with the highest

frequency, results in the production of smaller and stronger vortices. These vortices are able to reach the flap trailing edge, while the vortices produced by motion I separate from the flap surface slightly earlier. But the main difference is found in the so-called secondary vortices. The development of these vortices is shown schematically in figure 6.12. When the fliperon moves up, a large vortex is formed between the fliperon and the flap surface. At the beginning of the downward motion, this primary vortex leaves the fliperon and starts rolling over the flap surface. However, at the tip of the fliperon a second, smaller vortex is formed. In the case of motion I, this vortex is weak and lies more or less on top of the first vortex. These secondary vortices do not have a large influence on the first vortices that roll over the surface. However, in case of motion II the secondary vortex is quite strong. Although these vortices do not roll over the surface, they fit exactly between the primary vortices. This might help to keep the primary vortices attached to the surface and let them reach the trailing edge. It can be seen that motion II is the most effective, since the resulting trailing edge vortices and the flap wake are much smaller.

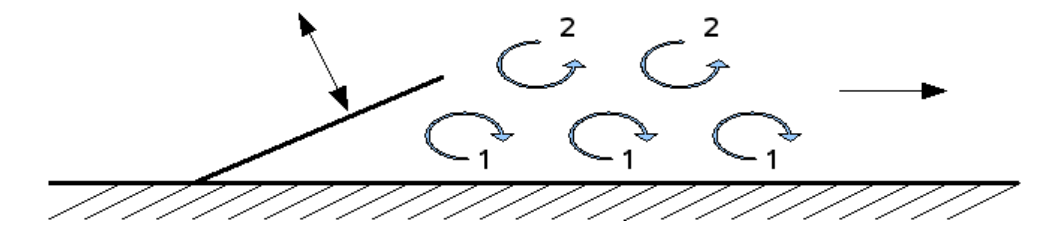


Figure 6.12: Schematic drawing of the development of (1) primary and (2) secondary vortices.

In order to get more insight into how the primary vortices and the secondary vortices develop, figure 6.13 shows a sequence of figures that zoom in on the fliperon. These pictures are taken from an oscillation in motion II, at a moment the flow field is already fully developed.

In figure 6.13(a), the fliperon is at the start of a new oscillation. This means automatically that the previous oscillation is just finished. The resulting vortices of that oscillation are still visible. Close to the fliperon tip a small vortex is seen. Later on it will become clear that this is the secondary vortex that originates from the fliperon tip. The large vortex that is seen next to the secondary vortex is the primary vortex produced in the previous oscillation. It can be seen that the primary vortex is attached to the flap surface.

Then the fliperon moves upward. From the vorticity field as shown in figure 6.13(b) is seen how a new primary vortex is generated. Air is sucked into the space between the fliperon and the flap surface, resulting in a clockwise rotating vortex. The secondary vortex is not generated yet, which can be seen from the contour lines that follow the upper surface of the fliperon. In the mean time the vortices of the previous oscillation move further towards the flap trailing edge. They increase in size and decrease in strength, but can still be recognized as a vortex pair.

In figure 6.13(c) the vorticity field is shown at the moment the fliperon deflection is maximal. The primary vortex has grown to its final size now and is about to leave the fliperon.

It can be seen that the vortex is also attached to the flap surface. In the corner of the figure can be seen how the previously generated vortices become larger and weaker while traveling further towards the trailing edge.

During the downward motion of the fliperon (figure 6.13(d)), the primary vortex has left the fliperon surface and is pushed into the boundary layer towards the trailing edge. Now the secondary vortex is generated which can be seen as the small vorticity contours at the fliperon tip. This secondary vortex rotates counter-clockwise, so opposite to the primary vortex. And then the sequence continues with a picture that looks very much like figure 6.13(a). The secondary vortex has also left the fliperon and follows the primary vortex towards the trailing edge. At this moment the secondary vortex is still close to the flap surface, but it is not sufficiently strong to follow the flap contour. The secondary vortices separate at a small distance behind the fliperon from the flap surface, but remain attached to their primary vortex (see figure 6.11(b)). When the vortex pairs arrive at the flap trailing edge, the main interaction with the existing vortices is done by the primary vortices. At that moment the secondary vortices are weak and too far away from the surface to interact as well.

6.3.2 Cavity type fliperon

The cavity type fliperon performed well on the NACA-0015 airfoil and therefore this type of fliperon is also applied on the NLR7301 airfoil-flap configuration. The shape of the cavity on the NACA-0015 airfoil was triangular, and this shape is also used here. In the next section another cavity geometry will be used and the influence of the cavity shape on the fliperon performance will be discussed.

With the original cavity type fliperon the motions I, II and III are performed. This results in fliperon oscillations with dimensionless frequencies of 4.0, 6.0 and 8.0, respectively. Figure 6.14 shows the development of the average lift coefficient for the performed motions. Again the lift coefficients show a clear periodic behaviour so the average value over each fliperon oscillation is plotted to keep the plot clear. It can be remarked that the higher the frequency, the larger the amplitudes of the oscillations. The lift coefficients are not completely converged yet, but their trend is clear and provides sufficient useful information.

From figure 6.14 can be seen that the frequency is still a highly important parameter that has a large influence on the final lift coefficient. In this case the higher frequencies perform much better than the lower frequencies, just as was seen in the case of the springboard type fliperon. Motion I is not able to increase the lift coefficient at all. With motions II and III applied to the original cavity type fliperon, lift coefficient increases of 9.1% and 13.7% are reached, respectively. From table 6.4 follows that the momentum coefficient behaviour corresponds with the lift coefficient behaviour since both increase with increasing frequency. Finally, it must be remarked that with the springboard type fliperon a dimensionless frequency of 4.0 was already sufficient to realize an increase in lift coefficient, while the same dimensionless frequency does not increase the lift coefficient

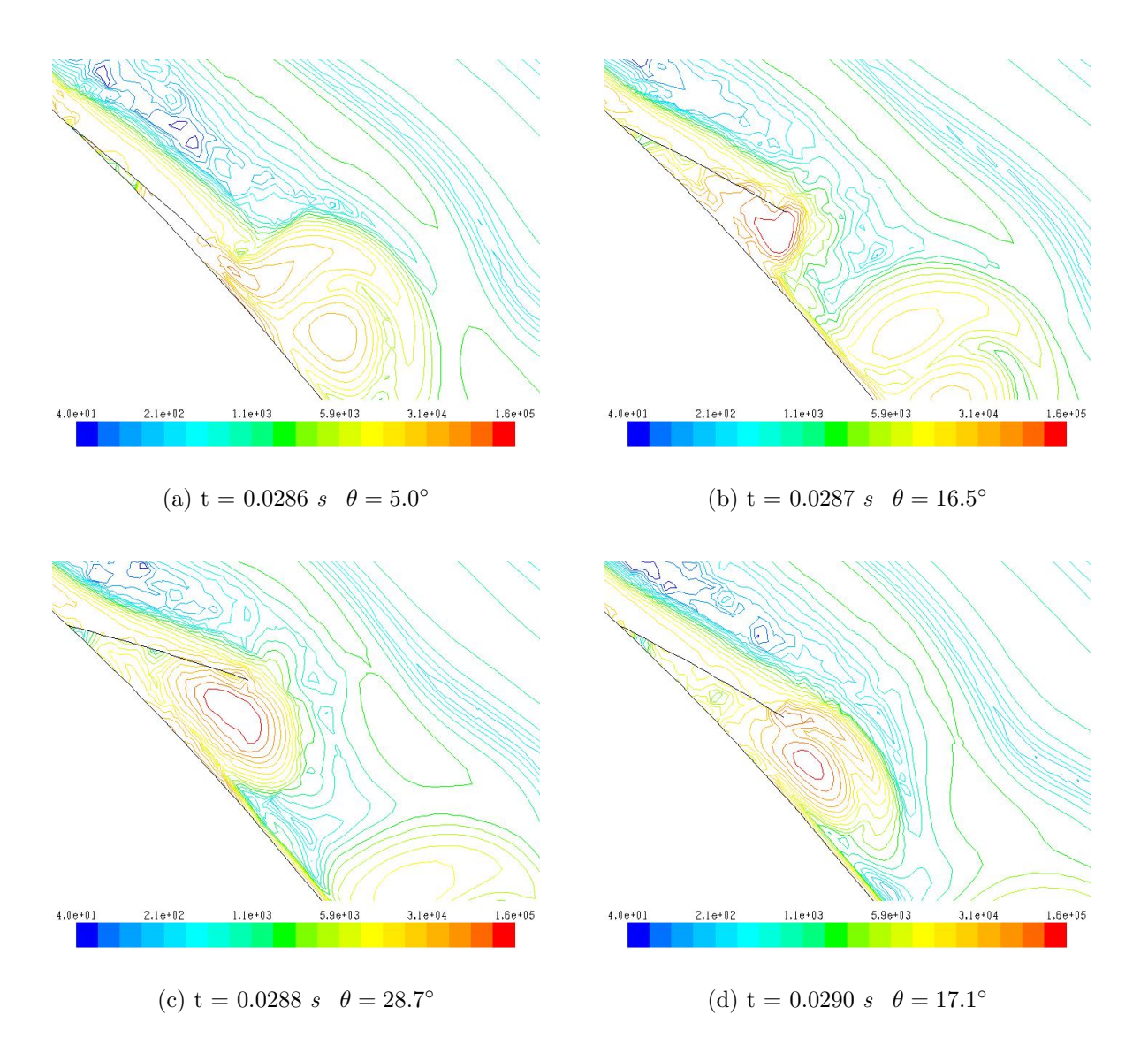


Figure 6.13: Development of the vorticity field during one oscillation of the springboard type fliperon in motion II: $F^+=6.0$, $A_{max}/\delta=1.2$ (vorticity in s^{-1}).

in this case. So the fliperon geometry is also a parameter that influences the final lift coefficient, as will be explained in more detail in section 6.3.4.

The development of the aerodynamic moment coefficients and drag coefficients is equal to the trends seen for the springboard type fliperon (figure 6.10). Again the moment coefficients converge quite good, while the convergence of the drag coefficients is poor. The values of the drag coefficients are lower in this case, and again motion II resulted in higher drag coefficients than motion I. The same can be said about the aerodynamic moment coefficients.

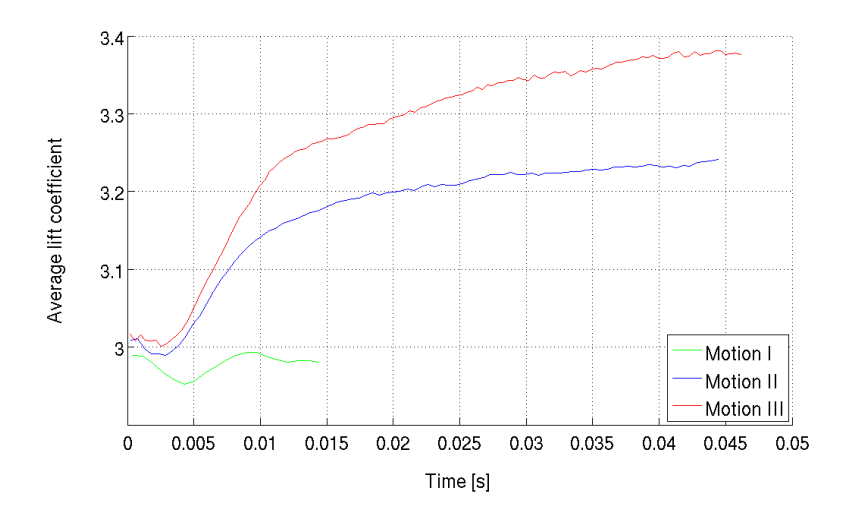


Figure 6.14: Development of the average lift coefficient in time when the fliperon oscillates above the original cavity.

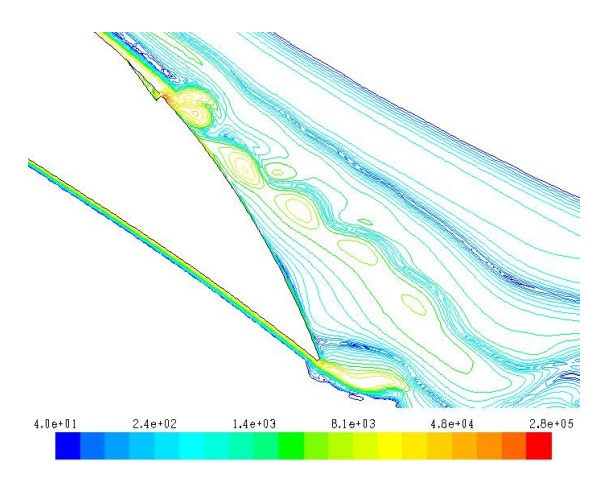
With each of the three motions prescribed to the fliperon the flow field changed. However, in case of motion I this did not result in reattachment of the separated flow. In the cases of motion II and motion III the flow over the complete flap reattached.

In order to understand the performance of the fliperon with different motions, the vorticity fields are plotted in figure 6.15. From figure 6.15(a) it becomes clear why the lift coefficient does not increase when motion I is prescribed. The vortices that are produced are by far not strong enough to reach the trailing edge of the flap. Instead they separate rather quickly from the flap surface and dissipate into the main flow.

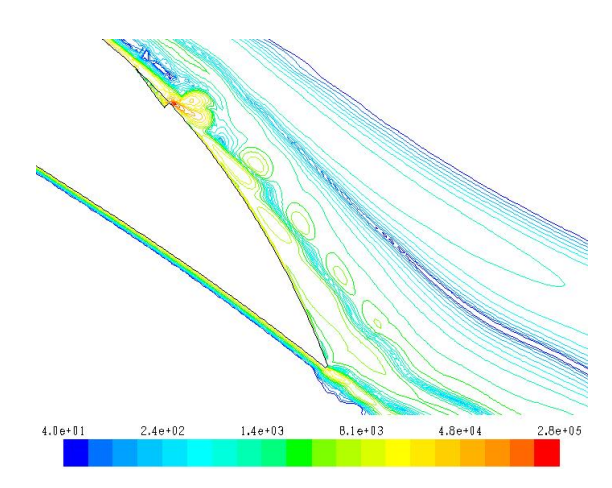
With increasing frequency the vortices become smaller in size and stronger, as can be seen from figure 6.15(b). The vortices of motion II are just strong enough to reach the flap trailing edge. They interact with the existing vortices, but still a rather large wake remains. Also a stream of secondary vortices is seen. These secondary vortices lie on top of their primary vortex and have about the same strength. It is difficult to indicate the influence of the secondary vortices, but since they are further away from the flap surface their influence on the reattachment of the boundary layer will not be extremely large.

The same phenomena are seen in the case motion III is applied to the fliperon. Due to the higher frequency the primary vortices are stronger, so now they can easily reach the trailing edge. The secondary vortices remain closer to the flap surface in this case, but still

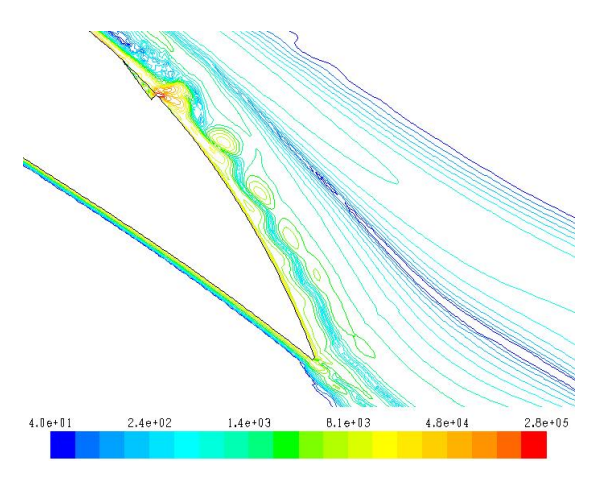
they lie partly on top of the primary vortices. This will limit their influence on the primary vortices and on the vortices that already existed from the separated flow. However, the primary vortices show a strong interaction with the existing vortices and are able to reduce the size of the wake significantly.



(a) The vortices of motion I separate from the flap surface and do not influence the trailing edge vortices significantly.



(b) When motion II is applied the vortices just arrive at the trailing edge and influence the existing vortices.



(c) The vortices produced from motion III are stronger and interact with the existing vortices, resulting in a reduction of the wake.

Figure 6.15: Vorticity fields resulting from different motions of the original cavity type fliperon. Contours indicate vorticity magnitude in s^{-1} .

It has already become clear that the geometry of the fliperon configuration has a significant influence on the performance of the fliperon. In order to find out what the differences are,

the generation of a vortex during a fliperon oscillation with the cavity geometry is plotted in figure 6.16. The figures display the fully developed flow field of motion II, so a large number of oscillations has already been performed before this oscillation starts.

In figure 6.16(a) the fliperon is at its lowest point. The vortices of the previous oscillation are still close to the fliperon. They are not completely developed yet, because up till this moment air was blown out of the cavity by the downward moving fliperon. It can be seen that the primary vortex is a little flattened, its shape is not circular. This is also a consequence of the blowing effect that occurs from the cavity. The secondary vortex lies on top of the primary vortex. It moves at a larger distance from the flap and is less influenced by the blowing effect. Therefore its shape is more circular.

In figure 6.16(b) the fliperon is moving upward and air is sucked into the cavity. It can be seen that a small, clockwise rotating vortex is generated at the fliperon tip. Next to this a counter-clockwise rotating vortex is formed at the trailing edge of the cavity. The vortices of the previous oscillation are still located rather close to the fliperon and have obtained their final shape now. It can be seen that due to the blowing effect of the cavity, the primary vortex has an elliptical shape. The secondary vortex, that is generated outside the cavity, still has a much more circular shape.

When the fliperon has reached its maximum deflection angle, both the clockwise rotating vortex at the fliperon and the counter-clockwise rotating vortex in the cavity have grown significantly. In figure 6.16(c) can be seen that the two vortices fill up the whole cavity. At this moment the suction of air into the cavity stops, and the cavity will start blowing the air out. This is also the moment at which the primary vortex will separate from the fliperon. The vortices of the previous oscillation are also still visible. They move together towards the trailing edge while their size increases and their strength decreases.

Figure 6.16(d) shows how the primary vortex is pushed and blown away into the boundary layer during the downward motion of the fliperon. The vortex that is still located inside the cavity decreases in size and strength, but it can also be seen that small vortex structures separate from this vortex and are pushed out of the cavity into the boundary layer. Further the secondary vortex is generated at the fliperon tip (upper side), rotating in a counterclockwise direction.

And now the situation of figure 6.16(a) returns. The secondary vortex has also left the fliperon now and lies on top of the primary vortex. Both the primary and the secondary vortex are significantly influenced by the vorticity structures that are blown out of the cavity, including the final structures of the large vortex at the cavity trailing edge. At this moment the vorticity structures are still interacting with the main vortices, therefore these vortices do not have their final shape yet.

6.3.3 Improved cavity type fliperon

In the previous section was already seen that the geometry of the fliperon configuration influences the vortices that are produced and so influences the resulting lift coefficient. In order to increase the lift coefficients further, an attempt was made to improve the original triangular cavity. The original cavity has a sharp corner at its trailing edge that

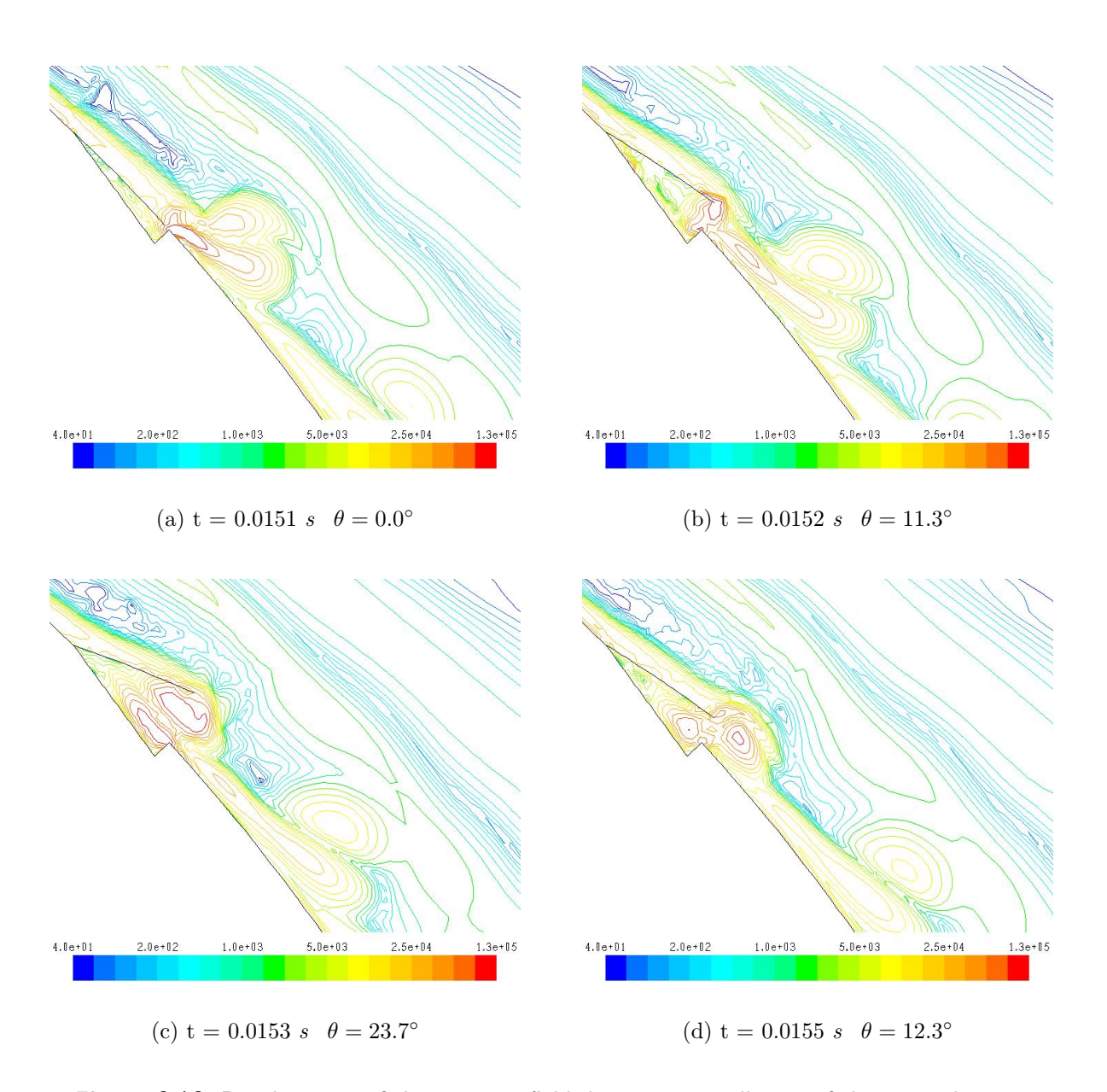


Figure 6.16: Development of the vorticity field during one oscillation of the original cavity type fliperon in motion II: $F^+=6.0$, $A_{max}/\delta=1.0$ (vorticity in s^{-1}).

causes additional vorticity. In the design of the new cavity only round shapes are used to prevent this additional vorticity. In order to enlarge the blowing effect of the cavity during the downward motion of the fliperon, the gap is enlarged while the outlet channel is made more narrow. This should also lead to an outflow that is more aligned with the flap surface. The resulting new cavity can be seen in figure 6.8(c). It must be remarked here that only the shape of the cavity has changed; the size and shape of the fliperon are still the same.

To investigate the influence of the new cavity geometry, 4 different motions are prescribed for the fliperon. These are the motions I till III that were also prescribed for the fliperon above the original cavity and the new motion IV in which the dimensionless frequency is increased to 10.0. Figure 6.17 shows the developments of the average lift coefficients, again with the remark that the non-averaged lift coefficients show oscillatory behaviour with the same frequency as the fliperon. Although not all lift coefficients are converged yet, the trends are clear. From the plot can be seen that motion II with a dimensionless frequency of 6.0 results in the largest increase in lift coefficient. The lift coefficient rises from 2.97 to 3.60, an increase of 21.2%. A lower frequency (motion I) can also perform quite well, but with a lift increase of 18.8% it is less effective. The same holds for motion III ($F^+ = 8.0$), which shows an increase in lift coefficient of 16.8%. Motion IV, the motion with the highest frequency, is clearly not that effective since only a small increase of 9.3% in lift coefficient is achieved. So the earlier observed trend that larger frequencies result in larger lift increases does not hold in this case.

The aerodynamic moment coefficients and the drag coefficients develop in the same way as was seen in case of the springboard type fliperon (figure 6.10). The momentum coefficients converge and end up at a larger value in case of motion I, but at about the same value in case of motion II when compared to the springboard type fliperon. The drag coefficients are again not converged, they keep decreasing every fliperon oscillation. For both motions the drag coefficients of the improved cavity type fliperon are larger than the drag coefficients of the springboard type fliperon.

Although the development of the lift coefficient is strongly dependend on the prescribed motion, it was observed that in all cases the flow reattached to the flap surface completely. The developed vorticity fields of the motions I till IV, that are shown in figure 6.18, reveal more about the lift increases that are obtained with the different motions.

In figure 6.18(a) the developed vorticity field resulting from motion I is shown. It can be seen that the produced vortices have a limited strength and are not of circular shape due to the blowing effect of the cavity. However, the primary vortices are strong enough to reach the trailing edge of the flap and interact with the existing vortices. The secondary vortices of motion I are rather weak. They dissipate before they can reach the trailing edge and do not contribute directly to the trailing edge interaction. Furthermore it can be seen from the figure that the frequency of motion I is in fact too low. Between each vortex pair some sort of empty space is seen, so the vortices do not form a tight stream. On the NACA-0015 airfoil was observed that the better the vortices fit together, the larger the

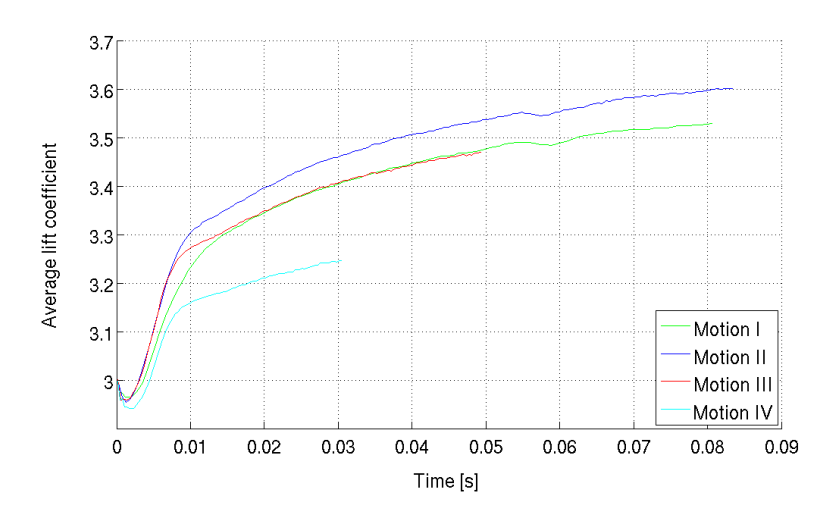


Figure 6.17: Development of the average lift coefficient in time when the fliperon oscillates above the new cavity.

From figure 6.18(b) can be seen that due to the increased frequency the vortices produced

increase in lift coefficient.

by motion II are stronger than the vortices of motion I. This holds for the primary vortices, but even more for the secondary vortices. It is also remarkable that the secondary vortices are much larger than the primary vortices. The primary vortices can reach the flap trailing edge easily, but their shape becomes more elliptical when they move further over the flap. With the application of motion II also the secondary vortices can reach the trailing edge. However, the secondary vortices are further away from the flap surface than the primary vortices, which means that the interaction with the existing trailing edge vortices is performed primarely by the primary vortices. Further it can be seen that the secondary vortices remain attached to their primary vortex and push it towards the flap surface when traveling downstream. The vortex pairs fit better together than in the case of motion I, which is an explanation for the larger increase in lift coefficient. However, small empty spaces between the vortex pairs remain visible so this frequency is still not optimal. Increasing the frequency further, as was done with the application of motion III, suddenly results in a different vorticity field, see figure 6.18(c). In order to understand how this vorticity field has occurred, a complete oscillation was examined. It turns out that when the fliperon is at its maximum deflection, the clockwise vortex is still rather small and does not cover the whole cavity area. This vortex does not leave the fliperon and is pushed into the cavity during the downward motion. In the same time also the counterclockwise secondary vortex is generated. When the fliperon approaches its most downward position, all vortex structures are pushed out of the cavity. At first instance a primary and a secondary vortex are visible (in figure 6.18(c) the vortex pair that is most close to the fliperon tip), but due to all vortex structures that are pushed out of the cavity the secondary vortex becomes much stronger than the primary vortex. After another fliperon oscillation the primary vortex is weakened even more and is pushed away from the flap

surface by the secondary vortex (the second and third vortex pairs in figure 6.18(c)). So now the secondary vortices must interact with the existing vortices at the trailing edge. However, the secondary vortices slightly tend to separate from the flap surface and dissipate rather fast, resulting in a thicker boundary layer at the flap trailing edge and a smaller wake reduction. It is clear that this frequency is beyond the optimum frequency for this cavity shape.

When motion IV with frequency 10.0 is applied, the situation only gets worse. Basically the same phenomena are observed as in the case of motion III, but now even stronger. In figure 6.18(d) can be seen that the difference in strength between the primary vortex and the secondary vortex is much larger in this case. Consequently, the primary vortices are earlier pushed away from the flap surface. The secondary vortices are almost completely dissipated before they reach the trailing edge, so no interaction can take place. This explains the small increase in lift coefficient that was found when motion IV is applied.

In order to compare the different cavity geometries, the development of vorticity during a fliperon oscillation is shown in figure 6.19. This figure shows the completely developed vorticity field when motion II is applied.

In figure 6.19(a) the fliperon is in its lowest position. At this moment a lot of vorticity structures are blown out of the cavity and interact with the primary and the secondary vortex created in the oscillation that is just finished. These vortices are still located close to the fliperon tip and can be changed easily by the blown-out vortex structures.

During the upward motion of the fliperon air is sucked into the cavity and a clockwise vortex is generated at the fliperon tip, as can be seen in figure 6.19(b). The vortices of the previous oscillation have obtained their final shape now and have eliminated the small vortex structures that were blown out of the cavity. The vortices are still attached to each other and to the flap surface when moving towards the trailing edge.

When the fliperon is at its maximum deflection, the situation as shown in figure 6.19(c) occurs. It is observed that the primary vortex does not fill the whole cavity and is also not of circular shape. The vortex is located quite far into the cavity and therefore it can not leave the fliperon at this moment.

When the fliperon moves downward, shown in figure 6.19(d), the primary vortex is still not separated. This means that it get squeezed and it is partly pushed into the cavity. At the fliperon tip the secondary, counter-clockwise rotating vortex is formed, influenced by the part of the primary vortex that was located close to the tip in the previous time steps. Just before the fliperon is at its lowest position, the primary vortex separates from the fliperon and is pushed into the boundary layer. Also a lot of other vortical structures that were first located inside the cavity are blown out. And then the situation of figure 6.19(a) returns, in which also the secondary vortex has left the fliperon tip and starts moving towards the trailing edge. Both the primary and the secondary vortex are strongly influenced by the small vortical structures that are blown out of the cavity and interact with each other and with the main vortices.

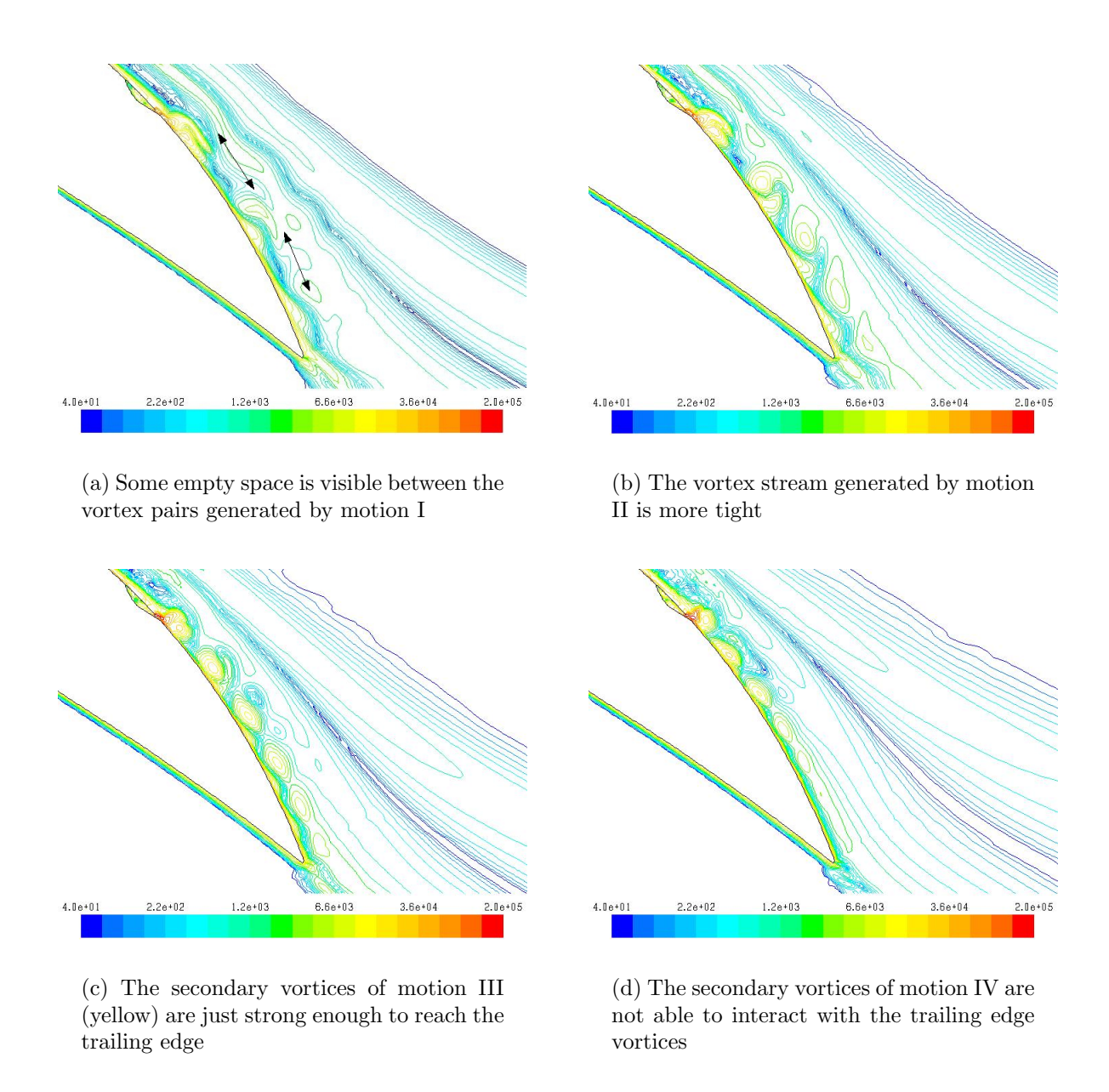


Figure 6.18: Vorticity fields resulting from different motions applied to the fliperon above the new cavity. Contours indicate vorticity magnitude in s^{-1} .

6.3.4 Comparison of geometries

In the previous sections it has become clear that the geometry of the fliperon configuration has a large influence on the results of a certain fliperon motion. The results of the motions applied to the different fliperon geometries are summarized in table 6.5. It can be seen that the same motion, when applied to different geometries, results in different momentum coefficients and different increases in lift coefficient.

Motion I is already a good example of the extremely large differences between the fliperon

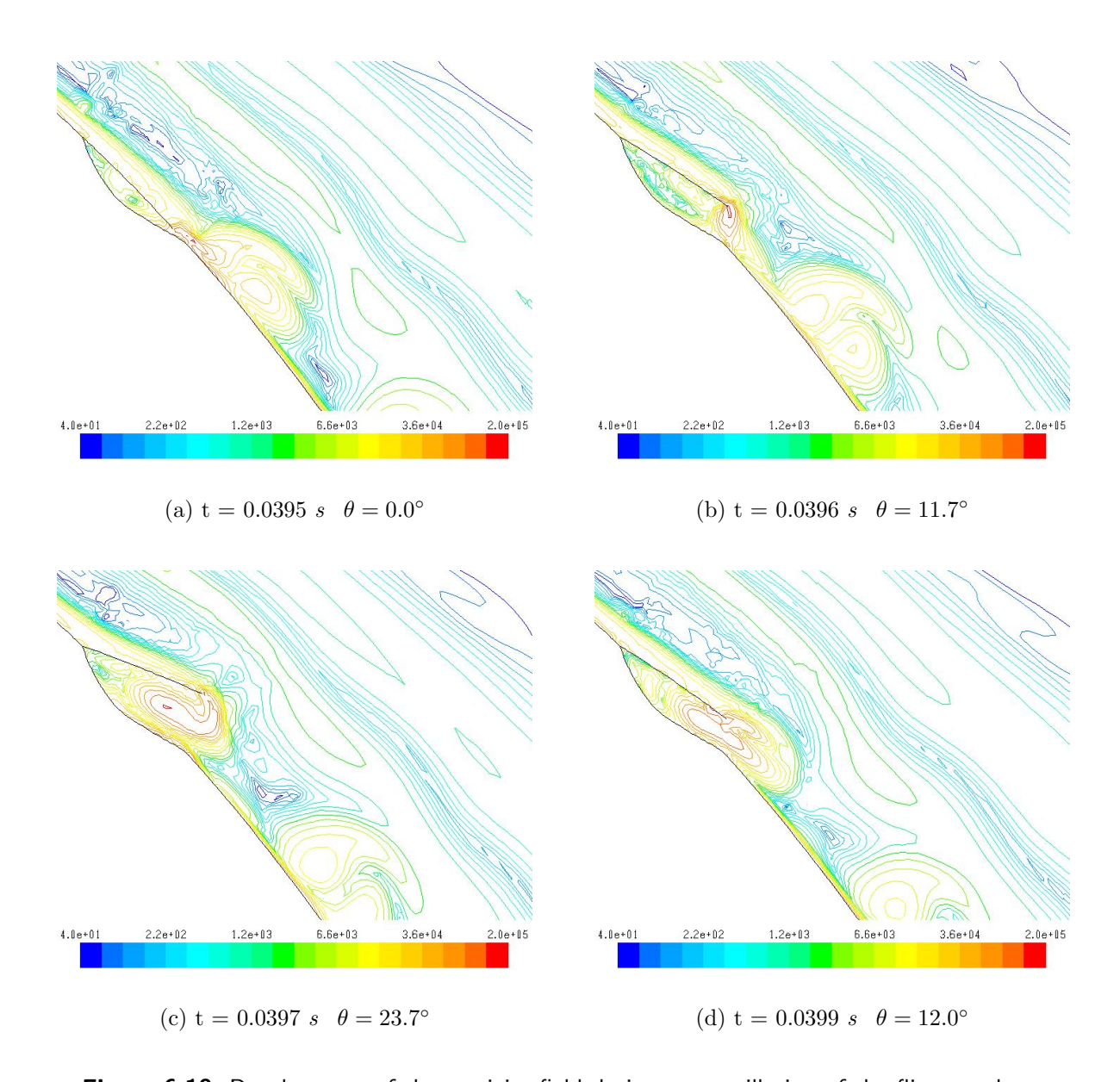


Figure 6.19: Development of the vorticity field during one oscillation of the fliperon above the new cavity (vorticity in s^{-1}). Motion II: $F^+=6.0$, $A_{max}/\delta=1.0$

configurations. With the fliperon oscillating above the original cavity, no lift increase is obtained at all, while changing the cavity shape can increase the lift coefficient with 17%. The performance of the springboard type fliperon is found in between of these extremes. In case of motion II the ranking of the configurations is the same as in case of motion I. Again the improved cavity configuration results in the largest increase in lift coefficient, while the performance of the springboard type fliperon is the second best. Also in case of motion III the improved cavity performs better than the original cavity.

Table 6.5: Overview of the resulting lift coefficient increases from different fliperon geometries.

Motion #	Fliperon type	C_{μ}	$\Delta C_L(\%)$
$I(F^+ = 4.0)$	Springboard	0.1171	8.0
	Cavity (original)	0.0198	0.0
	Cavity (improved)	0.0872	18.8
II $(F^+ = 6.0)$	Springboard	0.2700	18.0
	Cavity (original)	0.0834	9.1
	Cavity (improved)	0.1443	21.2
III $(F^+ = 8.0)$	Cavity (original)	0.1065	13.7
	Cavity (improved)	0.1497	16.8

One of the reasons that explain the rather bad performance of fliperon motions above the original cavity is the formation of the additional vortex at the trailing edge of the cavity (figure 6.19(c)). This vortex occupies a lot of cavity space, which leaves less space for the primary vortex that occurs on the lower side of the fliperon. In this way the primary vortex is limited in its maximum size and strength. The additional vortex causes the primary vortex to separate from the fliperon tip during the downward motion. But when the fliperon is almost at its lowest position, an enormous amount of vortical structures is blown out of the cavity. It is not proven here, but it is well possible that these vortical structures have a negative effect on the primary and secondary vortices. In fact the available space below the fliperon is more or less equal to the space that is available below the springboard type fliperon. However, because there is no additional vortex in case of the springboard type fliperon, the amount of vortical structures that is blown into the boundary layer is much smaller.

The limited performance of the original cavity geometry is also illustrated by the momentum coefficient, that is for all motions lower than the momentum coefficients of the springboard type fliperon and the improved cavity type fliperon. Next to the negative influence of the additional vorticity, also the direction of the flow out of the cavity plays a role here. Since the original cavity has a straight trailing edge, the largest part of the outflow will be directed upward. The momentum coefficient is based on the flow velocity parallel to the flap surface, so the direction of the outflow is not optimal for a large momentum coefficient.

In case of the springboard type fliperon, a large disadvantage occurs before the

fliperon starts oscillating. Since the springboard type fliperon always has a small deflection angle it causes the flow to separate already at the location of the fliperon. This means that the springboard type fliperon has to perform better to obtain the same amount of attached flow as a cavity type fliperon. The simulations have shown that the springboard type fliperon does perform quite good: one large primary vortex is generated and there are no negative influences of small vortical structures. The values of the momentum coefficient show that with both motions the springboard type fliperon transfers the largest amount of momentum to the boundary layer. However, this does not fully compensate the additional flow separation and therefore the springboard type fliperon is not able to realize the largest lift coefficient increase for both motion I and motion II.

The new designed cavity seems to be a real improvement, because it eliminates the two main disadvantages of the other fliperon configurations. Since a cavity is used no additional flow separation occurs and since the sharp trailing edge of the cavity is removed no additional vortices occur. Still an amount of vortical structures is blown out of the cavity at the end of the fliperon oscillation, but this amount is smaller than the amount that is blown out in case of the original cavity. So the mass flow that comes out of the cavity remains more or less equal is size, but the flow is less turbulent and better aligned with the flap surface. This improves the effectiveness of the fliperon configuration. This is also supported by the momentum coefficient, which is always larger with the improved cavity than with the original cavity. The momentum coefficient of the springboard type fliperon is still much larger, but that can also be caused by the larger amplitude ratio of the springboard type fliperon.

Although the new cavity shape improved the increase in lift coefficients, it is difficult to indicate the exact influence of the cavity shape on the performance of the fliperon. The blowing effect that occurs during the last part of the downward motion of the fliperon results in an air flow that contains vortical structures, but these structures could not be investigated to a sufficient level of detail to determine their source and development. Also the exact influence of these structures on the primary and secondary vortices could not be revealed in sufficient detail. Therefore it can not be said wether this new cavity is optimal, or if it should be optimized further. Performing a Large Eddy Simulation (LES) can probably lead to an answer for this remaining question, otherwise a Direct Numerical Simulation (DNS) will be required.

6.4 Fliperon versus other types of flow control

In the previous section was shown that flow control with an oscillating fliperon can be applied to increase the lift coefficient of an airfoil-flap configuration. From section 2.2 it is known that there are more flow control techniques available that can be used in a situation like this. In section 2.4 the performance of flow control by means of a fliperon was compared to other types of flow control. That comparison was a general comparison

in order to indicate the range of lift coefficient improvements that can be expected with a certain flow control method. In this section again different flow control methods will be compared, but now the focus is on the application of flow separation control on a flap. In this way an indication of the effectiveness and efficiency of a fliperon can be obtained for this specific situation.

First some passive flow control techniques are revisited. In [13], Klausmeyer et al illustrate the application of vortex generators on the flap of a three element configuration. The leading edge slat was deflected over 30°, the flap over 35°. This resulted in flow separation at 40% of the flap chord. With the vortex generators applied at 20% flap chord, the flow reattached completely and the lift coefficient increased by 4.5%.

The self-activated movable flap of [20] that was discussed in section 2.2.1 can theoretically also be applied on the flap of the airfoil-flap configuration. In [20] the self-activated movable flap was applied on a single element airfoil and lead to more than 10% increase in total lift coefficient.

Of course a lot more research about the application of passive flow control devices has taken place. However, these two examples illustrate the order of magnitude of the lift improvement that can be reached. The lift coefficient increases that were obtained with the application of the fliperon on the flap were larger, but it should not be forgotten that the fliperon is an active flow control device. This means that some disadvantages like power consumption, additional complexity and weight are the drawbacks of the larger lift increase.

In that way it is more objective to compare the performance of the fliperon with other types of active flow control on flaps. Greenblatt [10] provides an overview of both research in which acoustic excitation (synthetic jets) is applied, and research in which periodic excitation is used. Focusing on the researches in which periodic excitation is applied on flapped configurations, it is observed that enormous increases of about 80% in post-stall lift coefficients are reported. But this is merely caused by the definition used. According to [10], the maximum post-stall ΔC_L is the difference between the maximum lift coefficient with flow control and the corresponding lift coefficient, at the same angle of attack, of the case without flow control. However, in case of the NLR7301 airfoil-flap configuration only one angle of attack and one flap deflection angle were investigated. Based on these results it is difficult to predict the maximum post-stall ΔC_L , but it is expected that this value is larger than the lift increase found now. Therefore no further comparison with those results in [10] is made. However, it can still be remarked that in general lower momentum coefficients of the order of 10^{-2} are used, in situations with Reynolds numbers that are also an order of magnitude smaller.

In order to indicate the efficiency of the fliperon, two specific examples of active flow control researches can be mentioned. In the first research an airfoil flap configuration is investigated by Petz and Nitsche [19]. Oscillatory blowing with a dimensionless frequency of 0.9 and a momentum coefficient of 0.06% is applied at the leading edge of the flap. This delayed the onset of separation and resulted in a lift coefficient increase of 12%. This experiment was performed at a rather low Reynolds number of $0.55 \cdot 10^6$.

As was seen in the case of the NACA-0015 airfoil, also synthetic jets can be an efficient method of flow separation control. In [12] Kim and Kim present the results of flow control with a synthetic jet applied on a plain flap. The flap is part of the three element NACA-23012 airfoil configuration. The synthetic jet is located at the flap leading edge and operates at a dimensionless frequency of 1, with a momentum coefficient of 0.017. The resulting increase in lift coefficient raised to values of about 20%.

If the fliperon is now compared to other methods of flow separation control on flaps, it can be concluded that with a fliperon the same amount of lift coefficient increase can be reached. So the fliperon is an effective device for flow separation control.

In most reference researches the frequencies and the momentum coefficients used are much lower. This means that other methods of flow control can reach more or less the same effects with less momentum input, so the momentum is used more efficiently. However, since the fliperon will be used during the relatively short landing phase only, the power consumption of the flow control system is not that important. Therefore the larger momentum coefficients are not seen as a large disadvantage. Because the fliperon flow control system is less complex than the systems of several other flow control methods like boundary layer suction, periodic excitation or synthetic jet actuation, it will be less expensive and more reliable. With these advantages it can still be said that the fliperon is an efficient flow control device.

Conclusions and recommendations

7.1 Conclusions

In the outline of the thesis (section 1.2) was explained that the goal of this thesis was to numerically investigate the effectiveness and efficiency of flow separation control by means of an oscillating fliperon. Numerical RANS simulations in which this type of flow control was applied were performed successfully. Two configurations with a moderate amount of separated flow were investigated: the NACA-0015 airfoil at 20° angle of attack and the NLR7301 airfoil-flap configuration at zero angle of attack but with 35° flap deflection. With the results of the performed simulations it has now become possible to draw conclusions about the fliperon as flow separation control device. This section will present an overview of these conclusions, grouped by topic.

Fliperon design parameters

About the implementation of the fliperon can be concluded that the most forward point of the fliperon, the hinge, should be located at a distance of about 20% (flap) chord ahead of the flow separation point. The shape of the fliperon should be equal to the local airfoil curvature to minimize its disturbing effects when it is inoperative.

Further it was found that the length of the fliperon should be based on the local boundary layer thickness. When the fliperon is close to its maximum deflection, usually at a deflection angle of about 25°, the amplitude of the fliperon tip should be equal to the boundary layer thickness.

If the fliperon oscillates above a cavity, the shape of the cavity also influences the performance of the fliperon. It was shown that a cavity with a sharp trailing edge produces additional vorticity, which can have a negative influence on the vortices produced by the fliperon. A cavity with a smooth shape does not have this disadvantage and the fliperon performed clearly better in that case. Another possibility is to use a springboard type fliperon that oscillates above the airfoil surface and does not need a cavity. However, this fliperon type has the disadvantage that it causes additional flow separation because it is never completely aligned with the airfoil surface.

Fliperon motion

The motion that is prescribed for the fliperon has a large influence on the performance of the fliperon. In all cases the motion was defined by prescribing the angular velocity of the fliperon as a sine function. This made it possible to know the frequency and the maximum amplitude of the fliperon a priori.

The frequency turned out to be the most important parameter of the fliperon motion. Dimensionless frequencies with values of 1.0 or slightly higher values resulted into attached flow and increasing lift coefficients on the NACA-0015 airfoil. In case of the NLR7301 airfoil-flap configuration much higher frequencies were required due to the larger adverse pressure gradient. It turned out that a dimensionless frequency of 6.0 was close to the optimum.

The influence of the frequency on the fliperon performance can be explained as follows. During the upward motion of the fliperon, a vortex is generated at its lower side. At the start of the downward motion this vortex separates from the fliperon and is pushed into the boundary layer towards the trailing edge. Increasing the frequency of the fliperon motion leads to smaller and stronger vortices, that dissipate slowly. It is important that the produced vortices do not dissipate too fast, because they must travel to the trailing edge and interact with the vortices that existed there already as a consequence of the separated flow. This interaction will increase the total amount of circulation and so the lift coefficient. It is therefore important that a sufficiently large frequency is used. However, in case of the NLR7301 configuration was clearly shown that there is an optimum frequency beyond which the vorticity generation changes and the fliperon becomes less effective.

The maximum amplitude of the fliperon tip should be approximately equal to the local boundary layer thickness. Using larger amplitudes does not have much effect, because in that case the additional flow that is excited is flow outside the boundary layer that does not need additional momentum. If the maximum amplitude of the fliperon is much smaller than the boundary layer thickness only a small part of the boundary layer will be affected by the produced vortices. This is ineffective and will not lead to significant lift improvements.

Lift coefficient

Both on the NACA-0015 airfoil and on the NLR7301 airfoil-flap configuration the application of flow control by means of a fliperon resulted in increasing lift coefficients. In case of the NACA-0015 the maximum increase in lift coefficient was 20% with respect to the situation in which no flow control was applied. The amount of additional momentum that was transferred to the boundary layer flow, expressed in the momentum coefficient, was for that case 0.016. Compared to a reference research in which flow control on the NACA-0015 airfoil was applied by means of a synthetic jet, a larger lift increase was reached with the fliperon, while the momentum coefficient was slightly smaller in

the current case. Furthermore the fliperon is less complex than the synthetic jet. This makes the fliperon both an effective and an efficient device for flow control in this situation.

In case of the NLR7301 airfoil flap configuration the maximum increase in lift coefficient was obtained with a fliperon oscillating above a cavity with only round shapes. The maximum increase was 21.2% with respect to the uncontrolled situation. As a consequency of the higher frequencies that were necessary in this case, the momentum coefficients were also much larger. Corresponding to the maximum lift coefficient increase a momentum coefficient of 0.144 was found. This high value raises questions about the efficiency of the momentum transfer in this case. Comparable researches in which flow control was applied by means of synthetic jets or periodic excitation (blowing and suction) showed more or less the same increase in lift coefficients, but at much smaller momentum coefficients. However, these flow control methods require more complex flow control systems. Therefore it can still be said that the fliperon is an efficient flow control device on a flap configuration.

7.2 Recommendations for future research

The current research has answered many questions about flow control by means of a fliperon. However, by far not all questions are answered and several new questions arose. Additional research, both numerically and experimentally, can lead to valuable knowledge to improve this concept.

Numerical research

The current numerical research has raised questions for more in-depth research on the following topics:

- In case of the NACA-0015 airfoil, it would be interesting to optimize the flow control. This means in the first place that an optimum frequency has to be found. This frequency will be higher than the highest frequency that was applied in the current research. Furthermore the sharp trailing edge of the cavity should be removed and replaced by a round shape. When a new optimum is found, the new increase in lift coefficient and the corresponding momentum coefficient will indicate how effective and efficient the fliperon really is in this case.
- With respect to the NLR7301 airfoil flap configuration it is recommended to perform a Large Eddy Simulation (LES). Such a simulation should reveal the influence of the cavity shape in more detail, because the source and the development of small vorticity cells can be made visible. In this way the cavity shape can be improved further, which can lead to larger lift coefficient increases.

- In the performed numerical simulations the prescribed angular velocity of the fliperon was always a sine function. It would be interesting to investigate the effect of the prescribed function on the generated vortices. By applying other functions that for example have a different upward and downward speed, the blowing effect of the cavity can be optimized.
- In general it would be useful to investigate in which situations flow control and momentum transfer by means of a fliperon can be applied efficiently. The NACA-0015 airfoil was a situation in which this flow control method was very efficient, but the efficiency in case of the NLR7301 airfoil-flap configuration was lower. By investigating for example the NLR7301 configuration with a smaller flap deflection angle and the NACA-0015 airfoil at a larger angle of attack, a possible relation between the pressure gradients and the efficiency of the fliperon can be found. In this way it becomes clear what situations are primarely suitable for flow control by means of a fliperon.

Experimental research

The current numerical research has shown that flow control by means of a fliperon can also be effective on an airfoil-flap configuration. This reduces the risk of a wind tunnel experiment, in which a similar airfoil-flap configuration could be investigated. In order to set up the flow control system, the conclusions with respect to fliperon design should be taken into account. Further it is important that the drive system that controls the motion of the fliperon does not disturb the flow under the fliperon. Since the new flap of the NLR7301 configuration is quite thick, it should be possible to implement a small power supply system inside the flap.

A good experimental research is not only the ultimate validation of the numerical simulations, but also a possibility to investigate the flow and the possibilities of the flow control system in a different way. The following topics could be addressed in an experimental research:

- In a wind tunnel experiment it would be possible to investigate the power that is needed to operate the fliperon. This can be compared with the power needed to operate for example a synthetic jet, and in this way a more reliable conclusion about the efficiency of momentum transfer by means of a fliperon can be drawn.
- In a wind tunnel experiment it is possible to determine the optimum frequency and amplitude ratio for both configurations. Because a lot of frequencies and amplitudes can be applied in a short time, a more accurate estimation of their optimum value and the corresponding maximum lift coefficient increase can be obtained.
- The current simulations were performed in 2D, but it would be interesting to perform also a 3D wind tunnel test with an aircraft wing configuration. This can reveal the

influence of cross flow and cross flow instabilities, and the influence of the wing tip vortices. It is would be very difficult to investigate these effects numerically, since the computation time for a 3D simulation with a dynamic mesh will be very long. However, with respect to the final application on aircraft flaps, it is important to have some knowledge about these 3D effects.

Bibliography

- [1] Agard. A selection of experimental test cases for the validation of cfd codes. *Advisory Report 303*, 1, August 1994.
- [2] J.D. Anderson Jr. Fundamentals of Aerodynamics. McGraw-Hill, 2001.
- [3] Ansys Fluent 12.0 Theory Guide. Ansys Inc., January 2009. Available at www.fluentusers.com.
- [4] Ansys Fluent 12.0 User's Guide. Ansys Inc., January 2009. Available at www.fluentusers.com.
- [5] K. Artois. Active separation control by periodic excitation in an adverse pressure gradient. Master's thesis, Delft University of Technology, May 2005.
- [6] C. Bak, P. Fuglsang, J. Johansen, and I. Antoniou. Wind Tunnel Tests of the NACA63-415 and a modified NACA63-415 Airfoil. Risø National Laboratory, Roskilde, Denmark, December 2000.
- [7] L.M.M. Boermans. Research on sailplane aerodynamics at delft university of technology, boundary layer suction. Delft University of Technology, February 2007.
- [8] P.A. Davidson. *Turbulence: an Introduction for Scientists and Engineers*. Oxford University Press, 2004.
- [9] M. Drela. A User's Guide to MSES 3.04. MIT Department of Aeronautics and Astronautics, December 2006.
- [10] D. Greenblatt and I.J. Wygnansky. The control of flow separation by periodic excitation. *Progress in Aerospace Sciences*, 36:487–545, 2000.
- [11] M. van der Jagt. Separation postponement by means of periodic surface excitation. Master's thesis, Delft University of Technology, November 2008.
- [12] S.H. Kim and C. Kim. Separation control on naca23012 using synthetic jet. AIAA Paper, (2006-2853), June 2006.

102 Bibliography

[13] S.M. Klausmeyer, M. Papadakis, and J.C. Lin. A flow physics study of vortex generators on a multi-element airfoil. *AIAA Paper*, (96-0548), January 1996.

- [14] P. Marzocca. The naca airfoil series. Clarkson University, March 2009.
- [15] LT.P. Melton, C.S. Yao, and A. Seifert. Active control of the separation from the flap of a supercritical airfoil. *AIAA Journal*, 44(1), January 2006.
- [16] E.A. Munts. Synthetic jets for boundary layer separation control. Master's thesis, Delft University of Technology, March 2001.
- [17] Virtual Skies. NASA, 2009. Available at http://virtualskies.arc.nasa.gov.
- [18] B. Nishri and I. Wygnanski. Effects of periodic excitation on turbulent flow separation from a flap. *AIAA Journal*, 36(4), April 1998.
- [19] R. Petz and W. Nitsche. Designing actuators for active separation control experiments on high-lift configurations. Berlin University of Technology, 2007.
- [20] M. Schatz et al. Separation control by self-activated movable flaps. AIAA Paper, (2004-1243), January 2004.
- [21] S.K. Sinha and J. Zou. On controlling flows with micro-vibratory wall motion. *AIAA Paper*, (2000-4413), August 2000.
- [22] E. Stanewsky. Adaptive wing and flow control technology. *Progress in Aerospace Sciences*, 37:583–667, 2001.
- [23] M.V. van der Steen. Passive off-surface flow separation control methods on a simplified flapped configuration. Master's thesis, Delft University of Technology, April 2009.
- [24] E.L.N. Terry. Extension of the aerodynamic design program mses for the simulation of boundary layer suction. Master's thesis, Delft University of Technology, November 2004.
- [25] M. Van Dyke. An Album of Fluid Motion. Parabolic Press, 1982.

Appendix A

Dynamic mesh model

In this appendix some additional information with respect to the dynamic mesh model of Fluent is presented. First an example of a user-defined function is given in section A.1. Then an overview of the parameters used for the dynamic mesh simulations is presented in section A.2. Finally section A.3 gives an indication of the computational effort of the different simulations.

A.1 Example of a user-defined function

A.2 Dynamic mesh parameters

In fluent there are two dialog boxes in which parameters with respect to the dynamic mesh model can be entered: the dynamic mesh parameter box and the dynamic mesh zones box. In the dynamic mesh parameter box the Dynamic Mesh Model is selected. Further smoothing and remeshing are enabled as methods to update the grid. The parameters and their

values used are summarized in table A.1. The smoothing parameters are independent of the grid size, but this does not hold for the dimensional remeshing parameters. Therefore the remeshing parameters presented in table A.1 can not be copied to an arbitrary other dynamic mesh. It is remarked that next to these parameters also the option must improve skewness was enabled for the remeshing.

Table A.1: Overview of	f the	parameters u	used in	the d	vnamic	mesh	model

Mesh Methods	Parameter	Value
Smoothing	Spring constant factor	0.5
	Boundary node relaxation	0.5
	Convergence tolerance	0.001
	Number of iterations	20
Remeshing	Minimum length scale (m)	0.0007
	Maximum length scale (m)	0.0015
	Maximum skewness	0.4
	Size remesh interval	1

In the dynamic mesh zones box each grid zone can be classified according to its motion type. Table A.2 presents an overview of the motion and the parameters that were defined for the different grid zones. It should be remarked that smoothing and remeshing are enabled for the fluid, just as prescribed in the dynamic mesh model.

Table A.2: Grid zones and their corresponding motion type for the NLR7301 airfoil-flap configuration.

Grid zone	Motion type	Parameter	Value
Fliperon	Rigid body	X_{cq} (m)	1.0652
(-shadow)	8	Y_{cq} (m)	-0.0567
		θ (°)	0
		Cell height (m)	0.001
Fluid	Deforming	Minimum length scale (m)	0.0007
		Maximum length scale (m)	0.0015
		Maximum skewness	0.4
Main element upper surface	Stationary	Cell height (m)	0.001
Main element lower surface	Stationary	Cell height (m)	0.001
Flap upper surface	Stationary	Cell height (m)	0.001
Flap lower surface	Stationary	Cell height (m)	0.001
Pressure inlet	Stationary	Cell height (m)	0.001
Pressure outlet	Stationary	Cell height (m)	0.001

A.3 Computational effort

Table A.3 presents an overview of the computation times for the different configurations. All computations were made on a single processor, because the dynamic mesh model did not work properly for parallel computations.

Table A.3: Computation times for the different configurations.

	•		
Configuration	Grid size (cells)	Time per fliperon oscillation	Total computation time
Ramp flow	45.000	$\pm 2 \text{ hours}$	< 1 day
NACA-0015	450.000	\pm 8 hours	$\pm 6 \text{ days}$
NLR7301	350.000	\pm 5 hours	\pm 28 days

Appendix B

MSES analysis

In this appendix some more information about the MSES analysis will be presented. For this analysis the newest version of MSES, version 3.07, was used. First the input files will be discussed in some more detail and after that the results of the analysis will be presented. More information about MSES can be found in [9].

B.1 Input files

In total 2 input files are required to use the flow solver program MSES. The first input file is required for the initialization routine MSET and is called blade.xxx. This file should contain the name of the configuration, the size of the farfield and the coordinates of the airfoil elements. A general blade.xxx for an airfoil-flap configuration looks as follows:

```
NAME
XINL
        XOUT
                 YBOT YTOP
X(1,1)
        Y(1,1)
X(2,1)
        Y(2,1)
X(3,1)
        Y(3,1)
        Y(m,1)
X(m,1)
999
        999
X(1,2)
         Y(1,2)
X(2,2)
        Y(2,2)
X(3,2)
         Y(3,2)
X(n,2)
        Y(n,2)
```

MSES analysis

Where:

XINL, XOUT, YBOT and YTOP are the x-location of the left grid inlet plane, the x-location of the right grid outlet plane, the y-location of the lowest grid streamline / bottom wall and the y-location of the topmost grid streamline / upper wall, respectively. All locations are given in the airfoil coordinate system. The values used here are: 1.75, 3.0, -2.5, 2.5.

X(1,1),Y(1,1) till X(m,1),Y(m,1) are the coordinates of the main element, starting from the trailing edge and then going around the element

X(1,2),Y(1,2) till X(n,2),Y(n,2) are the coordinates of the flap, again starting from the trailing edge and going around.

The second input file is called MSES.xxx. This file contains the runtime parameters used by the flow solver MSES. For an explanation of the names of the parameters and the meaning of their numbers, the reader is referred to [9]. The used input file is case of free transition was:

3	4	5	7	GVAR(1)	GVAR(2)	GVAR(3)	GVAR(4)
3	4	5	7	GCON(1)	GCON(2)	GCON(3)	GCON(4)
0.185	2.0	0.0		MACHIN	CLIFIN	ALFAIN	
4	2			ISMOM	IFFBC		
4.5E06	9.0			REYNIN	ACRIT		
1.0	1.0	1.0	1.0	XTRS1	XTRP1	XTRS2	XTRP2
0.99	1.2			MCRIT	MUCON		

In case of a fully turbulent simulation the parameters XTRS1, XTRP1, XTRS2 and XTRP2 are all set to a value of 0.0.

B.2 Results

As was already explained in section 6.2.2, the flap position and deflection angle are varied manually and MSES is only used as an analysis tool. With the flap nose located at (0.91; -0.04) and a flap deflection of 35° , a reasonable amount of flow is separated from the trailing edge of the flap. The pressure distribution that resulted from the free transition simulation is shown in figure B.1. Unfortunately, MSES was not capable of finding a converged solution for the same configuration in a completely turbulent simulation.

In order to get an indication of the differences between a simulation with free transition and a fully turbulent simulation, both kind of simulations were performed with the flap at

B.2 Results

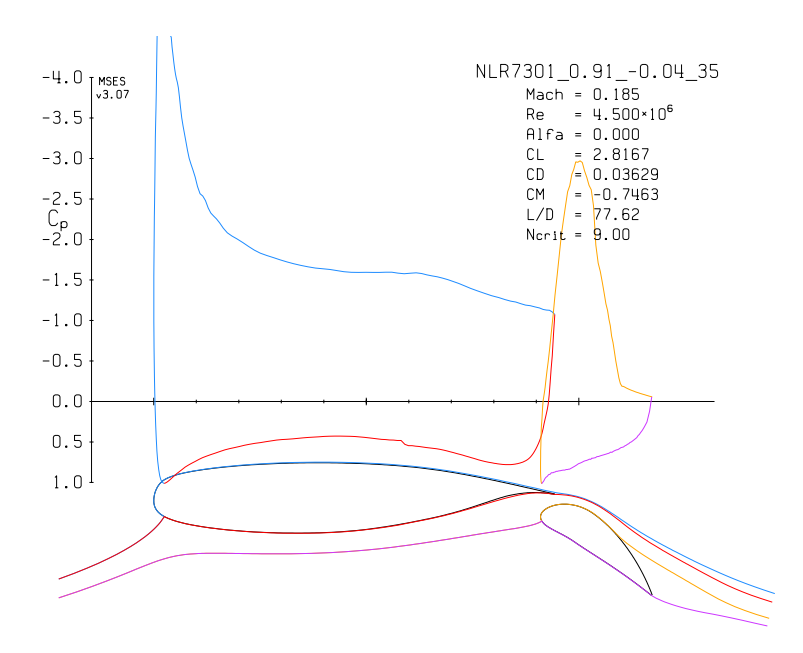


Figure B.1: Pressure distribution and streamlines for a flap deflection of 35°

the same position, but deflected over 30°. The results are shown in figure B.2. It should be kept in mind that Fluent always performs fully turbulent simulations. However, since the turbulence models of MSES and Fluent differ, it is well possible that also the predictions of the separation locations will be different.

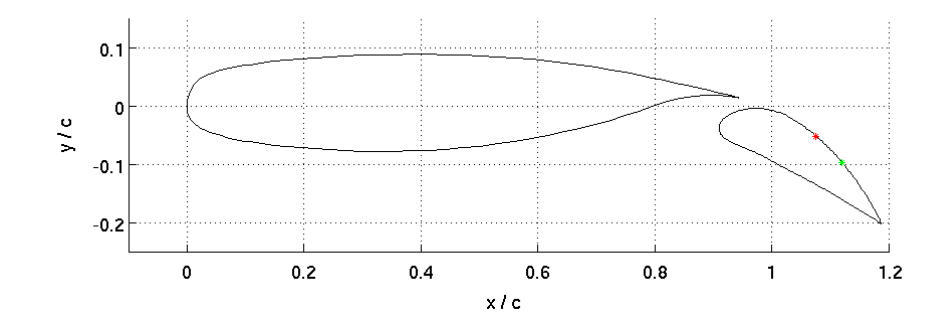


Figure B.2: Separation is predicted much earlier in the fully turbulent simulation (red asterisk) than in the simulation with free transition (green asterisk).

110 MSES analysis

Appendix C

NLR7301 airfoil-flap coordinates

Main element

0.943600000000000	1.499000000000000E-02	0.0
0.9426700000000000	1.519000000000000E-02	0.0
0.939880000000000	1.5800000000000002E-02	0.0
0.935240000000000	1.68999999999998E-02	0.0
0.928780000000000	1.830000000000000E-02	0.0
0.920510000000001	2.008000000000001E-02	0.0
0.910470000000000	2.24099999999999E-02	0.0
0.898700000000001	2.512000000000000E-02	0.0
0.885240000000000	2.819000000000000E-02	0.0
0.870150000000000	3.1620000000000002E-02	0.0
0.853490000000000	3.536000000000003E-02	0.0
0.835320000000000	3.941000000000001E-02	0.0
0.815720000000000	4.367999999999997E-02	0.0
0.794760000000000	4.814000000000002E-02	0.0
0.772530000000000	5.27299999999999E-02	0.0
0.749110000000001	5.73499999999998E-02	0.0
0.724590000000000	6.191000000000000E-02	0.0
0.699080000000000	6.628000000000006E-02	0.0
0.672670000000000	7.03799999999998E-02	0.0
0.645470000000000	7.4099999999999E-02	0.0
0.617580000000000	7.73699999999994E-02	0.0
0.589120000000000	8.01499999999999E-02	0.0
0.560190000000000	8.24799999999998E-02	0.0
0.530919999999999	8.437999999999997E-02	0.0
0.501410000000000	8.590000000000004E-02	0.0
0.471780000000000	8.704000000000006E-02	0.0
0.442160000000000	8.78099999999999E-02	0.0
0.4126500000000000	8.826000000000005E-02	0.0
0.383370000000000	8.83800000000000E-02	0.0
0.354440000000000	8.817999999999994E-02	0.0
0.325980000000000	8.767999999999994E-02	0.0
0.298090000000000	8.687000000000003E-02	0.0
0.270980000000000	8.57699999999999E-02	0.0
0.244480000000000	8.440000000000003E-02	0.0

0.218970000000000	8.276000000000000E-02	0.0
0.1944500000000000	8.08699999999997E-02	0.0
0.171030000000000	7.8740000000000004E-02	0.0
0.148800000000000	7.638000000000003E-02	0.0
0.127840000000000	7.381000000000001E-02	0.0
0.1178600000000000	7.245000000000001E-02	0.0
0.108240000000000	7.10299999999996E-02	0.0
9.897000000000002E-02	6.958000000000003E-02	0.0
9.00699999999997E-02	6.8070000000000006E-02	0.0
8.154999999999997E-02	6.6500000000000004E-02	0.0
7.341000000000003E-02	6.487999999999993E-02	0.0
6.567000000000006E-02	6.3170000000000004E-02	0.0
5.83199999999997E-02	6.137000000000001E-02	0.0
5.13899999999998E-02	5.942999999999997E-02	0.0
4.487000000000000E-02	5.73100000000000E-02	0.0
3.87699999999999E-02	5.50599999999998E-02	0.0
3.309000000000001E-02	5.26799999999998E-02	0.0
2.78599999999999E-02	5.009000000000003E-02	0.0
2.305000000000001E-02	4.716999999999997E-02	0.0
1.870000000000001E-02	4.372999999999998E-02	0.0
1.47899999999999E-02	3.978000000000003E-02	0.0
1.13300000000000E-02	3.54399999999999E-02	0.0
8.31999999999993E-03	3.07599999999999E-02	0.0
5.77000000000000E-03	2.581999999999999E-02	0.0
3.68000000000001E-03	2.06399999999999E-02	0.0
2.060000000000002E-03	1.5160000000000000E-02	0.0
8.8999999999995E-04	9.58999999999996E-03	0.0
1.90000000000001E-04	4.21999999999998E-03	0.0
-4.00000000000003E-05	-8.000000000000004E-04	0.0
1.90000000000001E-04	-5.51999999999997E-03	0.0
8.8999999999995E-04	-9.920000000000000E-03	0.0
2.060000000000002E-03	-1.417000000000000E-02	0.0
3.680000000000001E-03	-1.804000000000000E-02	0.0
5.77000000000000E-03	-2.172999999999999E-02	0.0
8.31999999999993E-03	-2.521000000000000E-02	0.0
1.133000000000000E-02	-2.851000000000001E-02	0.0
1.47899999999999E-02	-3.157999999999997E-02	0.0
1.870000000000001E-02	-3.4450000000000001E-02	0.0
2.305000000000001E-02	-3.7170000000000002E-02	0.0
2.78599999999999E-02	-3.971999999999998E-02	0.0
3.30999999999997E-02	-4.2150000000000000E-02	0.0
3.87699999999999E-02	-4.442999999999997E-02	0.0
4.487000000000000E-02	-4.660999999999999E-02	0.0
5.13899999999998E-02	-4.8730000000000002E-02	0.0
5.831999999999997E-02	-5.072999999999997E-02	0.0
6.567000000000006E-02	-5.263000000000003E-02	0.0
7.341000000000003E-02	-5.446000000000001E-02	0.0
8.154999999999997E-02	-5.621999999999999E-02	0.0
9.00699999999997E-02	-5.791000000000003E-02	0.0
9.897000000000002E-02	-5.954000000000003E-02	0.0
0.1082400000000000	-6.10899999999998E-02	0.0

0.1178600000000000	-6.259000000000007E-02	0.0
0.1278400000000000	-6.401999999999994E-02	0.0
0.1488000000000000	-6.6720000000000002E-02	0.0
0.1710300000000000	-6.916999999999995E-02	0.0
0.1944500000000000	-7.131999999999995E-02	0.0
0.2189700000000000	-7.316999999999999E-02	0.0
0.2444800000000000	-7.470000000000003E-02	0.0
0.2708900000000000	-7.585000000000001E-02	0.0
0.298090000000000	-7.6660000000000006E-02	0.0
0.3259800000000000	-7.703999999999997E-02	0.0
0.3544400000000000	-7.700999999999995E-02	0.0
0.3833700000000000	-7.652000000000005E-02	0.0
0.4126500000000000	-7.54999999999998E-02	0.0
0.4421600000000000	-7.38499999999999E-02	0.0
0.4717800000000000	-7.144000000000003E-02	0.0
0.5014100000000000	-6.819000000000001E-02	0.0
0.530919999999999	-6.417000000000005E-02	0.0
0.560190000000000	-5.958999999999997E-02	0.0
0.5891200000000000	-5.459000000000000E-02	0.0
0.6175800000000000	-4.920999999999997E-02	0.0
0.6454700000000000	-4.354999999999998E-02	0.0
0.6726700000000000	-3.74999999999999E-02	0.0
0.6990800000000000	-3.080000000000001E-02	0.0
0.7245900000000000	-2.361999999999999E-02	0.0
0.749110000000001	-1.5970000000000002E-02	0.0
0.7725300000000000	-8.240000000000008E-03	0.0
0.7947600000000000	-8.000000000000004E-04	0.0
0.8157200000000000	5.8500000000000002E-03	0.0
0.8353200000000000	1.115000000000000E-02	0.0
0.853490000000000	1.472000000000000E-02	0.0
0.8701500000000000	1.702000000000000E-02	0.0
0.8852400000000000	1.8180000000000002E-02	0.0
0.8987000000000001	1.842999999999998E-02	0.0
0.910470000000000	1.80699999999999E-02	0.0
0.9205100000000001	1.7330000000000002E-02	0.0
0.9287800000000000	1.644999999999999E-02	0.0
0.9352400000000000	1.52999999999999E-02	0.0
0.939880000000000	1.460000000000000E-02	0.0
0.9426700000000000	1.423000000000000E-02	0.0
0.9436000000000000	1.410000000000000E-02	0.0

Original flap delfected over 20°

1.201770696059817	-0.1037033815656575	0.0
1.200692709602058	-0.1029811314726236	0.0
1.197433081462563	-0.1009433816370903	0.0
1.192098632541988	-9.7501310354596304E-02	0.0
1.184785059458593	-9.2625897679360414E-02	0.0
1.175469146436702	-8.6819499090858732E-02	0.0
1.164243100871274	-8.0296585557556949E-02	0.0
1.151266635996908	-7.3232347497839925E-02	0.0

```
1.136691760967246
                         -6.5852380162565061E-02
                                                  0.0
 1.120755955460824
                         -5.8264402641412735E-02
                                                   0.0
 1.103671030389966
                          -5.0705134467632029E-02
                                                   0.0
 1.094772279314860
                         -4.6998015734260046E-02
                                                   0.0
 1.085675294600364
                         -4.3367730744865968E-02
                                                   0.0
 1.076407403347008
                         -3.9856151083806426E-02
                                                   0.0
 1.067008749782965
                         -3.6499171610663406E-02
                                                   0.0
 1.057510944888292
                         -3.3297656003528832E-02
                                                   0.0
 1.047938759240180
                         -3.0271261792910318E-02
                                                   0.0
 1.038351994597308
                         -2.7431113261199541E-02
                                                   0.0
 1.028772865013525
                         -2.4774653885055179E-02
1.019248355119872
                         -2.2318984671643494E-02
1.009816052621179
                         -2.0077786426697518E-02
 1.000499864416544
                         -1.8102327660781719E-02
                                                   0.0
0.9913220045598179
                         -1.6390051850554754E-02
0.9823320142053799
                         -1.4980274057031869E-02
                                                   0.0
                         -1.3838826776814892E-02
0.9735529710851710
                                                   0.0
0.9650446769578719
                         -1.2976834292295509E-02
                                                   0.0
0.9568267893539902
                         -1.2369526026283391E-02
                                                   0.0
0.9489428727031318
                         -1.2043399912152685E-02
                                                   0.0
0.9414219814620123
                         -1.1977105574146324E-02
                                                   0.0
0.9343025670135550
                         -1.2152712837940503E-02
                                                   0.0
0.9276342050230749
                         -1.2492489770531003E-02
                                                   0.0
0.9214621872763619
                         -1.2959712345178297E-02
                                                   0.0
                         -1.3555244239974298E-02
0.9158181247534728
                                                   0.0
0.9107079941791824
                          -1.4291902582560122E-02
                                                   0.0
0.9061206712710986
                         -1.5229489131616180E-02
0.9020937437340533
                         -1.6381684692875497E-02
                                                   0.0
0.8986246550447048
                         -1.7726275212489102E-02
                                                   0.0
0.8957253586526026
                         -1.9288894945739220E-02
                                                   0.0
0.8933984110810878
                         -2.1091757946474835E-02
                                                   0.0
0.8916874112707008
                         -2.3044315154050601E-02
                                                   0.0
0.8906034835038336
                         -2.5086764809786121E-02
                                                   0.0
0.8902680276758993
                         -2.6944039530312124E-02
0.8906041065101170
                         -2.8769046658295702E-02
                                                   0.0
0.8916553189470271
                         -3.0471237133091536E-02
                                                   0 0
0.8935661771249181
                         -3.1624329073912688E-02
                                                   0.0
0.8962930821032500
                         -3.2318871541404504E-02
                                                   0.0
0.8997248945909087
                         -3.2801741140312667E-02
                                                   0.0
                                                   0.0
0.9037855064782708
                         -3.3311281227266912E-02
0.9084168088519053
                         -3.3890192553781354E-02
                                                   0.0
0.9135991441813047
                         -3.4563245697046330E-02
0.9193231155402611
                         -3.5327020455628577E-02
                                                   0.0
                         -3.6152462372812603E-02
0.9255673725530175
                                                   0.0
0.9323003042395167
                         -3.7038707770506496E-02
                                                   0.0
0.9394996965459100
                         -3.7988313172051619E-02
                         -3.9009811825563893E-02
0.9471305182907075
                                                   0.0
                         -4.0096363328176829E-02
0.9551739756214931
                                                   0.0
0.9635796637057945
                         -4.1240263598931987E-02
                                                   0.0
0.9723245048116708
                         -4.2475680141227552E-02
0.9813555375833078
                         -4.3772694820256128E-02 0.0
```

(0.9906531044901984	-4.5156078213208023E-02	0.0
	1.000157403773662	-4.6614706037691571E-02	0.0
	1.009835960775549	-4.8179325595671695E-02	0.0
	1.019654607992463	-4.9826859155207494E-02	0.0
	1.029562076913838	-5.1581213615397387E-02	0.0
	1.039507962707202	-5.3434684895282962E-02	0.0
	1.049470051318706	-5.5389829518205536E-02	0.0
	1.059385120788236	-5.7444920127981310E-02	0.0
	1.069218139934303	-5.9608489972726227E-02	0.0
	1.078940917978282	-6.1870278448140512E-02	0.0
	1.088503050087701	-6.4222581473265747E-02	0.0
	1.097863528356296	-6.6661115168576757E-02	0.0
	1.115844546202668	-7.1758388675898371E-02	0.0
	1.132621721261670	-7.7034722349917373E-02	0.0
	1.147945620405216	-8.2356762845671089E-02	0.0
	1.161626646774832	-8.7485234106569151E-02	0.0
	1.173499110411146	-9.2232128586585554E-02	0.0
	1.183351995058059	-9.6563209760453378E-02	0.0
	1.191137555939242	-0.1001418466190047	0.0
	1.196783243190244	-0.1027287976165836	0.0
	1.200234402610001	-0.1042403195844767	0.0
	1.201377372894992	-0.1047840280795613	0.0

Adapted flap delfected over 35°

1.1726	-0.222856	0.00
1.1716	-0.219772	0.00
1.1703	-0.216505	0.00
1.1690	-0.213251	0.00
1.1677	-0.210010	0.00
1.1663	-0.206782	0.00
1.1650	-0.203567	0.00
1.1636	-0.200365	0.00
1.1622	-0.197176	0.00
1.1608	-0.194000	0.00
1.1593	-0.190837	0.00
1.1578	-0.187687	0.00
1.1564	-0.184550	0.00
1.1548	-0.181427	0.00
1.1533	-0.178316	0.00
1.1518	-0.175219	0.00
1.1502	-0.172134	0.00
1.1486	-0.169063	0.00
1.1470	-0.166006	0.00
1.1453	-0.162962	0.00
1.1437	-0.159931	0.00
1.1420	-0.156915	0.00
1.1403	-0.153911	0.00
1.1386	-0.150922	0.00
1.1368	-0.147947	0.00
1.1351	-0.144986	0.00

1.1333	-0.142039	0.00
1 1215	-0.139106	0.00
1.1297	-0.136188	0.00
1.1278	-0.133285	0.00
1.1260		0.00
1.1241	-0.127523	0.00
1.1222	-0.124665	0.00
1.1202		0.00
1.1183	-0.118996	0.00
1.1163	-0.116185	0.00
1.1144		0.00
1.1123	-0.110613	0.00
1.1103	-0.107851	0.00
1.1083		0.00
1.1062	-0.102380	0.00
1.1041	-0.099670	0.00
1.1020		
		0.00
1.0999		0.00
1.0977	-0.091652	0.00
1.0955		0.00
1.0933		0.00
1.0911	-0.083805	0.00
1.0889	-0.081229	0.00
1.0866		0.00
1.0843		0.00
1.0820	-0.073629	0.00
1.0797	-0.071140	0.00
1.0773	-0.068673	0.00
1.0750	-0.066230	0.00
1.0726	-0.063810	0.00
1.0701	-0.061416	0.00
1.0677		
		0.00
1.0652		0.00
1.0627	-0.054385	0.00
1.0602		0.00
1.0577		0.00
1.0551	-0.047601	0.00
1.0525	-0.045398	0.00
1.0499	-0.043225	0.00
1.0473	-0.041084	0.00
1.0446	-0.038976	0.00
1.0419	-0.036901	0.00
1.0392	-0.034861	0.00
1.0365	-0.032856	0.00
1.0337	-0.030889	0.00
1.0305	-0.028741	0.00
1.0269	-0.026462	0.00
1.0232	-0.024306	0.00
1.0195	-0.022279	0.00
1.0156	-0.020384	0.00
1.0117	-0.018622	0.00

1.0078 1.0038 0.9997 0.9956 0.9914 0.9872 0.9830 0.9787 0.9744	-0.016999 -0.015517 -0.014179 -0.012987 -0.011946 -0.011057 -0.010325 -0.009753 -0.009343	0.00 0.00 0.00 0.00 0.00 0.00 0.00 0.0
0.9700	-0.009102	0.00
0.9657	-0.009033	0.00
0.9613	-0.009143	0.00
0.9569	-0.009439	0.00
0.9525	-0.009930	0.00
0.9481	-0.010627	0.00
0.9437	-0.011546	0.00
0.9393	-0.012707	0.00
0.9350	-0.014138	0.00
0.9306 0.9263 0.9220	-0.015880 -0.017997 -0.020596	0.00
0.9177 0.9156	-0.023889 -0.025937	0.00 0.00 0.00
0.9136	-0.028426	0.00
0.9116	-0.031747	0.00
0.9107	-0.034135	0.00
0.9102	-0.036276	0.00
0.9100	-0.040000	0.00
0.9106	-0.043672	0.00
0.9114	-0.045738	0.00
0.9125	-0.048009	0.00
0.9146	-0.051121	0.00
0.9166	-0.053436	0.00
0.9184	-0.055345	0.00
0.9221	-0.058464	0.00
0.9257	-0.061029	0.00
0.9291	-0.063251	0.00
0.9324	-0.065239	0.00
0.9355 0.9386	-0.067056 -0.068742	0.00
0.9415	-0.070326	0.00
0.9444	-0.071829	0.00
0.9471	-0.073264	0.00
0.9498	-0.074645	0.00
0.9524	-0.075979	0.00
0.9549	-0.077275	0.00
0.9573	-0.078537	0.00
	-0.079771 -0.080982 -0.082173 -0.083348	0.00 0.00 0.00 0.00

0.9684	-0.084510	0.00
0.0705	-0.085661	
0.9705		0.00
0.9725	-0.086805	0.00
0.9744	-0.087945	0.00
0.9764	-0.089084	0.00
0.9783	-0.090225	0.00
0.9801		0.00
0.9819	-0.092526	0.00
0.9837	-0.093692	0.00
0.9855		0.00
0.9876	-0.096327	0.00
0.9901	-0.098043	0.00
0.9926	-0.099748	0.00
0.9951	-0.101443	0.00
0.9975	-0.103129	0.00
1.0000		0.00
1.0026	-0.106478	0.00
1.0051	-0.108143	0.00
1.0076	-0.109804	0.00
1.0101	-0.111460	0.00
1.0126		0.00
1.0152		0.00
1.0177	-0.116413	0.00
1.0203	-0.118061	0.00
1.0228		0.00
1.0254	-0.121358	0.00
1.0280	-0.123007	0.00
	-0.124658	
1.0305		0.00
1.0331	-0.126312	0.00
1.0357	-0.127968	0.00
1.0383	-0.129628	0.00
1.0408	-0.131292	0.00
1.0434	-0.132960	0.00
1.0460	-0.134633	0.00
1.0486	-0.136312	0.00
1.0512		0.00
1.0539	-0.139686	0.00
1.0565	-0.141383	0.00
	-0.143087	
1.0591		0.00
1.0617	-0.144799	0.00
1.0643	-0.146518	0.00
1.0669	-0.148245	0.00
1.0696	-0.149980	0.00
1.0722	-0.151724	0.00
1.0748	-0.153477	0.00
1.0775	-0.155239	0.00
1.0801	-0.157011	0.00
1.0827	-0.158792	0.00
1.0854	-0.160584	0.00
1.0880	-0.162385	0.00
1.0907	-0.164197	0.00

1.0933	-0.166019	0.00
1.0960	-0.167853	0.00
1.0986	-0.169697	0.00
1.1013	-0.171552	0.00
1.1040	-0.173419	0.00
1.1066	-0.175297	0.00
1.1093	-0.177187	0.00
1.1120	-0.179088	0.00
1.1146	-0.181001	0.00
1.1173	-0.182926	0.00
1.1200	-0.184863	0.00
1.1227	-0.186813	0.00
1.1254	-0.188774	0.00
1.1280	-0.190748	0.00
1.1307	-0.192734	0.00
1.1334	-0.194733	0.00
1.1361	-0.196744	0.00
1.1388	-0.198767	0.00
1.1415	-0.200803	0.00
1.1442	-0.202852	0.00
1.1469	-0.204913	0.00
1.1496	-0.206988	0.00
1.1523	-0.209074	0.00
1.1551	-0.211174	0.00
1.1578	-0.213286	0.00
1.1605	-0.215411	0.00
1.1632	-0.217549	0.00
1.1660	-0.219699	0.00
1.1687	-0.221862	0.00
1.1716	-0.224233	0.00

